

**Ocean Heat Delivery Mechanisms Beneath Antarctic Ice
Shelves**

by

Alon Stern

A dissertation submitted in partial fulfillment
of the requirements for the degree of
Doctor of Philosophy
Department of Mathematics
Courant Institute of Mathematical Sciences
New York University
May 2014

David Holland

© Alon Stern

All Rights Reserved, 2014

Dedication

Whose woods these are I think I know.

His house is in the village though;

He will not see me stopping here

To watch his woods fill up with snow.

My little horse must think it queer

To stop without a farmhouse near

Between the woods and frozen lake

The darkest evening of the year.

He gives his harness bells a shake

To ask if there is some mistake.

The only other sounds the sweep

Of easy wind and downy flake.

The woods are lovely, dark and deep,

But I have promises to keep,

And miles to go before I sleep,

And miles to go before I sleep.

Robert Frost

Dedicated to my parents

Acknowledgements

First and foremost, I would like to thank my advisor David Holland. David's hands off style of teaching encouraged me to think independently and to create my own research agenda. His approach of simplifying a problem down to its bare essentials and removing all the jargon, helped me to discipline my thinking. I am grateful to David for including me on the research trips to Antarctica and Greenland. These field campaigns were the highlight of my graduate school experience and gave me new perspective on ocean-ice interactions.

I would like to thank Louis-Philippe Nadeau for all of the help, advice, instruction and direction. I appreciate him teaching me how to run his model, and for being patient with me when progress was slow. I think that working with LP made me to step up my game and work harder, more thoughtfully and more efficiently. I am convinced that I am a better researcher as a result of his mentorship.

Thank you to the other members of my PhD committee: Adrian Jenkins and Oliver Bühler. Your input and comments have helped significantly improve this thesis. Thank you to Mike Dinniman for running the model used in Chapter 4, and for all the useful feedback he gave me when while I was preparing Chapter 4. His thoroughness and attention to detail is hugely appreciated. Thank you to Paul Holland for his comments on Chapter 1, and to Joel Sommeria for teaching me Particle Image Velocimetry and Laser Induced Fluorescence.

Thank you to Ed Gerber, Shafer Smith and Olivier Pauluis who put so much effort into improving the education of all students in the Center for Atmosphere

Ocean Science. Thanks to Tamar Arnon for being a Courant mom to all PhD students. Estaban Tabak, thank you for filling the 5th floor with laughter and for making Courant a great place to come to work everyday.

I would like to thank Mitch Bushuk and Carl Gladish for the many conversations which were extremely useful in putting this dissertation together. Maria Gehne, Dharshi Devendran and Ray Yamada, thanks for all the office conversations, cups of tea, talks about the future. You guys were great office companions.

Thanks to my parents, Micky and Gilad; my siblings Orly, Guy and Eitan and all my friends back home, Romany Pinnock, Adam Sack, Terence Goldberg, Adi Lazar, Adam Baldinger, Joel Bregman (and others), for all the support over the past five years. Thanks to all my New York housemates, Sahar Sajadieh, Miroslav Urbanek, Eszter Kirs, Mak Kamenica, Quoc Doan, Mor Haimovitz, David Alvarez, Juliane Eichblatt, Ellie Lotan, Sammy Kanofsky, Benji Holzman (and others), for providing the backdrop to my New York life. Thank you to Mia Candy for wonderful weekends in Brooklyn. Thanks to Matan Harel and Lukas Koehler for lunch time conversations, written and oral exam preparations, and fun evenings out which provided useful distractions. Special thank you to Mia Candy and Gilad Stern for help with editing.

Finally, I would like to thank all the members of *Xichen and the Li's*. Your music has inspired a generation.

Abstract

Ocean currents around Antarctica are responsible for transporting heat under the Antarctic ice shelves and exporting cold melt-water out into the open ocean. These ocean currents strongly influence the melt rates beneath the Antarctic ice shelves. This thesis explores the three modes of melting beneath Antarctic ice shelves using laboratory experiments, analysis of field observations, and both complex and simple numerical models.

In Chapter 2, we construct a laboratory experiment to simulate the density driven circulation under an idealized Antarctic ice shelf (mode 1). Results confirm that the ice front can act as a dynamic barrier that partially inhibits fluid from entering or exiting the ice shelf cavity, away from two wall-trapped boundary currents. The strength of the dynamic barrier is sensitive to changes in the ice shelf geometry and changes in the buoyancy fluxes which drive the flow.

Chapter 3 explores how instabilities in topographically steered jets could be responsible for the exchange of warm Circumpolar Deep Water across the continental shelf break in West Antarctica (mode 2). Results show that the majority of mixing occurs in discrete mixing events which coincide with the shelf break jet becoming baroclinically unstable. The largest instability events display an intermittent low frequency variability with instabilities occurring up to 50 years apart.

Chapter 4 uses observational data to study the summer intrusion of surface waters below McMurdo Ice Shelf (mode 3). A six-month temperature record collected below the ice shelf in 2011-2012 shows the temporal and spatial structure of the summertime warm water signal that penetrates beneath the ice shelf. A Ross Sea numerical model demonstrates a seasonal warm water pathway leading from the west side of the Ross Sea Polynya (RSP) towards McMurdo Sound.

Contents

Dedication	iii
Acknowledgements	iv
Abstract	vi
List of Figures	ix
List of Tables	xxi
1 Introduction	1
2 The effect of geometry on ice-shelf ocean cavity ventilation: a laboratory experiment	7
2.1 Introduction	7
2.2 Experimental setup and data collection	12
2.3 Major features of the flow	31
2.4 Discussion	47
2.5 Conclusion	52
3 Instability and mixing of ocean jets along an idealized Antarctic continental shelf break	55
3.1 Introduction	55
3.2 Numerical model and experimental design	58

3.3	Effect of topography and wind on cross shelf exchange	62
3.4	Intermittent critical regime	76
3.5	Intermittent critical regime	76
3.6	Jet drifting	86
3.7	Confirmation of drifting jets using primitive equation model	94
3.8	Conclusions	97
4	Intrusion of warm surface water beneath the McMurdo Ice Shelf, Antarctica	100
4.1	Introduction	100
4.2	Background oceanography	103
4.3	Observations at Windless Bight	106
4.4	Modeling of ocean circulation and temperatures	118
4.5	Discussion	132
4.6	Conclusion	135
5	Conclusion	138
5.1	Summary	138
5.2	Future work:	139
	Bibliography	142

List of Figures

1.1	Schematic showing the three modes of warm water intrusion	3
2.1	Schematic diagram of processes beneath an idealized ice shelf.	9
2.2	The experimental setup for our experiment. The upper panel shows the side view of the experiment. The lower panel shows the plan view of the experiment. The red and blue marks indicate the position of the fresh and dense water sources, respectively. The y -axis indicates latitude, the x -axis indicates the zonal direction. The positive y direction points north and the positive x -axis points east.	14
2.3	Summary of seven different experiments runs performed. The seven experimental runs are divided into three experiments. All three experiments used the same Control Run, which is positioned in the center. The top row shows Thickness Investigation where the ice shelf cavity thickness was varied. Row two shows Gradient Investigation where the slope of the ice shelf was varied. Row three shows Buoyancy Investigation, where the control geometry was used, but the fluxes of the dense and fresh water sources were varied.	18

2.8	The time-mean interior concentration field for The Stretch is shown at different latitudes. The interior concentration is defined as the average concentration between $x = 40$ and $x = 172$. In this figure we can see strong density gradient across the ice front.	37
2.9	The time-mean vertically integrated meridional volume flux for all the experimental runs. The arrows indicate direction and magnitude of the integrated volume horizontal flux. The figure shows how changing the geometry of the ice shelf and the dense and fresh sources has an effect significant on the circulation inside the ice shelf cavity. The three experimental runs in the column on the left of the figure all systematically show a more intense circulation on the continental shelf, and less intense cavity circulation, compared to the Control Run.	39
2.10	The time-mean, meridional velocity (cm s^{-1}) of the dense plume at $y=-54\text{cm}$ is plotted for each experiment. Only the negative velocity has been plotted to allow the plume to be seen more clearly. Density contour lines have been plotted over the top.	41
2.11	The time-mean concentration contours of the dense plume at $y=-54\text{cm}$ is plotted for each experiment.	42
2.12	Time series of the volume flux of the dense plume at $y = -54\text{cm}$ (blue) and at $y=-110$ (green), which are both latitudes inside of the ice shelf cavity. The horizontal axis shows time in seconds. A horizontal red line is plotted indicating the dense source flux rate in the experiment. The dashed vertical lines indicate the times between the time-averages were taken in the previous sections. . . .	47

2.13 A schematic summarizing the results from the three investigations. The size of the dense plume, the strength of the circulation inside the ice shelf cavity, and the strength of the circulation outside the ice shelf cavity are shown by the size of the arrows in each of the experimental runs (not to scale)	50
3.1 Hovmöller diagram of the upper-layer zonally-averaged zonal veloc- ity are shown for different wind forcings and different shelf widths. Wind forcings $\tau = 0.04 \frac{N}{m^2}$ and $\tau = 0.12 \frac{N}{m^2}$ are shown in the left and right columns, respectively. Shelf widths W=10km, 30km, 50km, 200km, and 500km are shown from top to bottom.	64

3.11 Panel (a) shows the meridional jet drifting velocity for different values of $Q = \frac{\partial^2 h_b}{\partial y^2}$. The black curve uses $W=100\text{km}$ and imposed shear, $U_s = 0.3$. The red curve uses $W=50\text{km}$ and $U_s = 0.3$. The jets drift northwards for positive Q and southward for negative Q . Panel (b) shows the jet drifting velocity for different values of imposed shear, U_s . The black curve uses $W=100\text{km}$ and $Q = 10 \times 10^{-9}$. The red curve uses $W=50\text{km}$ and $Q = 25 \times 10^{-9}$. Both sets of simulations used a parabolic bottom topography.	93
3.12 Simulations run using MITgcm primitive equation model. Figure shows the zonally-averaged zonal velocity on the surface for simulations using (a) $W=20\text{km}$, (b) $W=100\text{km}$, (c) $W=300\text{km}$. Jets which form over the continental shelf break region are seen to drift northwards.	95
3.13 Hovmöller diagram of the zonally-averaged surface tracer concentration for a run using $\tau_0 = 0.1$ and $W=100\text{km}$. Black lines show the surface velocity contours of the jet. Cross shelf tracer fluxes coincide with the jet drifting northwards.	96
4.1 Schematic showing the three modes of warm water intrusion	102
4.2 Panel (a) shows a map of the region around McMurdo Sound. Panel (b) shows the bathymetry around McMurdo Sound as used in the circulation model. Panel (c) shows the depth of the base of the ice shelf (below MSL). Panel (d) shows the thickness of the water column.	105

4.3	Borehole setup: Two boreholes were drilled through the ice 20 meters apart. Three cables were deployed through the boreholes. Pressure transducers and PT100's are connected to the cables as shown above.	109
4.4	(a) Observations of the ocean temperature profile at Windless Bight from November 2011 to June 2012 made using a DTS fiber optic cable. (b) Model ocean temperature profile at Windless Bight from November 2010 to June 2011.	112
4.5	Panel (a) shows the time evolution maximum model temperature in the water column at the selected points to the north (green) and west (magenta) of Ross Island, and also at Windless Bight (blue) to the south of Ross Island. In Panel (b), the blue curve shows the time evolution of the model melt rate found at the grid point closest to Windless Bight.	113
4.6	Mean model velocities around Ross Island. Panel (a) shows the annual mean velocity at 25m below the ocean surface (open ocean or below the ice shelf base). Panel (b) shows the mean surface velocity for January 2011.	121
4.7	Ocean temperatures on the level 20 terrain following model surface from December 2010 to March 2011. The sequence shows the warm water signal originating to the west of the Ross Sea Polynya, being advected into McMurdo Sound and wrapping around Ross Island under the McMurdo Ice Shelf towards Windless Bight.	122

4.8 Ocean temperatures on the level 20 surface from December 2003 to March 2004. The sequence shows the warm water signal originating to the west of the Ross Sea Polynya, being advected into McMurdo Sound and wrapping around Ross Island under the McMurdo Ice Shelf towards Windless Bight.	123
4.9 Melt rates at the base of the ice shelf in mid-February, at the peak of melting.	124
4.10 The trajectories of four groups of 3D Lagrangian model floats is shown. Each group of floats consists of ten floats which were allowed to drift for 120 days . The initial position of the floats is indicated by the black triangles. Panels (a), (b) and (c) show floats released at model level 20 on 1 Dec 2011, 16 Dec 2011 and 31 Dec 2011, respectively. Panel (d) shows floats released at the surface on 16 Dec 2011.	126
4.11 Cross sections of model results running across the ice shelf front in the south of McMurdo Sound in 2011. Panel (a) shows the salinity in late January 2011. Panel (b) shows the potential temperature in late January 2011. Panel (c) shows the potential density in late January 2011. Panel (d) shows the potential temperature in late February 2011. Panel (e) shows the salinity in late September 2011. Panel (f) shows the potential temperature in late September 2011. . .	128
4.12 Integrated sea-ice cover over the Ross Sea (panels (a) and (b)) and over the Ross Sea continental shelf (panels (c) and (d)). Model results are shown in red and SSMIS satellite observations are shown in blue.	132

List of Tables

2.1	Parameters used in the experimental runs	17
2.2	Non-dimensional parameters used in the experimental runs. The experimental runs have been grouped into three groups corresponding to the Thickness Investigation, the Gradient Investigation and the Buoyancy Investigation. The same control run was used for all three investigations.	25
3.1	Model parameters	60
4.1	Melt rate sensitivities are shown for six different parameters. The first column shows the parameters used in the melt rate calculation. The second column shows the value of the parameters used. The third column shows the amount that the parameter is changed by in the sensitivity study. The fourth column shows the change in the annual mean melt rate as a result of changing the parameter.	118

Chapter 1

Introduction

The question of the how the ocean transports heat towards the ice shelves of Antarctica is one of the central questions in polar oceanography. The efficiency of this heat delivery mechanism is a major factor in setting ice shelf melt rates and Antarctic mass balance. The sudden disintegration of the Larsen B ice shelf (Scambos et al, 2004), and the recent acceleration in the velocity of the ice shelves and ice streams in the Amundsen and Bellingshausen Seas (Pritchard et al, 2012; Horgan et al, 2011), are strong reminders to the climate community that changes in Antarctica can occur rapidly, and without warning. Understanding the physical processes involved in melting and breaking ice shelves is essential if we hope to project future sea levels in a changing climate.

Ice shelf melting processes, and the intrusion of warm water beneath ice shelves, can be described by three modes (Jacobs et al, 1992; Hattermann et al, 2012) as shown in the schematic in Fig. 1.1 (Craven, pers. comm., 2012). Mode 1 is the

intrusion of High Salinity Shelf Water (HSSW) into the ice shelf cavities along the sea-floor bottom. HSSW is formed due to brine rejection from sea-ice formation. Since the HSSW is formed at the surface and the freezing point of salt water decreases with increased pressure, the HSSW is warmer than the freezing point at the deep grounding line, and its intrusion causes melting at the grounding line (MacAyeal, 1984). Mode 1 circulation causes melting in the grounding line areas of the Ross, Filchner-Ronne and Amery Ice Shelves (Jacobs et al, 1992). Mode 2 is the intrusion of Circumpolar Deep Water (CDW) into the ice shelf cavity at intermediate depths. The CDW can be more than 4°C warmer than the in-situ freezing point and thus causes rapid melting. Mode 2 melting is largely responsible for the recent accelerated melt rates found on ice shelves in the Amundsen and Bellingshausen Seas (Jacobs et al, 2011). Lastly, a mode 3 intrusion is caused by warm surface waters that enter the ice shelf cavity near the surface, forced by tides and/or seasonal currents, causing melting near the ice front (Jacobs et al, 1992).

The three modes of circulation are not mutually exclusive and can overlap and interact with one another. Interaction between the modes can be important for determining the heat and mass exchange beneath ice shelves (Hattermann et al, 2012). Nevertheless, the modes provide a good framework for understanding ice shelf melting processes.

The structure of this PhD dissertation is based on the above-mentioned framework. The dissertation consists of three chapters, each of which deals with one of the three modes of melting.

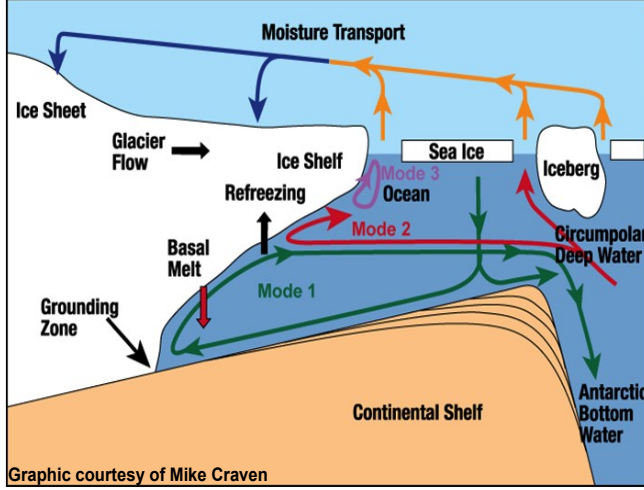


Figure 1.1: Schematic showing the three modes of warm water intrusion.

Chapter 2 focuses on mode 1 of melting. In this chapter, we construct a laboratory experiment to simulate the density driven circulation under an idealized Antarctic ice shelf and to investigate the flux of dense and fresh water in and out of the ice shelf cavity. In the experiment, we vary the ice shelf geometry in order to observe how the circulation beneath the ice shelf responds to changes in ice shelf geometry. We also make changes to the buoyancy fluxes which drive the flow and observe how the system responds to these changes.

It has been observed in numerical models that the ice shelf front can act as a dynamical barrier which separates water masses inside and outside of the ice shelf cavity (Determan and Gerdes, 1994; Grosfeld et al, 1997). This is because flow outside the ice shelf cavity is dominated by the barotropic mode, which steers the flow along the ice front rather than into the ice shelf cavity. The presence of the ice shelf imposes a change in water column thickness which presents a barrier for the barotropic flow. The barotropic flow tends to move along $\frac{f}{H}$ contours which run parallel to the shelf.

In our experiments, we are particularly concerned with how the strength of this dynamical barrier responds to changes in ice shelf geometry and buoyancy forcing. The strength of the dynamical barrier controls the heat flux into the ice shelf cavity from the open ocean, which in turn sets the basal melt rates beneath the ice shelf.

Our results confirm that the ice front can act as a dynamic barrier that partially inhibits fluid from entering or exiting the ice shelf cavity, away from two wall-trapped boundary currents. This barrier results in a density jump across the ice front and in the creation of a zonal current, which runs parallel to the ice front. However despite the barrier imposed by the ice front, there is still a significant amount of exchange of water in and out of the cavity. This exchange takes place through two dense and fresh gravity plumes, which are constrained to flow along the sides of the domain by the Coriolis force. The flux through the gravity plumes and the strength of the dynamic barrier are shown to be sensitive to changes in the ice shelf geometry. They are also sensitive to changes in the buoyancy fluxes that drive the flow.

Chapter 3 is concerned with the mode 2 intrusions of Circumpolar Deep Water (CDW) that cross the continental shelf break in the Amundsen and Bellingshausen Seas. In this chapter we explore how instabilities in topographically steered jets could be responsible for the exchange of warm Circumpolar Deep Water across the continental shelf break. The relationship between the flux of water across the continental shelf break and the topography of the continental slope is studied in an idealized setting using a 2-layer quasi-geostrophic model.

Results show that the majority of mixing occurs in discrete mixing events that coincide with the jet becoming baroclinically or barotropically unstable. The largest mixing events occur for continental shelf slopes that are steep enough to allow for a large build up of shear. Shelves that are narrower than the eddy scale cannot maintain a strong jet, and therefore have reduced mixing. For intermediate width shelves, jets are able to remain stable for many years, building up a large amount of shear, before becoming unstable. The largest instability/mixing events are associate with jets that build up the most shear. These jets display an intermittent low frequency variability, with instabilities occurring up to 50 years apart.

Chapter 4 focuses on mode 3 intrusions. We focus on a particular example in which we use observational data to study the summer intrusion of surface waters below McMurdo Ice Shelf. In this chapter a six-month temperature record collected below McMurdo Ice Shelf in 2011-2012 shows the temporal and spatial structure of the summertime warm water signal that penetrates beneath the ice shelf. The strength and duration of the warm water intrusion suggest an annual melt rate at

Windless Bight of 0.71m/yr. A Ross Sea numerical model demonstrates a seasonal warm water pathway leading from the west side of the Ross Sea Polynya (RSP) towards the McMurdo Sound. The warm water enters McMurdo Sound, subducts beneath the ice shelf, and causes accelerated summer melting.

The temperatures in this study were recorded using Distributed Temperature Sensing fiber optics, which give a vertical temperature profile at a one meter vertical resolution. This study constitutes one of the first successful implementations of this technology in polar regions.

Chapter 2 is based on a manuscript co-authored by D.M. Holland, J. Sommeria, A. Jenkins and P. Holland. The results are published in the journal *Experiments in Fluids* (Stern et al, 2014). Chapter 3 is co-authored by L.P. Nadeau and D.M Holland. The results are currently being prepared for submission to the *Journal of Physical Oceanography* which is due to be submitted before May 2014. Results in Chapter 3 using MITgcm, are unpublished. Chapter 4 is based on a manuscript co-authored by M. S. Dinniman, V. Zagorodnov, S. W. Tyler, and D. M. Holland, and has been published in *Journal of Geophysical Research* (Stern et al, 2013). Technical results about DTS described in Chapter 4 have been published in Tyler et al (2013). Drilling techniques described in Chapter 4 have been submitted for publication in *Annals of Glaciology* (Zagorodnov et al, 2014). I am a co-author on Tyler et al (2013) and Zagorodnov et al (2014).

Chapter 2

The effect of geometry on ice-shelf ocean cavity ventilation: a laboratory experiment

2.1 Introduction

The Greenland and Antarctic ice sheets are comprised of many separate ice streams - fast-flowing rivers of ice that flow downhill under gravity. Where these ice streams come into contact with the oceans, they either fracture and calve icebergs, or they form ice shelves - large floating glaciers that can be several kilometers thick and several hundreds of kilometers wide.

The dynamics of the water within ice shelf cavities and the flux of dense water in and out of the ice shelf cavities, has a strong influence on the calving and melting rates of the ice shelves. However, the large quantity of ice above the cavities

has made observational measurements extremely difficult and as a result, there exists relatively little data about the circulation within the cavities. In addition to this, the sloping and melting upper boundary above the cavity has a strong effect on the dynamics of the flow within the cavity and makes the dynamics distinct from all other ocean flows.

Nevertheless, in the past 30 years a small body of observational measurements under the Antarctic ice shelves has begun to be created (Nicholls, 1996; Makinson et al, 2005, 2006; Nicholls et al, 2009; Hattermann et al, 2012; Jenkins et al, 2012) and a general picture of dominant dynamical processes that take place within the ice shelf cavities has begun to emerge. The first one-dimensional models to describe ocean-ice interactions within the Antarctic ice shelf cavities were put forward by MacAyeal (MacAyeal, 1984, 1985) and Jenkins (Jenkins, 1991) and later extended to a 2-D model by Holland and Feltham (Holland and Feltham, 2006). This model can be summarized as follows (Figure 2.1): The cold Antarctic winter conditions cause the surface water at the ice front to freeze. The salt rejected during freezing mixes with the cold ambient surface water to form High Salinity Shelf Water (HSSW). The dense HSSW sinks to the bottom of the water column and flows down into the ice shelf cavity towards the grounding line.

Since the freezing point of sea water decreases with depth, the temperature of the HSSW, which was formed at the surface, is warmer than the freezing point of sea water at the grounding line. When the HSSW comes into contact with the ice at the grounding line it causes the ice to melt, releasing cold fresh melt water into the ice cavity. The melt water and HSSW mix to form a plume of buoyant Ice

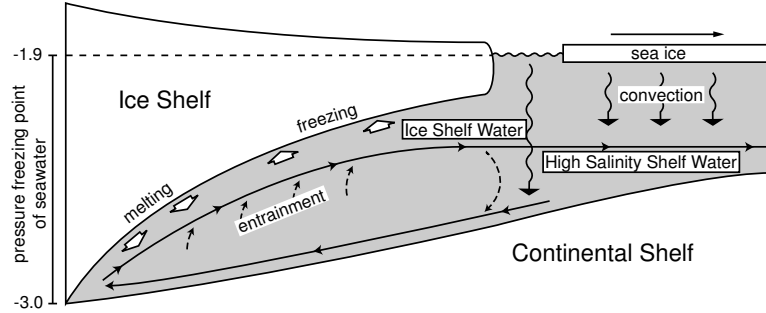


Figure 2.1: Schematic diagram of processes beneath an idealized ice shelf.

Shelf Water (ISW), which rises up along the shelf base.

As it rises, the ISW becomes super-cooled and begins to form frazil ice. Much of this frazil ice deposits itself on the underside of the ice shelf, where it is known as marine ice. The dynamics of the upward moving plume are further complicated by the fact that it is subject to the Coriolis force, and that it entrains ambient water as it rises. Eventually the ISW may become neutrally buoyant and leave the ice shelf base. Some of this ISW makes it to the ice front and becomes an important factor in processes taking place at the ice front (Nicholls et al, 2009), including the formation of Antarctic deep and bottom water. The entire process described in the previous three paragraphs is known as the ice pump.

The energy budget for the ice pump involves complicated thermodynamic interactions, lattice ice energy and the non-linear equation of state of sea water (Millero, 1978; Holland and Jenkins, 1999; Hellmer and Olbers, 1989). However, at the most basic level, the ice pump process can be seen as being a buoyancy driven circulation forced by the injection of dense water (HSSW) at the ocean surface, and the injection of fresher water (ISW) at depth, which effectively injects potential energy

into the system. By neglecting the temperature variations and thermodynamics, as we have in our study, one can focus on how these buoyancy sources, the structure of the bottom topography and the structure of the ice shelf determine the flow.

The dynamical effects of the ice shelf topography were studied by Determan and Gerdes (1994) and Grosfeld et al (1997). These studies used numerical models to demonstrate that the ice front has a major effect on the flow, and essentially blocks waters from the open ocean from entering the cavity as a result of a potential vorticity constraint. More recent work has shown that this blocking effect is not as powerful as previously supposed (Holland and Jenkins, 2001) and depends on the stratification of the water arriving at the ice front (Makinson et al, 2005). Recent work has shown that eddies are able to intrude into the ice shelf cavity (Arthun et al, 2013). Furthermore, boundary currents are able to enter and exit the ice shelf cavity quite freely and are able to transport a large volume of water into the cavity (Holland and Jenkins, 2001).

The boundary currents which run into the ice shelf cavity are examples of rotating gravity currents. Rotating gravity currents on a slope have been studied at length both experimentally and theoretically (Cenedese et al, 2004; Etling et al, 2000; Lane-Serff and Baines, 1998; Zatsepin et al, 1996; Killworth et al, 1984; Cossu et al, 2010). The problem of rotating density currents along a solid lateral boundary has also been studied (Griffiths, 1986; Griffiths and Hopfinger, 1983; Stern et al, 1982). These large scale topographically steered gravity currents are important since they control a large proportion of the flux into the ice shelf cavity, and can also affect the properties of the ambient fluid in the ice shelf cavity

via entrainment (Wahlin et al, 2008). However, it is unknown how these gravity currents respond to the presence of an ice shelf, which acts as an upper boundary.

In nature, bottom and ice shelf topographies are important in steering the dense water into the ice shelf cavity, and fresh water out of the ice shelf cavity. Observations indicate that the main pathways for HSSW are through depression in the ocean bottom and along land boundaries (Nicholls et al, 2003; Mathiot et al, 2012). Similarly, buoyant ice shelf water leaving the ice shelf cavity is steered by the bathymetry and by the ice shelf geometry (Holland and Feltham, 2006). The ice shelf topography also plays a role in directing ocean jets, which run along the ice front, outside of the ice shelf cavity (Nunez-Riboni and Fahrbach, 2010; Foldvik et al, 2001). The role that these topographically steered jets play in the exchange of water into and out of the cavity is still unknown. In real-world ice shelves, easterly winds at the ice front are involved in driving the jets, which further complicates the dynamics.

In this study, a laboratory experiment is created to simulate the density driven currents involved in the ice pump. The first aim of the experiment was to observe how water passes into and out of the ice shelf cavity and estimate the flux of dense water which moves into the cavity as a gravity plume along the lateral boundary. Secondly, the experiment aimed to determine how the flux of dense water into the cavity, the flux of fresh water out of the cavity, the circulation inside the cavity, and the structure of the gravity plumes moving into and out of the cavity, are affected by varying the buoyancy fluxes injected into the system, and varying the geometry of the ice shelf cavity.

In the experiment described below, the flow was visualized using Particle Image Velocimetry (PIV) (Adrian, 2005) and Laser Induced Florescence (LIF) (Houcine et al, 1996) . Recent advancements in flow visualization in laboratory experiments has meant that laboratory experiments can be used for quantitative rather than qualitative geophysical applications. However, in recent years the use of laboratory experiments to study ocean-ice interaction has not been popular. One of the purposes of this study is to present observations and lessons from a first effort obtaining quantitative data to help understand sub-ice shelf circulation.

Section 2 explains the experimental setup, measurement methods and calibration process. The results of the experiments are outlined in Section 3. Section 4 contains a brief discussion of the results. Section 5 contains some concluding remarks.

2.2 Experimental setup and data collection

The experiment described below was performed on a rotating platform in the Coriolis laboratory, in Grenoble, France. In this section we explain the experimental setup, the different types of experimental runs, and comment on the data collected.

2.2.1 Experimental Setup

The experimental setup was motivated by the descriptions of the ‘ice pump’ described in the introduction (MacAyeal, 1984; Jenkins, 1991; Holland and Feltham, 2006). Figure 2.2, which shows our experimental setup, can be compared to Fig. 2.1 which is a schematic of the process we were trying to mimic. The upper panel in Fig. 2.2 shows a side view of our experimental domain. The plan view of the experiment is shown in the lower panel of Fig. 2.2. The base of the experimental domain consisted of the cavity continental slope with a slope of 0.1 and a level continental shelf. These are shown from left to right in the upper panel in Fig. 2.2. An ice shelf was created using Plexiglas and was positioned above the sloping bottom as shown in Fig. 2.2. Between the ice shelf and slope there was a region which we refer to as the ice shelf cavity.

The entire domain shown in Fig. 2.2 was placed inside the large 13m rotating platform which rotated counter-clockwise with a period of 60 seconds. The Grenoble turntable was only able to turn in the counter-clockwise direction, so the experiment simulated a northern hemisphere ice shelf (i.e. $f > 0$). Since the experiment was meant to model the Antarctic ice shelves, we will refer to the left most side of Fig. 2.2 as the southern most point (we are free to make this choice as we have constant rotation everywhere in the domain). The other directions are named accordingly. The x, y and z axes are defined using the standard direction convention: the positive direction on the y-axis is north, the positive direction on the x-axis is east, and the positive direction on the z-axis is up.

At the southern end of the ice shelf cavity, we constructed a barrier, which we

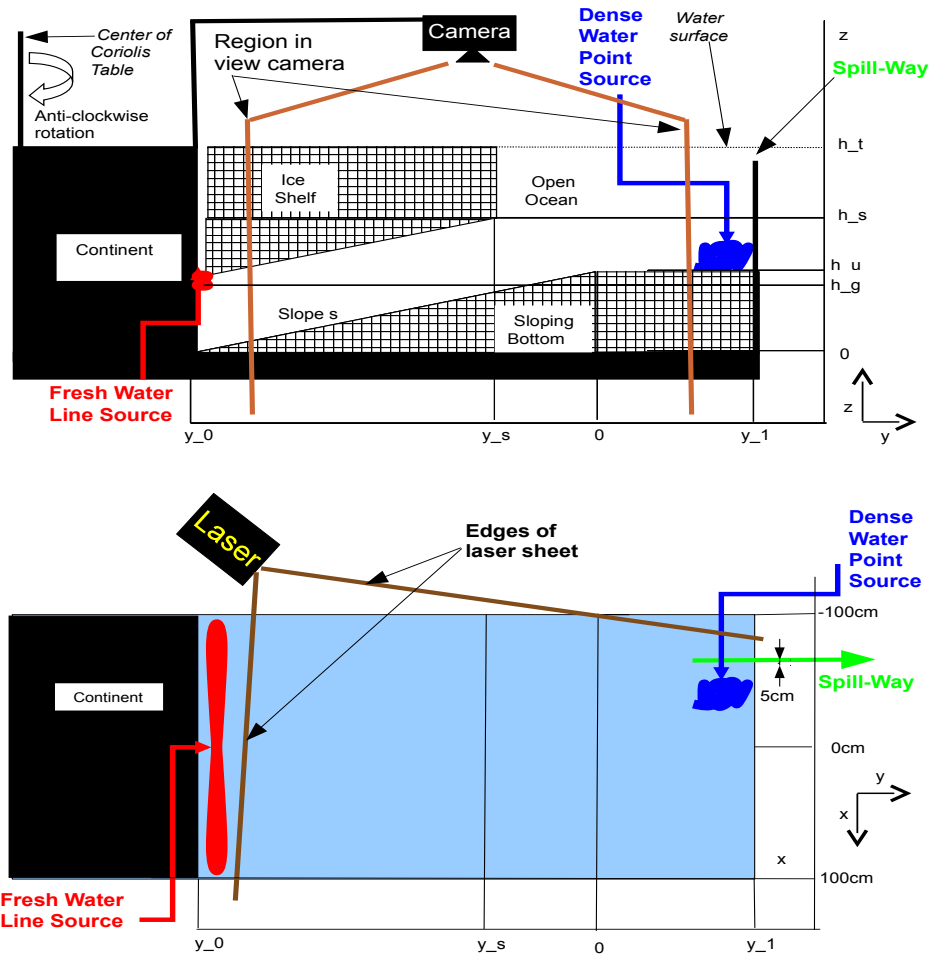


Figure 2.2: The experimental setup for our experiment. The upper panel shows the side view of the experiment. The lower panel shows the plan view of the experiment. The red and blue marks indicate the position of the fresh and dense water sources, respectively. The y -axis indicates latitude, the x -axis indicates the zonal direction. The positive y direction points north and the positive x -axis points east.

refer to as the continent. The point where the ice shelf base meets the continent is referred to as the grounding line. The height of the grounding line is denoted h_g . At the northern end of the experimental setup, there was a barrier to keep the fluid inside the experimental domain. The domain was 400cm from north to south, 200cm from east to west and 56cm from top to bottom.

Two water masses were used in the experiment: Fresh water with density of $1000 \frac{\text{kg}}{\text{m}^3}$ and dense water with a density of $1004 \frac{\text{kg}}{\text{m}^3}$. These densities were chosen for the dense and fresh water since the difference between the densest and freshest waters found under Antarctic ice shelves is $\sim 4 \frac{\text{kg}}{\text{m}^3}$. The dense water was seeded with Rhodamine dye, which was used to measure the water density during the experiments (see section 2.4). Both water masses were seeded with micrometer sized particles which were used to calculate the velocity fields during the experiment (see section 2.4). At the beginning of the experiment, the entire domain was filled with mixture of the fresh and dense water. The experimental results were insensitive to the ratio of this initial mixture since measurements were only made after the system had reached equilibrium.

A fresh water line source was placed along the grounding line. When this source was switched on, it created a plume of buoyant fresh water which rose up along the ice shelf base. This plume represented the Ice Shelf Water (ISW) discussed in the previous section. The water injected at the fresh source was injected vigorously creating some mixing. The fresh water source contained some bubbles that we were unable to prevent during the experiment, but these did not materially affect our results. Just outside of the ice shelf cavity, we placed a dense water point source

near the north-west corner of the domain. The dense water injected here formed a gravity current which rolled down the slope and into the cavity. This dense water represented the High Salinity Shelf Water (HSSW) discussed in the previous section. A sponge was used to limit the mixing and bubbles caused by injecting the dense water. A point source was used for the the dense water injection since the production of HSSW is often a localized process (Mathiot et al, 2012; Arthun et al, 2013). A line source was used for the fresh water source since melting occurs all along the grounding line.

At the north-west corner of the domain, there was an opening which we refer to as the spill-way. Water was allowed to drain out of the experimental domain through the spill-way. In this way, the total amount of water in the domain remained fixed.

The experiment was spun-up for two hours to be in solid body rotation before the dense and fresh sources were turned on. After the dense and fresh sources were turned on, there was an unsteady period where the system adjusted to a new equilibrium. All measurements and analysis were performed after this adjustment had been completed and the system was in a statistically steady state. The waiting time after the dense and fresh sources were turned on, was approximately one hour, which is greater than the flushing time for the system, T_f , and the spin-up time, T_s (see Section 2.2.1). Measurements of the density driven circulation were observed using a camera positioned above the experimental domain. In the different experimental runs measurements were taken for between 4000 and 10000 seconds.

Experiment	Dense Flow Rate	Fresh Flow Rate	h_g (cm)	h_s (cm)
Control Run	20.05 l/min	20.00 l/min	20.0	41.3
Fresh Run	10.04 l/min	30.00 l/min	20.0	41.3
Dense Run	30.63 l/min	10.00 l/min	20.0	41.3
Pinch Run	19.93 l/min	21.67 l/min	9.0	43.8
Stretch Run	20.30 l/min	21.67 l/min	30.0	36.3
Big Gap Run	20.00 l/min	20.00 l/min	29.7	51.0
Little Gap Run	20.00 l/min	20.00 l/min	10.0	31.3

Table 2.1: Parameters used in the experimental runs

Three tests were performed to explore the effect of ice geometry and buoyancy sources on the ice shelf circulation:

- **Thickness Investigation:** The thickness of the ice shelf cavity was varied, while the slope of the ice shelf, and the buoyancy sources, were kept constant.
- **Gradient Investigation:** The gradient of the ice shelf was varied while the buoyancy sources were kept constant.
- **Buoyancy Investigation:** The buoyancy sources were varied, while the ice shelf geometry was kept constant.

In the rest of the paper, we refer to these three investigations as the Thickness Investigation, Gradient Investigation and Buoyancy Investigation. The term *experimental runs*, is used throughout the rest of the paper to refer to individual simulations which made up these three *investigations*. Each investigation consisted of three experimental runs. The number of experimental runs was limited by the time taken to run an experiment and the complexity of the experimental setup. The same Control Run was used for all three investigationa meaning that in total, seven different experimental runs were performed.

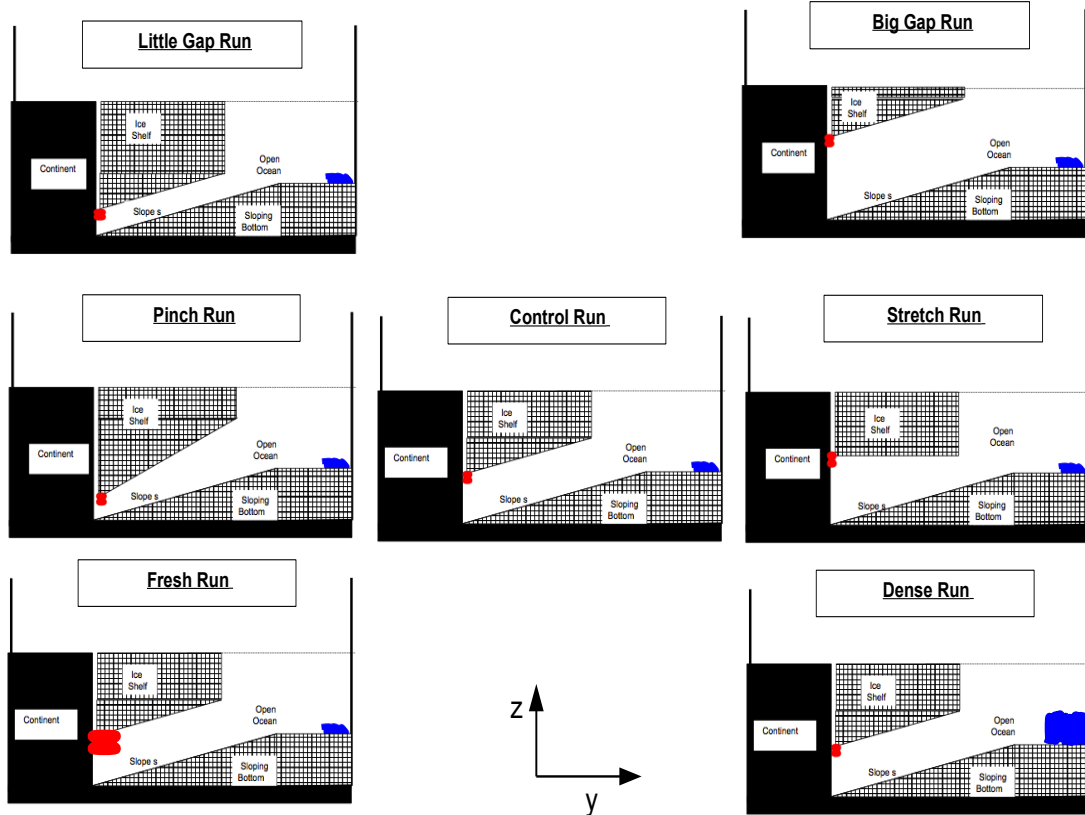


Figure 2.3: Summary of seven different experiments runs performed. The seven experimental runs are divided into three experiments. All three experiments used the same Control Run, which is positioned in the center. The top row shows Thickness Investigation where the ice shelf cavity thickness was varied. Row two shows Gradient Investigation where the slope of the ice shelf was varied. Row three shows Buoyancy Investigation, where the control geometry was used, but the fluxes of the dense and fresh water sources were varied.

Figure 2.3 shows a schematic of the experimental runs performed. The three investigations are shown from left to right in rows one, two and three of Fig. 2.3, with the Control Run in the center. The various experimental runs are named in Fig. 2.3. These names are used throughout the discussion below. Different geometries were achieved by changing h_g and h_s . All experimental runs used $y_0 = -250\text{cm}$, $y_1 = 169\text{cm}$, $y_s = -38\text{cm}$, $h_u = 25\text{cm}$, and $h_t = 56\text{cm}$. Table 1 has a list of the experimental parameters used in the various experimental runs.

2.2.2 Non-dimensional numbers:

2.2.2.1 Non-dimensional numbers showing dynamic similarity:

The large Coriolis facility was used rather than a smaller rotating platform as the large experimental domain meant that we were able to better resolve the boundary currents in the experiment. The largeness of experimental domain also allowed us to achieve non-dimensional numbers which were more similar to the real world.

The Rossby number of our system was $R_0 = \frac{U}{fL} = \frac{10^{-2}}{0.2*1} = \frac{1}{20}$. Here we use the fact that $f = \frac{4\pi}{T} = \frac{4\pi}{60} \approx 0.2$. We use $L=1\text{m}$, which half of the width of the domain and $U = 10^{-2}\text{m/s}$, which was a typical velocity observed in the experiments. The real-world Rossby number can be estimated as $R_{ocean} = \frac{U}{fL} \approx \frac{10^{-1}}{10^{-4}*10^5} = 10^{-2}$ where the estimate of U comes from (Nicholls, 1996). The smallness of the Rossby number in both cases mean that the system was likely to be close to geostrophic

balance.

Since we were using a large tank, we were able to achieve a small aspect ratio $\alpha_0 = \frac{H}{L} \approx \frac{0.5\text{m}}{4\text{m}} \approx 10^{-1}$. The length of the tank was 4m. The aspect ratio of the real-world ice cavities is $\alpha_{ocean} \approx \frac{10^3\text{m}}{10^5\text{m}} = 10^{-2}$. While our aspect ratio is an order of magnitude larger than that of the ocean, the both systems are strongly influenced by the smallness of their aspect ratio.

The frictional Ekman layer thickness scales like $\delta = \sqrt{\frac{\nu}{f}}$. Using the viscosity of water $\nu \approx 10^{-6}\text{m}^2\text{s}^{-1}$, we estimate a molecular Ekman layer thickness of $\delta_{mol} = \sqrt{\frac{\nu}{f}} \approx \sqrt{\frac{10^{-6}}{\frac{1}{5}}} = 2.2 \times 10^{-3}\text{m} = 2.2\text{mm}$. This provides a lower bound of the Ekman layer thickness. To get an upper bound on the Ekman layer thickness, we use a typical Eddy viscosity found in the ocean, $\nu = 10^{-2}$. This gives us $\delta_{tur} = \sqrt{\frac{\nu}{f}} \approx \sqrt{\frac{10^{-2}}{\frac{1}{5}}} = 22\text{cm}$. However, since our system was likely to be much less turbulent than the ocean, it is probable that the eddy viscosity will be an order of magnitude or more smaller, resulting in an Ekman layer thickness, δ , between 1cm and 10cm, although this is hard to predict a-priori. In the experimental results shown below, the Ekman boundary layer can not be seen. This is especially apparent in the dense and fresh plumes where the fastest speeds are close to the lower and upper boundaries, respectively. This implies that the Ekman layer thickness is likely to be smaller than 2cm, the resolution of the velocity measurements.

The Reynolds number in the experiment is $Re = \frac{UL}{\nu} = \frac{10^{-2}*1}{10^{-6}} = 10^4$. Since the transition to turbulence typically occurs for $2300 < Re < 4000$ (in a pipe flow) (Holman, 2002), the fluid in our experiment was likely to have been turbulent.

While the Reynolds number is smaller than typical Reynolds numbers found in the ocean, it is comparable to Reynolds numbers used in numerical models. The Froude number for the gravity plumes in the experiment is $F = \frac{U}{\sqrt{gH}} = \frac{10^{-2}}{\sqrt{10^{-2} \cdot 10^{-1}}} \sim 0.3$, which is slightly subcritical.

The spin-up time for a rotating tank is $T = \sqrt{\frac{L^2}{\nu}\Omega}$ (Greenspan and Howard, 1963). In our experiment the spin-up time is estimated as $T = \sqrt{\frac{L^2}{\nu}\Omega} = \sqrt{\frac{1m^2}{10^{-6}m^2s^{-1}\frac{2\pi}{60}}} \sim 10^{\frac{7}{2}}s \sim 3000s$. The experiments were allowed to spin up for two hours to reach solid body rotation before the flow was turned on. The experimental domain contained $\sim 2m^3$ of water. The combined flux of the dense and fresh water sources were 40 liters per minutes ($\sim 0.66 \times 10^{-3}\frac{m^3}{s}$). This meant that the flushing time for the system was $T_f \sim 3000s$.

2.2.2.2 Non-dimensional parameters varied in experiments:

The changes in geometry and buoyancy used in the three investigations can be described by three non-dimensional numbers: G_t , G_s and G_b . These are described below::

We define G_t as the ratio of the thickness of the water column inside and outside the ice shelf cavity at the ice front. Since the height of the ocean floor at the ice front is $h_u - |y_s|s$, we define

$$G_t = \frac{h_s - (h_u - |y_s|s)}{h_t - (h_u - |y_s|s)} \quad (2.1)$$

Here s is the slope of the ocean bottom. G_t gives a measure of the change of water column thickness which occurs as a column of fluid moves across the ice front.

G_s is defined to be the average meridional gradient of the ice cavity thickness. In our setup, G_s is given by

$$G_s = \frac{(h_g - 0) - (h_s - (h_u - |y_s|s))}{|y_0 - y_s|} \quad (2.2)$$

G_s gives a measure of how the cavity water column thickness changes as a column of fluid moves from the grounding line to the ice front.

G_b is defined as the ratio of the mass flux anomaly caused by injecting dense and fresh water injected into the system.

$$G_b = \frac{\Delta M_d}{\Delta M_d} \quad (2.3)$$

If the ambient water in the system has a density of ρ_a , the dense water has a density of ρ_d , and the fresh water has a density of ρ_f , then the mass flux anomalies are give by

$$\Delta M_d = (\rho_d - \rho_a)Q_d \quad (2.4)$$

$$\Delta M_f = (\rho_a - \rho_f)Q_f \quad (2.5)$$

Here Q_d and Q_f are the fluxes of water injected at the dense and fresh source, respectively. The density of the dense and fresh waters injected into the system were, $\rho_d = 1004 \frac{\text{kg}}{\text{m}^3}$ and $\rho_d = 1000 \frac{\text{kg}}{\text{m}^3}$. We set $\rho_a = \frac{(\rho_d + \rho_f)}{2} = 1002 \frac{\text{kg}}{\text{m}^3}$.

In the Control Run we used $G_t = 0.58$, $G_s = 0.00$ and $G_b = 1.0$. Values were picked in order to make the control run analogous to the Ross Ice Shelf. The average ice draft of Ross Ice Shelf at the ice front is $\sim 300\text{m}$, while the continental shelf depth is $\sim 700\text{m}$ below sea level (Davey, 2004). This gives $G_t \sim \frac{400\text{m}}{700\text{m}} \sim 0.57$. At 180°W , the Ross Ice Shelf cavity thickness changes by 300m over a distance of 300km between 79°S and 82°S (Davey, 2004). This implies $G_s \sim \frac{1}{1000}$.

To calculate G_b we use the freshwater flux in the Ross Sea caused by sea ice production, evaporation, precipitation and the basal melt beneath the Ross Ice Shelf. Assmann et al (2003) estimated the total flux of fresh water from basal melt beneath the Ross Ice Shelf to be 5.3mSv . The total fresh water flux on the Ross Sea continental shelf (excluding the contribution of melt water from under the ice shelf) was estimated to be -26.6mSv . Here $1\text{mSv} = 10^3 m^3 s^{-1}$. Taking the ratio, this gives $G_b \sim 5$. However, a large portion of the dense water created in the Ross Sea is exported off the continental shelf and does not influence the dynamics under the ice shelf (Orsi et al, 2002; Gordon et al, 2009). Because of this uncertainty in the total amount of fresh water extraction which affects the ice shelf dynamics, we note that $G_b \sim O(1)$, and used $G_b = 1$ in our Control Run. The Dense Run and Fresh Run are used to examine the effect of changes in G_b on the circulation beneath the ice shelf.

The values of G_t , G_s and G_b used in the three different investigations are shown in Table 2. Values of G_t , G_s and G_b were varied in order to examine the sensitivity of the circulation to changes in these parameters. These experiments are motivated

by the fact that paleoclimate records show that the geometry and basal melt of the Ross Ice Shelf has changed significantly in the past (Conway et al, 1999). We are interested in how the circulation beneath the Ross Ice Shelf might have responded to such changes. Furthermore, these experiments are also of interest in comparing different ice shelves around Antarctica, which have differing geometries and buoyancy fluxes. The Ronne-Filchner Ice Shelf, for example, has a large ice draft at the ice front and therefore has a smaller value for G_t , while the ice front draft of the McMurdo Ice Shelf is only 20m, and hence $G_t \sim 1$ (Stern et al, 2013). Pine Island Glacier has a large value for G_s since it has an ice shelf which is many time steeper than the Ross Ice Shelf, resulting in a large change of cavity thickness over a shorter distance. G_s can also be negative locally when there is steep bottom topography. The large flux of ISW associated with rapidly melting ice shelve likely results in a small value of G_b . Changing values of G_b could be relevant to future climate change scenarios.

2.2.3 Data collected during the experiments

A camera was placed above the experimental domain, and a laser was placed south-west of the domain (see Fig. 2.2). The walls of the domain were constructed using plexiglas to allow the laser light to pass through. The laser created a horizontal plane of light, which allowed the camera to take pictures of the fluid illuminated by the laser. A mirror was placed on a carriage which could move up and down, and direct the laser light to different levels so that we were able to get images in 23 different horizontal planes. The camera position remained fixed 5m above the ex-

Thickness Investigation			
Experimental Run	G_t	G_s	G_b
Little Gap Run	0.29	0.00	1.0
Control Run	0.58	0.00	1.0
Big Gap Run	0.86	0.00	1.0

Gradient Investigation			
Experimental Run	G_t	G_s	G_b
Pinch Run	0.65	-0.06	0.9
Control Run	0.58	0.00	1.0
Stretch Run	0.43	0.07	0.9

Buoyancy Investigation			
Experimental Run	G_t	G_s	G_b
Fresh Run	0.58	0.00	0.3
Control Run	0.58	0.00	1.0
Dense Run	0.58	0.00	3.1

Table 2.2: Non-dimensional parameters used in the experimental runs. The experimental runs have been grouped into three groups corresponding to the Thickness Investigation, the Gradient Investigation and the Buoyancy Investigation. The same control run was used for all three investigations.

perimental domain, rotating with the table. The camera was sufficiently far from the domain that the camera focus was not significantly affected by moving the laser sheet. At each level, 3 images were taken at a frequency of 3Hz. The images at different heights were taken 3 seconds apart. This meant that the images at every horizontal plane had a time separation of 69 seconds. The size of the region in the view of the camera was 226cm in the north-south direction and 200cm in the east-west direction. The entire width of the domain (including the plumes on both sides of the domain) was in the sight of the camera, while just over half of the length of the domain (from north to south) was captured by the cameras. The fresh and dense sources were not in the field of view.

The fluid in the experiment was seeded with micrometer sized particles and the dense water injected at the dense source was mixed with a known concentration of Rhodamine dye. The Rhodamine dye and the seeded particles were illuminated by the laser and showed up in the images captured by the camera. These images were used to perform Particle Image Velocimetry (PIV), which involves finding the peak correlations between consecutive images in order to calculate horizontal velocity fields. Three images were used to calculate each velocity field. This was done by finding the peak correlation of each image with the other two, and averaging the three velocity fields. This technique helped us improve the quality of the velocity fields calculated. Multiple rounds of correlation were performed with velocity estimates from the previous round of correlations being used to refine the search parameters for subsequent correlation searches. The camera images were also used for Laser Induced Florescence (LIF), which involves using the intensity of the fluoresced light to find the concentration of Rhodamine dye in a fluid parcel, from which one can find the density of the fluid. The laser being placed on the south-west of the domain meant that the quality of the data on the side closest to the laser was better than the data on the far side. This meant that the quality of data in the dense plume was higher than the data quality in the buoyant plume.

A complex calibration process was used to convert the photographs taken during the experiments into velocity fields and concentration fields. Complications were caused by the fact that we had to mask out the ice shelf and solid geometries during the PIV correlation procedure. The program UVMAT was used to do the correlations for the PIV (further information about UVMAT software can be

found at <http://coriolis.legi.grenoble-inp.fr/spip.php?rubrique14>). The correlation percentages indicate the quality of the velocity field at a particular point. These percentages confirm that the highest quality velocity data was on the western side of the domain, near to the laser.

The procedure used for the calibration of the concentration had to account for the exponential decay of light as it passes through the rhodamine dye. The decay coefficients were calculated for each geometry separately using pictures taken with the entire domain filled with dense water (i.e. concentration of Rhodamine dye equal to 1 everywhere).

2.2.4 Quality of data after calibration

Figure 2.4 shows a typical concentration field obtained in the experiment. This example was taken from the Pinch Run, at $z = 30.5\text{cm}$. A horizontal cut is marked on the figure and the density at the cut is shown below. The dense and buoyant plumes discussed in the previous sections, can be seen along the left and right side of the figure, respectively. The velocity of the dense and buoyant plumes are shown in Box1 and Box2, where velocity is shown by the direction and size of the arrows, and the concentration is given by the color of the arrows. We define the dimensionless concentration $c = \frac{\rho - 1000}{4}$, which is the proportion of a grid box filled with Rhodamine dye. Since the Rhodamine dye is a proxy of density, c can be thought of as being normalized density, where $c = 1$ is the densest water in the domain (i.e. $\rho = 1004\text{kg m}^{-3}$) and $c = 0$ is fresh water (i.e. $\rho = 1000\text{kg m}^{-3}$).

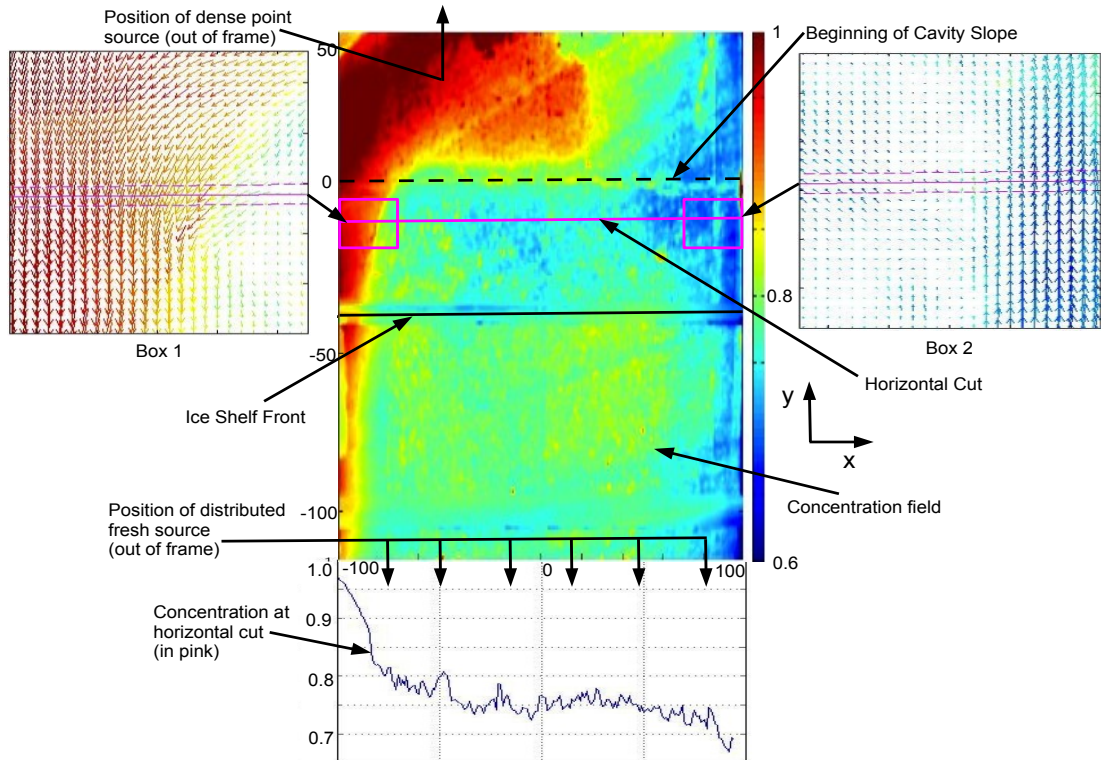


Figure 2.4: A typical concentration field on the x - y plane taken from the Pinch Run, at $z = 30.5\text{cm}$. The positive y direction points north and the positive x -axis points east. The concentration of Rhodamine dye in a grid box gives us the density of the fluid. A horizontal cut is marked in pink and the concentration at the cut is shown in the graph below. The velocity of the dense and buoyant plumes are shown in Box1 and Box2, where velocity is shown by the direction and size of the arrows, and the concentration is given by the color of the arrows.

The horizontal velocity fields have a horizontal spatial resolution of 1cm and a vertical resolution of approximately 2cm. The domain where we have data consist of 199 points in the x -direction, 226 points in the y -direction and 23 points in the z -direction (the vertical levels were not uniformly spaced). Again, the temporal resolution of the data is 69 seconds.

The accuracy of the concentration fields, c , is between 5 and 10 percent. Since the density is always in the range $1000 \frac{kg}{m^3} < \rho < 1004 \frac{kg}{m^3}$, this is equivalent to having an accuracy of between 0.2 and 0.4 kg m⁻³ in the density field. The accuracy is improved by averaging over time and space. The accuracy of the velocity field is approximately 5 percent. The major errors in the concentration field are caused by reflections of the laser off the ice front and the sloping bottom. There are also some reflections caused by bubbles, which entered the domain near via the fresh water source, and reflections off the PIV particles.

Figure 2.4 captures some of the main features of the flow which show up in the time-mean plots. These are discussed further in Section 3.

2.2.5 Further comments about the experimental setup

The experiment was performed inside a plexiglass tank with vertical walls running along the sides of the domain. This setup was preferred to axisymmetric model since in the real-world most of the large ice shelves are bounded by land on their eastern and western sides. While land boundaries on the flanks of the ice shelves are not vertical in the real world, the simplified geometry used in this

experiment captures the broad features of the larger ice shelves, and allows for boundary currents to run along the sides of the domain. The presence of a northern boundary in the experimental setup gives rise to a cyclonic circulation offshore of the ice front, which is analogous to the westward coastal current that pervades the continental shelf offshore of Antarctic ice shelves.

The dense source was placed on the continental shelf close to the bottom of the water column. In nature the production of dense water occurs at the top of the water column. Having the dense source at the bottom of the water column meant that we could not study the convection process, however, it allowed us to focus on the the intrusion of dense water into the ice shelf cavity.

It has been observed that the injection of dense water into a rotating system, has a tendency to generate a train of traveling baroclinic vortices (Lane-Serff and Baines, 1998; Etling et al, 2000) and results in an unsteady flow. This unsteady flow was observed in our experiment near the dense source. It is probable that the production of HSSW and ISW in nature is also associated with the generation of traveling baroclinic vortices, and unsteady flow, but current real-world observations are too sparse to comment further.

The laser being positioned on the western side of the domain meant that the quality of the velocity and concentration fields in the fresh plume was lower than in the dense plume (which was closer to the light source). This meant that the quality of data in the fresh plume was only good enough for qualitative analysis. This meant that we were unable to estimate the total mass and volume flux into

the cavity since this calculation is sensitive to error in the flux of water through the fresh plume. In future experiments it would be preferable to position the laser differently to ensure high quality data on both boundaries.

2.3 Major features of the flow

In this section we present the main features of the flow observed in the experiment. We begin our analysis by looking at the time mean features of the data. As mentioned earlier, all experimental runs were allowed a spin-up time to reach solid body rotation before the dense and fresh sources were turned on. After the sources were turned on, we again waited for the system to reach a statistically steady state. All time means have been taken over the times where a statistically steady state has been achieved.

2.3.1 Description of results in the Control Run:

The background colors in Fig. 2.5 shows the time-mean, z -mean meridional velocity for the control experiment. The arrows in Fig. 2.5 show the time-mean, z -mean horizontal velocity field. At latitudes $y=-38\text{cm}$ and $y=-97\text{cm}$, the view of the camera was obstructed and we were unable to collect data. The white lines in Fig. 2.5 show the position these data gaps. From this figure, together with figures of the concentration fields (similar to Fig. 2.4), we can infer the main features of the flow: Dense water, which is injected onto the continental shelf by the dense

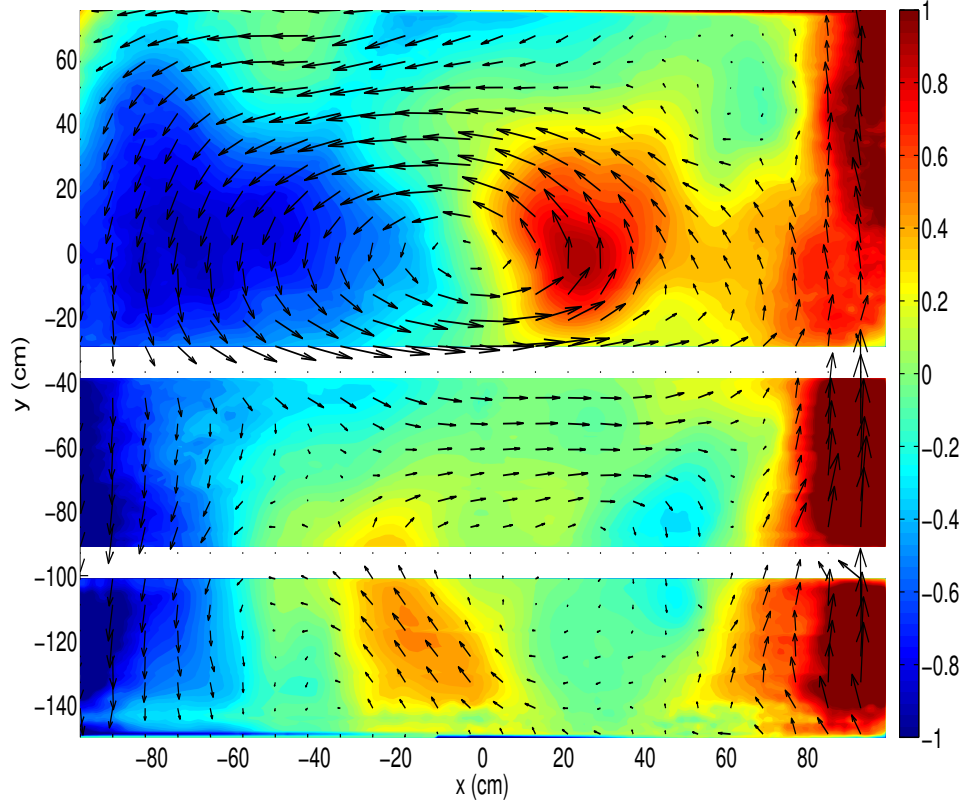


Figure 2.5: The arrows show the time averaged, z -average velocity field for the Control Run. The background colors show the time averaged, z -average meridional velocity on the x - y plane. The positive y direction points north and the positive x -axis points east. The fresh and dense plumes can be seen running along the west and east sides of the cavity, respectively. The continental slope begins at $y=0\text{cm}$ and the ice front is at $y=-38\text{cm}$.

source, diffuses into the surrounding water, remaining close to the bottom. As the dense water spreads southwards, it is acted on by the Coriolis force and veers to the west.

When the dense water reaches the beginning of the slope ($y=0$), it starts to roll

down the continental slope as a gravity plume, which pushes the water even further to the west (recall we are using $f > 0$ with the ice shelf on the south of the domain). In the absence of lateral boundaries, we would expect that the dense water would be redirected so strongly by the Coriolis force that it would eventually move parallel to the continental slope (Griffiths, 1986). In our case, the dense fluid continues to move westward until it reaches the western wall of the domain. The dense water moves as a gravity plume along the western wall of the domain. When it reaches the ice front ($y=-38\text{cm}$), some of the dense water runs along the ice front and recirculates on the continental shelf. The remaining dense water which continues to move along the wall of the domain, enters the ice cavity and continues down the slope towards the grounding line.

The fresh water acts in a similar way but with its direction reversed. The fresh water is injected fairly vigorously and causes some mixing near the grounding line (not seen in Fig. 2.5). Once it is injected, the fresh water begins to flow northward because of its positive buoyancy. As it moves north, it is directed eastward by the Coriolis force and eventually reaches the eastern boundary of the domain, where it moves up the ice shelf slope as a gravity plume. Once the fresh water plume exits the ice shelf cavity, it moves quickly to the surface because of its positive buoyancy, and continues to move northward along the eastern wall. The dense and fresh plumes along the sides of the domain are seen clearly in Fig. 2.5.

There is relatively little motion inside the ice shelf cavity away from the boundary currents. A small clockwise gyre can be seen inside the ice shelf cavity. This gyre is much smaller than the gyre on the continental shelf, and moves in the opposite

direction (i.e. against the rotation).

The vertical structure of the gravity plumes along the lateral boundaries is shown in Fig. 2.6. This figure shows the meridional velocity in the x - z plane at $y=-54\text{cm}$, which is a latitude inside of the ice shelf cavity. The dense and fresh plumes can be seen running into and out of the ice shelf cavity, respectively. Away from the boundary currents, the velocity of the fluid inside the ice shelf cavity is much smaller. Figure 2.6 is similar to Fig. 2.13 in Holland and Jenkins (2001) which simulated the flow under a similar idealized ice shelf using an isopycnic-coordinate ocean model (Holland and Jenkins, 2001).

The fresh water is injected vigorously by a distributed source and tends to mix with the ambient fluid. This results in the fresh plume being more homogeneous than the dense plume, and the density of the fresh plume being closer to the the density of the ambient water. This could account for the steep gradient of the boundary of the fresh plume observed in Fig. 2.6, since decreasing the density gradient across the plume boundary requires an increased slope of the plume boundary in order for the plume to maintain the same geostrophic velocity. However the quality of the data in the fresh plume is not sufficiently high to have confidence that the asymmetry between the dense and fresh plumes, observed in Fig. 2.6, is a robust feature of the system.

Outside of the ice shelf cavity, on the continental shelf, the fluid that does not enter the ice shelf cavity tends to circulate in a counter-clockwise direction, pro-

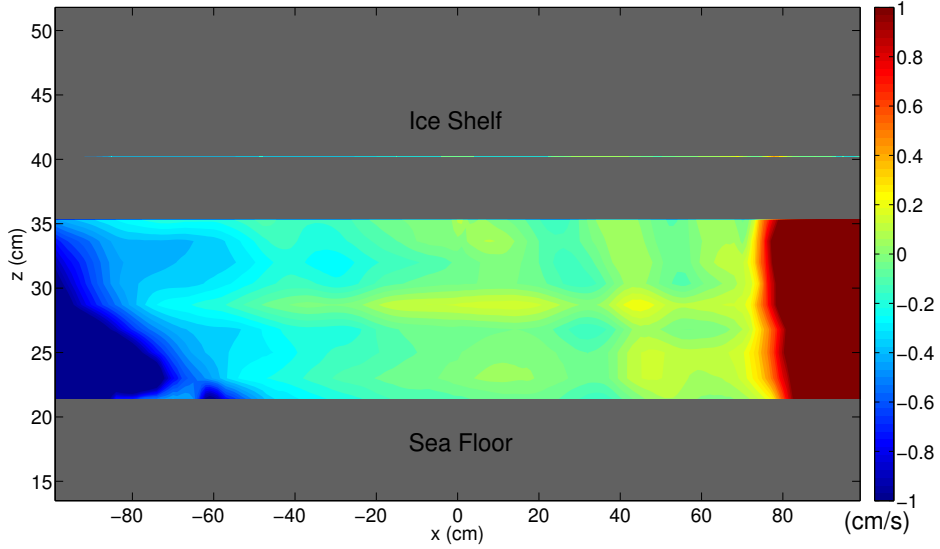


Figure 2.6: The time-mean meridional velocity at $y=-54\text{cm}$, which is a latitude inside of the ice shelf cavity. The dense and fresh plumes can be seen fluxing water into and out of the ice shelf cavity, respectively.

ducing a large gyre with positive vorticity. This gyre on the continental shelf results in a strong zonal flow along the ice front. This jet can be seen in Fig. 2.7 which shows the time averaged, x -mean of the zonal velocity. The jet does not penetrate far into the ice shelf cavity.

Figure 2.8 shows the interior concentration, C_{int} , for the Stretch Run (no concentration data was available for the Control Run). C_{int} is the average concentration of the fluid away from the eastern and western boundaries and is defined as

$$C_{int}(y, z) = \frac{1}{132} \int_{-60}^{72} c(x, y, z) dx \quad (2.6)$$

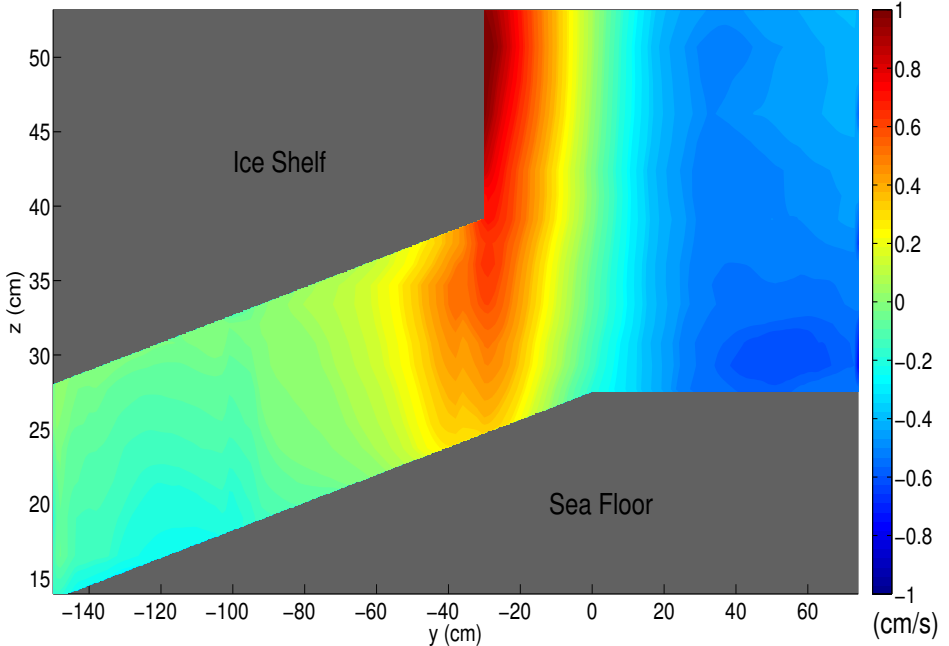


Figure 2.7: The time-mean, x -mean zonal velocity on the z - y plane for the Control Run. A strong eastward jet can be seen moving along the ice front and a return westward flow is seen along the northern wall. There is very little zonal motion inside the ice shelf cavity.

where c is the time-mean concentration and $x = -60$ and $x = 72$ are points which are in the interior and away from the dense and fresh boundary currents. Positions where we were unable to collect data are shown using white lines. Figure 2.8 shows a large density jump across the shelf break.

Since the laser used to illuminate the fluid for the LIF measurements was placed on the south-west of the domain, the shadow cast by the ice shelf was not parallel to the ice shelf front. This implies that the result shown in Fig. 2.8 is unlikely to be a result of calibration error, or a shadow cast by the ice shelf, but rather reflects

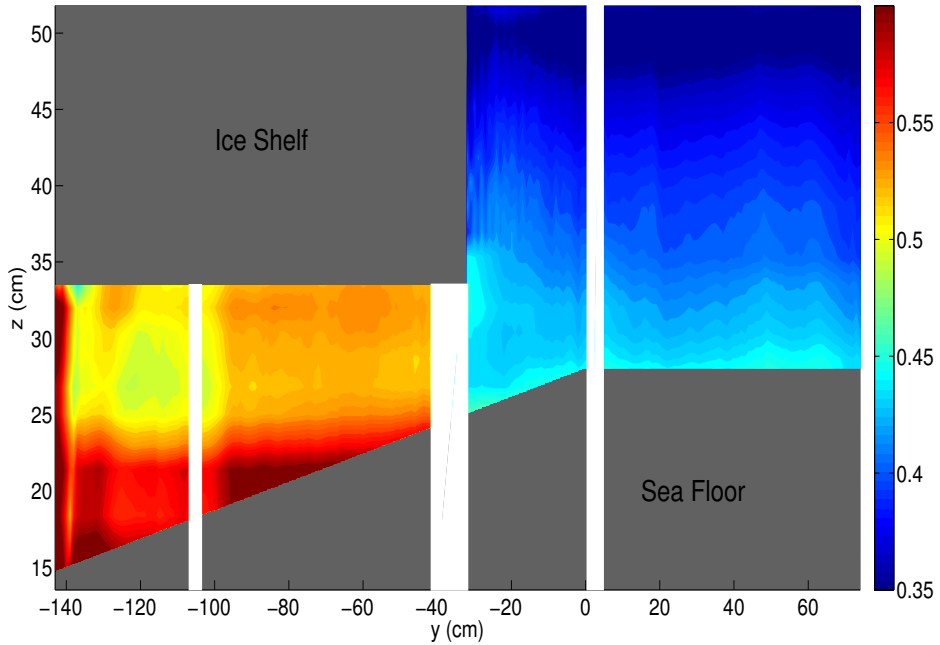


Figure 2.8: The time-mean interior concentration field for The Stretch is shown at different latitudes. The interior concentration is defined as the average concentration between $x = 40$ and $x = 172$. In this figure we can see strong density gradient across the ice front.

a real density gradient across the ice front.

2.3.2 Differences in the experimental runs:

While all the experimental runs had the features described in the section above, changing the ice shelf geometry and the flux of the dense and fresh water sources, caused significant differences in the behavior of the flow. Figure 2.9 shows the vertically integrated meridional volume flux for the experiments involving differ-

ent geometries. This figure highlights the sensitivity of the system to changes in buoyancy sources and ice shelf geometry. The main differences between the various experimental runs are pointed out in this section.

The results of Thickness Investigation: are shown in the top row of Fig. 2.9. Recall, the same Control Run was used for all three investigations, and is shown in the center of Fig. 2.9. The Little Gap Run, has almost no motion inside the ice shelf cavity, and very little flux into the cavity through the dense boundary currents. Most of the motion in this run was confined to the continental shelf. In contrast, in the Big Gap Run, we see that there is a larger flux of dense water into the cavity through the dense plume and more motion inside the ice shelf cavity. Furthermore, very little water is recirculated on the continental shelf along the ice front, meaning that the jet along the ice front is largely reduced, and the gyre offshore of the ice shelf disappears completely. The Control Case is an intermediate case which has some flux of water into the cavity, but still has a substantial jet running along the ice front.

The results from Gradient Investigation are shown in the second row in Fig. 2.9. The results of this investigation indicates that the gradient of the water column thickness in the ice shelf cavity has a strong influence on the circulation. The Stretch Run run is particularly noteworthy in that it has a lot of motion inside the ice shelf cavity. The gyre on the continental shelf in the Stretch Run is less strong. In contrast, the Pinch Run has relatively little movement inside the ice shelf cavity, but has a strong gyre on the continental shelf. The Control Run is again an intermediate case with some motion away from the boundary currents

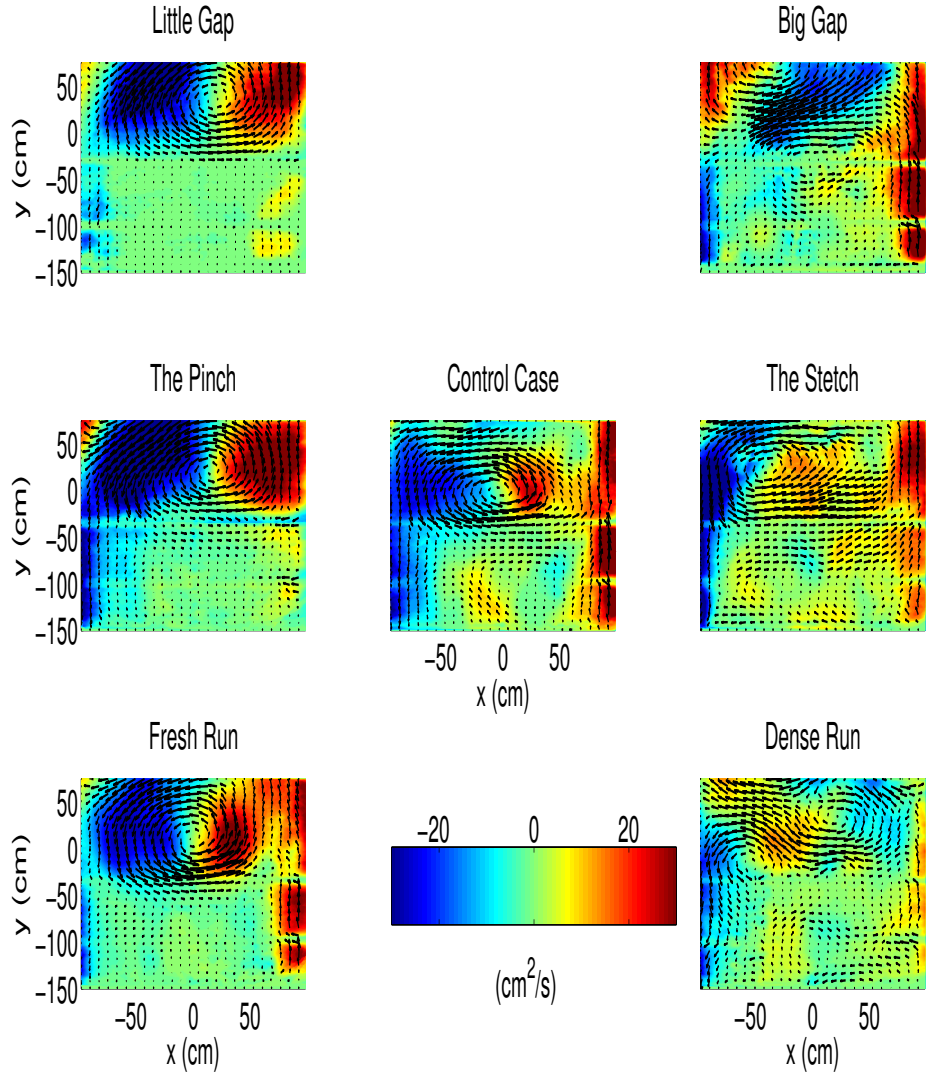


Figure 2.9: The time-mean vertically integrated meridional volume flux for all the experimental runs. The arrows indicate direction and magnitude of the integrated volume horizontal flux. The figure shows how changing the geometry of the ice shelf and the dense and fresh sources has an effect significant on the circulation inside the ice shelf cavity. The three experimental runs in the column on the left of the figure all systematically show a more intense circulation on the continental shelf, and less intense cavity circulation, compared to the Control Run.

inside the ice shelf cavity and a reasonably strong gyre on the continental shelf.

We propose that the slope of the ice shelf controls the motion in the ice shelf cavity via the following mechanism: Fresh water is injected into the system vigorously by a distributed source at the grounding line. The injection of the fresh water results in strong mixing near the fresh water source and causes the fluid columns near the fresh water source to largely barotropic. As a columns of fresh water drift northwards, the geometry of the ice shelf forces the column thickness to change, resulting in the production of vorticity. In the case of the Stretch Run, the fluid column thickness is decreased as a water column moves northwards, which generates negative vorticity. This acts in the same direction as the flow seen in the Control Run and increases the motion inside the cavity. In the Pinch Run, the fluid column thickness is increased when moving northwards. This generates positive vorticity which opposes the fluid motion seen inside the ice cavity in the Control Run, and suppresses motion inside the cavity.

The results of Buoyancy Investigation are shown in the bottom row of Fig. 2.9. The Fresh Run has a strong gyre on the continental shelf, but very little motion inside the ice shelf cavity. The Dense Run has a much smaller gyre on the continental shelf and has much more motion inside the ice shelf cavity. As expected, the fresh water plume is large in the Fresh Run, and small in the Dense Run, while the dense water plume is large in the Dense Run and small in the Fresh Run. The control case is an intermediate case with equally sized boundary currents, some motion inside the cavity, and a intermediate strength gyre on the continental shelf.

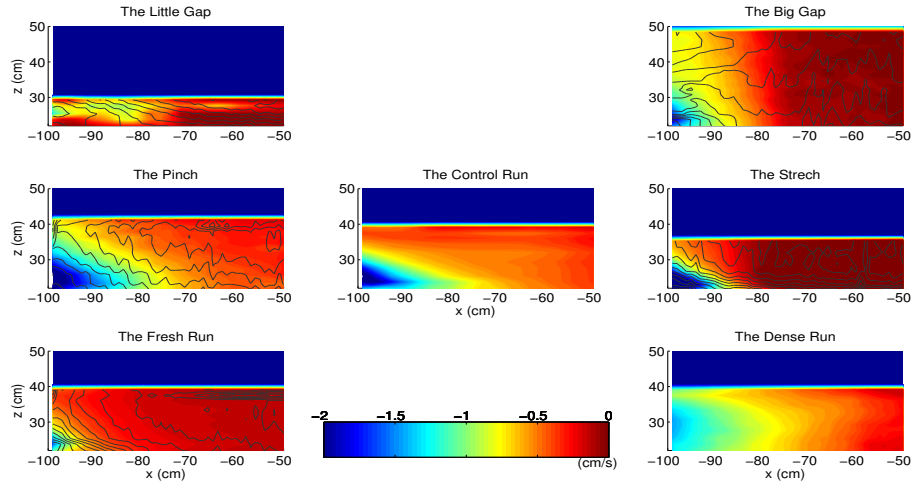


Figure 2.10: The time-mean, meridional velocity (cm s^{-1}) of the dense plume at $y = -54\text{cm}$ is plotted for each experiment. Only the negative velocity has been plotted to allow the plume to be seen more clearly. Density contour lines have been plotted over the top.

2.3.3 Shape of the dense plume

In this section we look more carefully at the structure of the dense plume for the different experimental runs. In Fig. 2.10 we plot the time-mean meridional velocity for each experimental run at $y = -54\text{cm}$, which is a latitude just inside the ice shelf cavity. The results are again positioned with Thickness Investigation shown in the top row, Gradient Investigation in the second row, and Buoyancy Investigation in the bottom row.

In almost all experimental runs the fastest moving and densest part of the plume is against the wall near the bottom. The velocity is seen to decay away from the wall toward the edge of the plume. The concentration (normalized density) con-

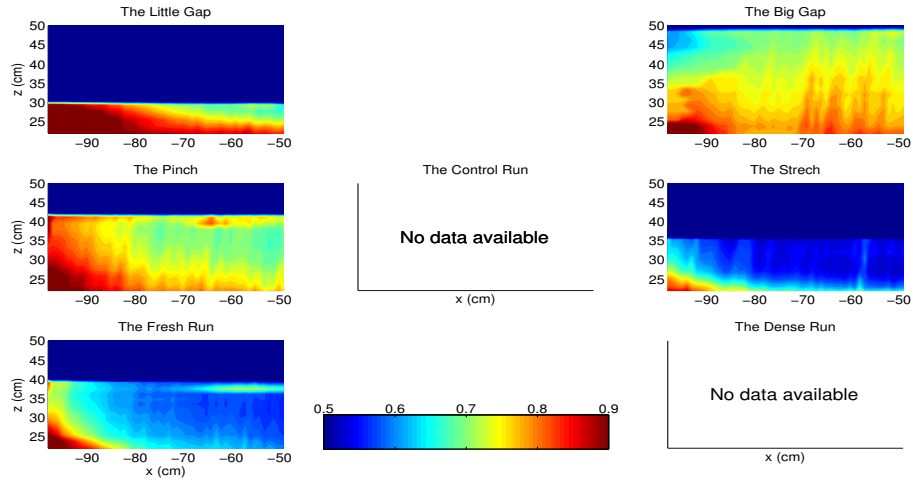


Figure 2.11: The time-mean concentration contours of the dense plume at $y=-54\text{cm}$ is plotted for each experiment.

tours have been plotted on top of Fig. 2.10. Figure 2.11 shows the time-mean concentration for the same slice of fluid. The concentration fields for the Control Run and the Dense Run are not plotted since there were problems with the calibrations. Comparing Fig. 2.10 and Fig. 2.11, one can see that the velocity contours lie parallel to the density contours in the densest part of the plume. The velocity contours of the plume take on a triangular shape near to the wall and then become more vertical as one moves away from the boundary. In all experimental runs, the zonal density gradient decreases away from the boundary. This results in a decrease in the vertical shear in meridional velocity as one moves away from the wall (see Fig. 2.10)

The structure of the dense plume is somewhat reminiscent of the observations of turbidity currents in submarine channels, which have an asymmetry in the heights of their levee banks (Komar, 1969; Cossu et al, 2010), or of the classic "cylinder

collapse experiment” (Marshall and Plumb, 2008). The densest water gets stacked against the wall which creates a region of high pressure against the wall. The pressure gradient is balanced by the Coriolis force, which generates a southward velocity and the fluid moves down into the ice shelf cavity.

The results described in (Cossu et al, 2010) emphasize the importance of Ekman layer dynamics in determining the transport of the gravity plumes in a turbidity current. Their experiments did not have an upper boundary. Never-the-less, their results suggest that the plumes found in our experiment and under an ice shelf, are likely to be affected by the upper boundary, which creates an upper Ekman layer.

In Fig. 2.12 the time varying volume flux through the dense plume is plotted. The volume flux is defined as:

$$\hat{V}(y) = - \int_A v(x, y, z) dx dz \quad (2.7)$$

A is the cross-sectional area of the plume. The cross sectional area of the plume is the area between the western wall and the plume edge. We define the edge of the dense plume using the following procedure: At each height we find the first 3 successive points closest to the western boundary which all have a meridional velocity $v > 0$. We define the first of these three points to be the edge of the plume and define our plume to be all points to the west of the plume edge. We allow for 3 points to make our calculation less susceptible to individual erroneous points.

Figures 2.10 and 2.11 show that the structure and size of the dense plume is

affected by changes in the geometry of the ice shelf cavity and changes in the amount of dense and fresh water injected into the system. Figure 2.12 shows that the amount of water fluxed into the cavity through the dense plume is also sensitive to changes in these parameters.

The Thickness Investigation is shown in the top row of Figures 2.10, 2.11 and 2.12. These figures show that when the ice shelf cavity is thick there is a greater flux through the dense plume than for thinner ice shelf cavities. Southward moving water approaching the ice front is able to enter the ice shelf cavity more easily when the cavity thickness at the ice front is wider while for narrower cavity thicknesses some of this water is blocked by the ice shelf, and is forced to remain outside of the ice shelf cavity on the continental shelf. One could imagine that in the limiting case of a very wide cavity entrance, the flow entering the cavity would be unimpeded at the ice front, while for extremely narrow cavity thickness at the ice front, no water would be able to move into the cavity, and all water would recirculate on the continental shelf.

The Gradient Investigation, in the second row, shows that the Pinch Run has a larger flux through the dense plume than the Stretch Run, while the Control Run has an intermediate amount. This is explained by noting that the thickness of ice shelf cavity at the ice front in The Stretch is smaller than the thickness of the ice shelf cavity at the ice front in The Pinch with the Control Run having an intermediate cavity thickness at the ice front. This result is consistent with Thickness Investigation.

The Buoyancy Investigation, in the third row, shows that if more dense water is injected into the system, it results in a larger plume flowing into the cavity (this can be seen in the velocity data in Fig. 2.10 and Fig. 2.12).

2.3.4 Plume variability

Most of the above analysis has focused on the time mean fields. However, when we look at the time dependent data, we see that the circulation inside the cavity and the flow through the plumes are in fact highly variable. In this section we focus on the time dependence of the flow in the dense plume. Movies showing the time evolution vorticity, kinetic energy and concentration fields throughout the cavity can be viewed online at <http://efdl.cims.nyu.edu/publications/refereed.html>.

Figure 2.12 shows a time series of the volume flux of the dense plume (defined above) at $y = -54$ (blue) and at $y=-110$ (green), which are both latitudes inside of the ice shelf cavity. A horizontal red line is plotted indicating the flux of water at the dense source in the experiment. The flux at the two latitudes vary together since the time scale of the oscillations is much longer than the time taken for fluid to move down the plume from the northern latitude to the southern latitude.

The most striking feature in Fig. 2.12 is that the various experimental runs have different volume fluxes through the dense plume, and that these volume fluxes are highly variable. The variabilities in the various experimental runs have different amplitudes and different periods depending on the geometry of the ice shelves and buoyancy sources used. As discussed in the previous section, the amplitude of

volume flux through the plume is proportional to the thickness of the opening of the ice shelf cavity at the ice front.

In Thickness Investigation (top row of Fig. 2.12), we see that the plume is more variable for a thick ice shelf cavity than for the thin cavity. For the thick ice shelf, the amplitude of the variations is bigger, and the period of the variations is longer. The Control Run has an intermediate amount of variability. In Gradient Investigation (second row in Fig. 2.12), we see that period of the oscillations in the plume in the Stretch Run is larger than in the Pinch Run, with the Control Run having an intermediate period. The amplitude of the oscillations also appears to be larger in the Stretch Run. This is especially apparent when the time series' are normalized. In the Buoyancy Investigation (bottom row of Fig. 2.12), we see that amplitude and period of the oscillations is larger and longer for the Dense Run than for the Fresh Run with the Control Run being intermediate.

The variability of the plume seems to indicate how much the circulation inside the ice shelf cavity is influenced by the variability outside of the cavity. The experimental runs with strong dynamic barrier at the ice front, seem to restrict movement inside the ice shelf cavity, and to limit variability inside the plume. The runs which have a weaker dynamic barrier at the ice front have more motion inside the ice shelf cavity, and have a more variable dense plume.

Looking carefully at the time varying data, we see that the dense water does not move smoothly from the source to the plume, but instead arrives in pulses. These pulses cause the oscillations in the flow rate seen in Fig. 2.12. The fluid is

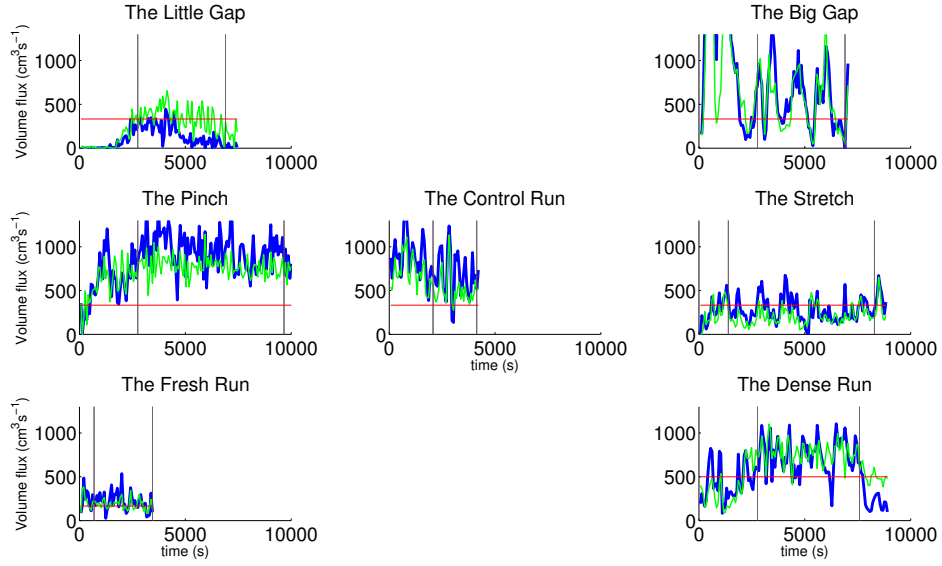


Figure 2.12: Time series of the volume flux of the dense plume at $y = -54\text{cm}$ (blue) and at $y=-110$ (green), which are both latitudes inside of the ice shelf cavity. The horizontal axis shows time in seconds. A horizontal red line is plotted indicating the dense source flux rate in the experiment. The dashed vertical lines indicate the times between the time-averages were taken in the previous sections.

injected smoothly into the domain by the dense source (i.e. without pulses), which implies that some other mechanism is causing the flow to be unsteady. The most likely candidates are baroclinic instability of the gyre on the continental shelf and that eddies are created at the dense source when the dense fluid was released into the domain.

2.4 Discussion

In the previous sections we saw evidence of the dynamic significance of the ice front in largely blocking water from entering and exiting the ice shelf cavity, and

that this blocking effect was significantly altered by changing the ice geometry and buoyancy fluxes. We discuss these in turn:

The blocking effect of the ice shelf front has been noted by other authors using numerical models (Determan and Gerdes, 1994; Grosfeld et al, 1997). Grosfeld (1997) Grosfeld et al (1997) used a three dimensional numerical model and observed that the flow was dominated by the barotropic mode, which steers the flow along the ice front rather than into the ice shelf cavity. The presence of the ice shelf imposes a change in water column thickness which presents a barrier for the barotropic flow. The barotropic flow tends to move along $\frac{f}{H}$ contours which run parallel to the shelf. For this reason, the zonal jet outside the ice shelf cavity runs along the ice front but does not enter.

However, while the results presented above do demonstrate the blocking effect of the ice shelf, they also demonstrate that this blocking effect is not as severe as previously suggested (Determan and Gerdes, 1994; Grosfeld et al, 1997). Figure 2.7 show that although the jet runs along the ice front, it does leak into the ice shelf cavity to some extent. There is a significant vertical shear in the velocity of the jet along the ice front. This indicates that the jet is not solely dominated by the barotropic mode. The leaking of the jet into the cavity may be a result of baroclinic instability. Furthermore, Fig. 2.5 shows there is some flux into and out of the ice shelf cavity away from the boundary currents, despite the dynamic barrier imposed by the ice shelf.

Furthermore, water is able to flux into and out of the cavity relatively freely

through the dense and fresh plumes. This is because in the dense and fresh plumes, the stratification decouples the water column and the plumes are able to enter/exit the ice shelf cavity more easily (Holland and Jenkins, 2001).

The results from Thickness Investigation, Gradient Investigation and Buoyancy Investigation indicate that the blocking effect of the ice shelf front, the amount of movement inside the ice shelf cavity, and the flux of water through the density plumes, are strongly affected by the geometry of the ice shelf cavity, and the amount of dense and fresh water injected into the system. Figure 2.13 is a schematic which summarizes the findings discussed above. In Fig. 2.13, the dense plume, the circulation on the continental shelf and the circulation inside the ice shelf cavity are represented using arrows. The size of the arrows is an indication of the strength of the plumes and circulations observed in the experiment (not to scale). We use Figure 2.13 to summarize our results in terms of the non-dimensional parameters described in section 2.2.2.

The results in Thickness Investigation show that making the ice shelf cavity narrower (decreasing G_t), decreases the size of the dense plume, decreases the circulation inside the ice shelf cavity, and increases the size of the gyre on the continental shelf outside of the ice shelf cavity. For larger values of G_t , the flux through the dense plume is increased, there is increased circulation inside the ice shelf cavity and there is a weaker gyre on the continental shelf. We conclude that the dynamic barrier at the ice front is strongest for small values of G_t . Small values of G_t decrease the connection between the water outside and inside the ice shelf cavity.

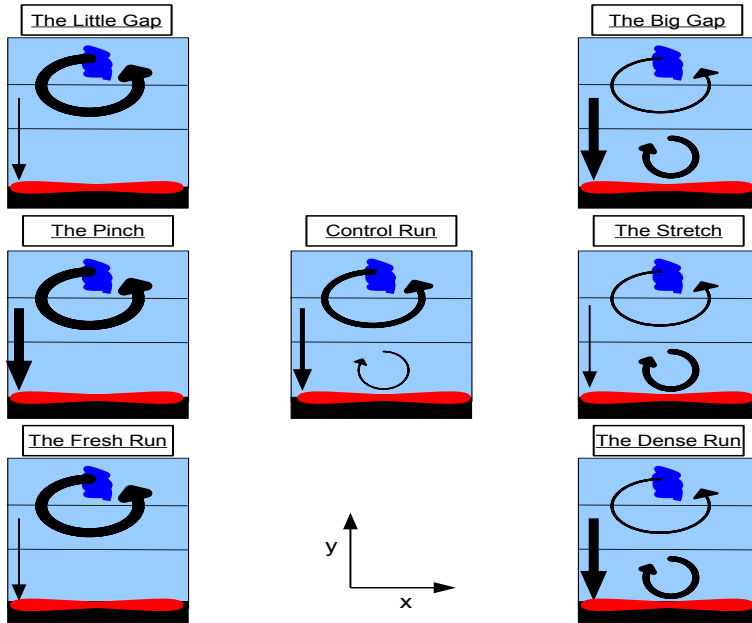


Figure 2.13: A schematic summarizing the results from the three investigations. The size of the dense plume, the strength of the circulation inside the ice shelf cavity, and the strength of the circulation outside the ice shelf cavity are shown by the size of the arrows in each of the experimental runs (not to scale).

The Gradient Investigation shows the effect of changing the slope of the ice shelf. In this investigation we see the competing effects of local and global geometry conditions. Changes in G_t affect the ice front locally, while changes in G_s change the geometry on a larger scale. These competing effects allow the Stretch Run to have a small dense plume and yet also to have a lot of activity inside the ice shelf cavity and less activity outside the ice shelf cavity. The Pinch Run has a strong plume, and almost no motion inside the ice shelf cavity away from the boundary currents.

The strength of the flux through the dense plume is controlled locally by the

parameter G_t . Decreased values of G_t result in a decreased flux through the dense plume. The Stretch Run, for example, has a narrower cavity thickness at the ice front, which means that a larger portion of the water approaching the ice front will be unable to enter the ice shelf cavity, and will have to remain on the continental shelf. The Pinch Run has a wider cavity thickness at the ice front, which means that less of the water approaching the ice shelf cavity will be blocked from entering. The trajectory of the water approaching the ice shelf cavity is strongly influenced by the cavity thickness at the ice front, and hence by the value of G_t . This result is the same as the result observed in the Thickness Investigation.

However, the results of the Gradient Investigation also indicate that the strength of the circulation inside the ice shelf cavity increases with decreasing values of G_s , despite the fact that the values of G_t are decreasing too. This is the opposite of the result observed in the Thickness Investigation, where decreasing values of G_t resulted in decreasing circulation inside the ice shelf cavity. This shows that the circulation inside the ice shelf cavity is controlled more strongly by the gradient of the ice cavity thickness on the large scale, than the local thickness of the cavity at the ice front.

The movement inside the ice shelf cavity and the flux through the dense plume are both indications of the strength of the ice shelf as a dynamic barrier. The Gradient Investigation shows that the amount of motion inside the ice shelf cavity away from the plume, the strength of the circulation outside the ice shelf cavity and the blocking effect of the ice front away from the boundary currents, are controlled somewhat separately from the mechanism controlling the flux of water into

the cavity through the dense plume.

The results from Buoyancy Investigation are much like the results in Thickness Investigation. For larger values of G_b , the dense plume is large, there is a lot of motion inside the ice shelf cavity, and there is not a lot of circulation on the continental shelf. For smaller values of G_b , the dense plume is small and there is much less communication between the water inside and outside the cavity. The Fresh Run has a strong circulation on the continental shelf, while there is very little motion inside the ice shelf cavity. We conclude that increasing the flux of dense water at the dense source (increasing G_b) has the effect of decreasing the dynamical barrier at the ice front which results in a stronger connection between the motion inside the ice shelf cavity and the motion on the continental shelf. Decreasing G_b results in a strengthening of the dynamical barrier at the ice front, and decreases the connection between the circulation inside of the ice shelf cavity and the circulation on the continental shelf.

2.5 Conclusion

A laboratory experiment has been set up to simulate the density-driven currents under ice shelves. The density current were forced by the input of dense water on the continental shelf and fresh water at the grounding line. The central question asked was how water of different densities is able to enter and exit the ice shelf cavity and whether its ability to enter the ice shelf cavity is affected by the

geometry of the ice shelf, and the strength of the dense and fresh water sources. This question has important scientific significance since the flux of dense water into the ice shelf cavity ultimately impacts the melt rates of the ice shelves.

From the results presented above, we draw three conclusions. Firstly, the results show that the movement in and out of the ice shelf cavity is largely restricted away from the boundary currents. In this sense the ice shelf front acts as a dynamical barrier restricting the connection between the water inside the ice shelf cavity and the water outside the ice shelf cavity. The dynamic barrier imposed by the ice front was observed to be present for various ice shelf geometries. However, the dynamical barrier was not as strong as previously argued (Determan and Gerdes, 1994; Grosfeld et al, 1997), and some water was able to pass through the ice front away from the boundary currents.

Our second finding was that fluid was able to enter and exit the ice shelf cavity very easily through the dense and fresh plumes running along the boundaries of the domain. These boundary currents take on a triangular shape with density contours lying parallel to velocity contours. The boundary currents transport water in and out of the ice shelf cavity very efficiently. This suggests that real world ice shelf cavity boundary currents are very efficient at transporting warm, salty water into the ice shelf cavity, and that warm, salty water arriving on the continental shelf will likely be fluxed into the cavity despite the dynamic barrier imposed at the ice shelf front.

The third finding is that changes to the ice shelf geometry and changes to the

source strength of the dense and fresh water sources, was shown to have a significant effect on the time mean circulation under the ice shelf. The thickness of the ice shelf cavity at the ice front was shown to be an important parameter in setting the volume flux through the dense plume. The thickness of the ice shelf cavity, and the slope of the ice shelf were shown to have a strong influence on the strength of the circulation inside the ice shelf cavity. Ice shelves whose thickness decreases as one moves from the grounding line towards the ice front, were shown to have more motion inside the ice shelf cavity. Furthermore, it was shown that increasing the strength of the dense source resulted in an increase in the amount of motion inside the ice shelf cavity, and a weakening of the dynamical barrier imposed by the ice front.

The experiments described here are a first attempt at using laboratory experiments to mimic ice shelf circulation. We were able to simulate the circulation under the ice shelf and generate a flow with the same broad features as the circulation surmised under real-world ice shelves using limited data. The experimental results presented above show that the circulation inside the ice shelf cavity, and the effectiveness of the ice front as a dynamical barrier, are both sensitive to the changes in the buoyancy sources and the ice shelf geometry.

Chapter 3

Instability and mixing of ocean jets along an idealized Antarctic continental shelf break

3.1 Introduction

The exchange of warm water across the Antarctic continental shelf margin has led to a sustained presence of Circumpolar Deep Water (CDW) on the continental shelf in the Amundsen and Bellingshausen Seas (Jenkins et al, 1997; Walker et al, 2008; Moffat et al, 2008; Jacobs et al, 2011). This ocean warming has caused increased melt rates of the adjacent ice shelves, and accelerations in the ice streams which flow into those ice shelves (Rignot et al, 2002; Jacobs et al, 2011; Pritchard et al, 2012).

It is still unclear what controls the dynamics of the exchange of CDW across

the continental shelf break. Ocean observations indicate that the heat exchange could be driven by baroclinic eddies, which cross the shelf break (Moffat et al, 2008). Others have argued that the amount of cross-shelf exchange is modulated by large scale atmospheric circulation patterns which control the local wind directions over the continental shelf break (Thoma et al, 2008; Dinniman et al, 2011). The exchange process is strongly influenced by the bottom topography and CDW intrusions tend to occur through troughs in the sea floor (Moffat et al, 2008; Wahlin et al, 2010). Regional modeling studies with realistic bathymetry indicate that the CDW exchange is influenced by the curvature of the continental shelf (Dinniman and Klinck, 2004) and the amount of vertical mixing of the intruding waters with the colder surface waters (Dinniman et al, 2011).

Most recent numerical studies have emphasized the interaction between the highly turbulent, strongly zonal Antarctic Circumpolar Current (ACC), and the sloping bottom topography, in determining the exchange across the shelf break (Zhang et al, 2011; Stewart and Thompson, 2013; St-Laurent et al, 2013). The proximity of the West Antarctic coastline to the southern edge of the ACC has been put forward as a reason for this being the primary location of cross-shelf exchange. Using a simplified 2-layer primitive equation model, Zhang et al (2011) showed the emergence of the zonal jet which forms over the continental shelf break as a result of interactions between the ACC and the sloping bottom topography. The presence of a shelf break jet, would likely affect the cross shelf exchange dynamics.

Topographically steered ocean jets are often associated with strong fronts in density, salinity and temperature across the continental shelf break (Beardsley and

Flagg, 1976; Jacobs, 1991; Huthnance, 1995). It has been hypothesized that a strong jet can act as a transport barrier blocking the flux of water across the jet center (Samelson, 1992; Dritschel and McIntyre, 2008). This has been observed in the Southern Ocean, where narrow zonal jets separate regions of differing density (Orsi et al, 1995). The strength and variability of these jets is associated with the strength of meridional transport (Sokolov et al, 2007; Thompson and Richards, 2011).

On the other hand, the large amount of potential energy stored in a strong baroclinic jet, can give rise to large instability events, which can cause enhanced mixing across the jet center (Pavan and Held, 1996). This is especially true over steep topography which can support jets with large amounts of shear. Growth rates of barotropic (Poulin and Flierl, 2005) and baroclinic (Changheng et al, 2013) instabilities are strongly controlled by the gradient and orientation (Benilov, 2001) of the bottom topography. Furthermore, the meridional transport across the jets is related to the jet meandering, which is in turn controlled by the bottom topography. Meridional transport can be inhibited or enhanced by changing the length scale of the meridionally varying the bottom topography (Thompson, 2010).

In this paper we focus on the mesoscale dynamics of ocean jets which form over steep topography at the continental shelf margin, and discuss the role which jet stability plays in setting the cross-shelf exchange. We hypothesize that the time variability of these shelf break jets affects the exchange of water across the shelf break. The relationship between cross-shelf exchange and the instability and meandering of the shelf break jets is examined in a series of numerical experiments.

Section 2 gives details on the model and experimental setup. Section 3 presents the model results for a wide range of shelf break topographies and wind forcings. Section 4 focuses on shelves of intermediate width which display a low-frequency intermittent variability. Section 5 discusses meridional jet drifting. Section 6 contains some concluding remarks.

3.2 Numerical model and experimental design

3.2.1 Quasi-Geostrophic Model

Numerical experiments are performed using a two layer quasi-geostrophic model. The governing model equations are

$$\frac{\partial q_1}{\partial t} + J(\psi_1, q_1) = -A_h \nabla^6 \psi_1 + \frac{\mathbf{k} \cdot \nabla \times \tau}{\rho_1 H_1} \quad (3.1)$$

$$\frac{\partial q_2}{\partial t} + J(\psi_2, q_2) = -A_h \nabla^6 \psi_2 - r \nabla^2 \psi_2 \quad (3.2)$$

where

$$q_1 = \nabla^2 \psi_1 + \beta y + F_1(\psi_2 - \psi_1) - F_0 \psi_1 \quad (3.3)$$

$$q_2 = \nabla^2 \psi_2 + \beta y + F_2(\psi_1 - \psi_2) + \frac{f_0 \eta_b}{H_2} \quad (3.4)$$

and $F_0 = \frac{f_0^2}{g H_1}$, $F_1 = \frac{f_0^2}{g' H_1}$ and $F_2 = \frac{f_0^2}{g' H_2}$. The mean Coriolis parameter is f_0 , β is the linear slope in the planetary rotation, g is the gravitational acceleration, $g' = \frac{g \Delta \rho}{\rho}$ is the reduced gravity. The biharmonic viscosity coefficient is A_h and r is the bottom drag coefficient. The layer thicknesses are H_1 and H_2 , and η_b is the

bottom topography. Variables q_k and ψ_k are the potential vorticity and the stream function in the k^{th} layer, and $J(\cdot)$ is the Jacobian operator.

Momentum and mass conservation equations are needed to close the system (McWilliams , 1977)

$$\oint_0^{Lx} [D_t[u_{0k}] - f_0 v_{1k} - \beta y v_{0k} = \\ -g \partial_x \eta_1 - \delta_{N,k} r u_{0k} - A_H \nabla^4 u_{0k} + \delta_{1,k} \frac{\tau}{\rho_1 H_1}] dx \quad (3.5)$$

$$\frac{\partial}{\partial t} (\iint_D \psi_k dxdy) = 0 \quad (3.6)$$

The integral in equation (3.6) is over the entire domain D . $u_0 = -\frac{\partial \psi}{\partial y}$ and $v_0 = \frac{\partial \psi}{\partial x}$ are the first order horizontal velocities, and $\eta_k = \frac{f_0 \psi_k}{g_k}$ is the interface height.

One further equation is needed to isolate the ageostrophic velocity, v_1 , used in the momentum conservation:

$$\oint_0^{Lx} [(H_k v_{1k}) - v_{0k}(\eta_k - \eta_{k-1})] dx = -\frac{d}{dt} \left[\iint_A [\eta_k - \eta_{k-1}] dxdy \right] \quad (3.7)$$

We use periodic boundary conditions at the boundaries in the east and west of the domain. No normal flow and free slip conditions are applied at the solid walls in the north and the south of the domain ($\psi = \nabla^2 \psi = \nabla^4 \psi = 0$). The model uses a third order Adams-Bashforth time stepping method and a multi-grid method is used for the elliptical inversion. Model parameters are given in Table 1. Further details of the model numerics are described in Nadeau and Straub (2011).

Parameter	Symbol	Value
Typical Rossby deformation radius	L_d	11.5
Horizontal resolution	$\Delta x = \Delta y$	3.125km
Typical time step	Δt	1000 seconds
Typical spinup time	-	300 years
Typical averaging time	-	200 years
Width of channel	L_x	1200km
Length of channel	L_y	1900km
Thickness of upper layer	H_1	1000m
Thickness of lower layer	H_2	3000m
Gravitational acceleration	g	9.8ms^{-2}
Typical reduced gravity	g'	0.03ms^{-2}
Coriolis parameter	f_0	$-1.3 \times 10^{-4}\text{s}^{-1}$
Beta parameter	β	$1.5 \times 10^{-11}\text{s}^{-1}\text{m}^{-1}$
Reference density	ρ_1	1027 kg m^{-3}
Drag parameter	r	1.5×10^{-7}
Biharmonic dissipation coef	A_h	1×10^8
Laplacian dissipation coef	κ_T	1×10^2
Height of topography	h_0	2500m

Table 3.1: Model parameters

3.2.2 Experimental Design

The zonally symmetric bottom topography is described by the equation

$$h_b(y) = \frac{h_0}{2}(1 + \tanh((y_0 - y)/W)) \quad (3.8)$$

Here h_0 is the shelf height, y_0 is the position of the shelf break, and W is a parameter which controls the shelf width. We fix $y_0 = 300\text{km}$ and $h_0 = 2500\text{m}$ in most of the experiments. The parameter W controls both the width and the slope

of the shelf break. The layer thicknesses are chosen with heights $H_1 = 1000\text{m}$ and $H_2 = 3000\text{m}$. The reduced gravity is chosen to make the deformation radius $L_D = 11.5\text{km}$. The grid scale used was $\Delta x = 3.125\text{km}$, so we expect to be in an eddy resolving state. The smallest shelf width parameter, W , used in our experiments is $W=10\text{km}$. Since the width of the shelf break region is $\sim 2W$, we have a minimum of 8 meridional grid points over the shelf break region.

Our flow is forced by wind stress described by the equation

$$\tau(y) = \tau_0 \sin^2\left(\frac{\pi y}{L_y}\right) \quad (3.9)$$

Some experiments were forced using an imposed background shear (see Section 5a). The experimental setup allows for the highly turbulent current in the open ocean to interact with the continental shelf break topography in the south of the domain.

3.2.3 Tracer diagnostics

Passive tracers are used to quantify the mixing across the shelf break. The tracer is advected by the flow according to the equation

$$\frac{\partial C}{\partial t} + J(\psi_i, C) = \kappa_T \nabla^2 C \quad (3.10)$$

We used $\kappa_T = 10^2$, but the results were found not to be sensitive to this choice of κ_T since the flow of the tracer is dominated by advection.

The value of the tracer was fixed at $C=1$ on the southern boundary, and $C = 0$ for $y \geq 600\text{km}$. This Dirichlet boundary condition allowed tracer to flux into the domain in the south and out of the domain at $y = 600\text{km}$. The tracer was initialized to vary linearly from one to zero over the interval $[0, 600\text{km}]$. The total amount of tracer to flux through the latitude $y = 600\text{km}$ was then used as a measure of the amount of cross-shelf mixing.

Another tracer diagnostic quantified mixing by considering how the distribution of tracer changed over a fixed amount of time. However, the amount of mixing caused by an instability event, calculated using this diagnostic, was found to be dependent on how recently the tracer had been re-initialized. While this diagnostic is effective in measuring the mean amount of mixing over a long period of time, it is not appropriate for measuring the size of isolated instability events.

3.3 Effect of topography and wind on cross shelf exchange

3.3.1 Phenomenology

In this section, we consider how the flow over the continental shelf break responds to changes in the shelf break width, W , and wind forcing, τ_0 .

Figure 3.1 shows Hovmöller diagrams of the zonally-averaged zonal velocity for 200 year simulations using various values of W and τ_0 . Strong jets forms over the

shelf break region in many of the simulations. The strength and stability of these shelf break jets are influenced by the shelf break width. Shelf break topographies with steeper slopes give rise to stronger shelf break jets, provided the shelf width is above a certain threshold. The period between instability events decreases with wind forcing and shelf width, W .

The simulations shown in Fig. 3.1 display a wide variety of behaviors indicating that they span different parameter regimes. Experiments can be classified in terms of the number of jets that form over the shelf break. For $W < 25\text{km}$, no jet forms over the shelf break. For $25\text{km} < W < 100\text{km}$, one jet forms over the shelf break. This jet remains for a number of years before becoming unstable and drifting away from the shelf break. Instability events occur intermittently and with low frequency. Finally, for $W > 100\text{km}$, multiple jets form over the shelf break. In this parameter regime, the shelf break jet does not remain stable at anytime, and instead constantly drift northwards.

The parameter regime with very narrow shelf breaks ($W < 25\text{km}$) is of limited interest as the shelf break slopes are much steeper than those found in the real world. The multiple jet regime has been studied extensively (Rhines, 1975; Farrell and Ioannou, 2003; Thompson, 2010; Srinivasan and Young, 2012). Here we focus on the intermediate width regime where just one jet forms. Since the instabilities of the shelf break jets affect the cross-shelf mixing, we begin by discussing what sets the strength and stability of these jets. We then compare this to the amount of mixing across the shelf break.

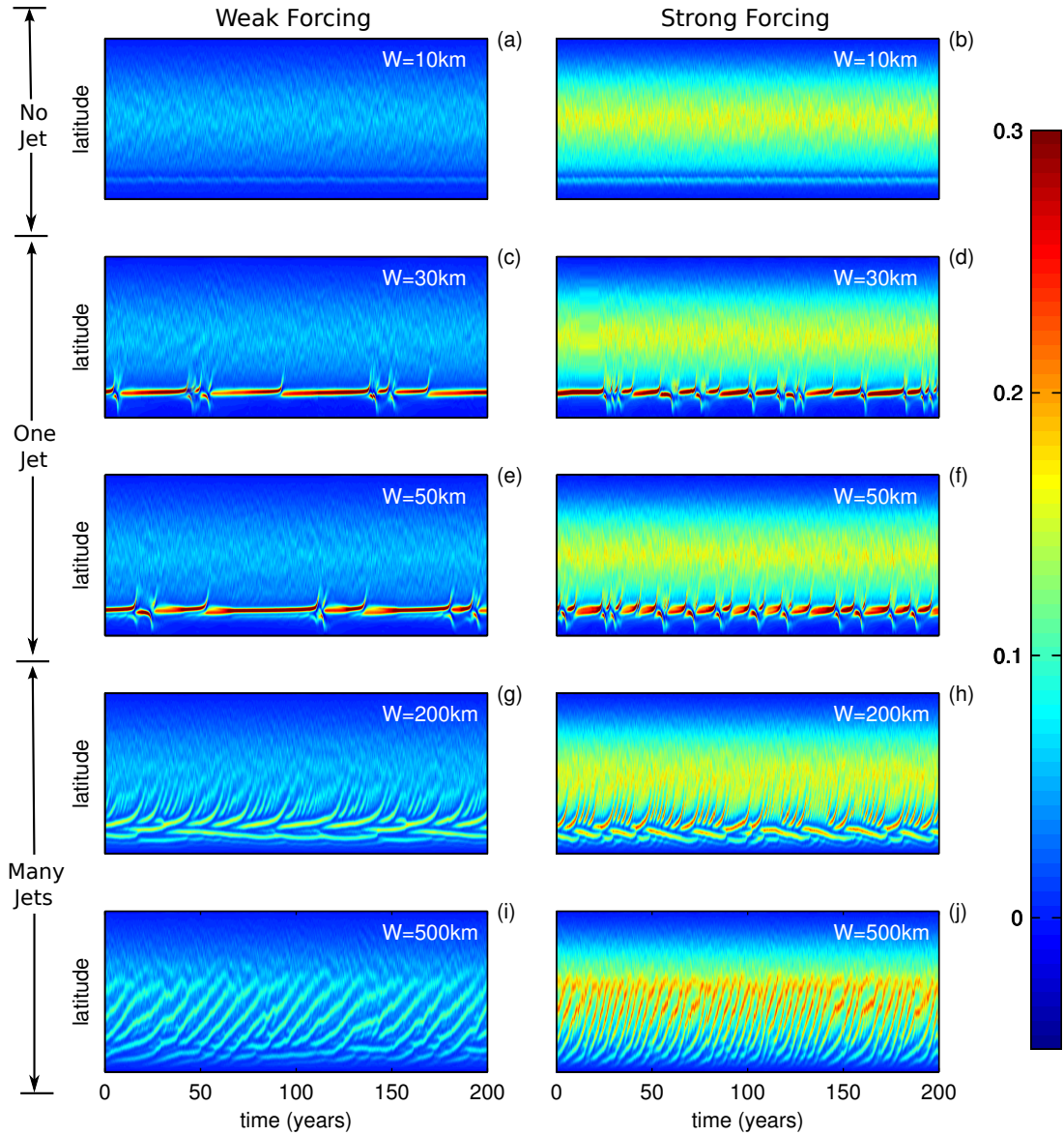


Figure 3.1: Hovmöller diagram of the upper-layer zonally-averaged zonal velocity are shown for different wind forcings and different shelf widths. Wind forcings $\tau = 0.04 \frac{N}{m^2}$ and $\tau = 0.12 \frac{N}{m^2}$ are shown in the left and right columns, respectively. Shelf widths $W=10\text{km}$, 30km , 50km , 200km , and 500km are shown from top to bottom.

3.3.2 The stabilizing effect of topography

The buildup of vertical shear in the zonal momentum over the shelf break is limited by the onset of baroclinic instability. Since the flow has a positive vertical shear, the critical instability condition (Pedlosky, 1979) is given by

$$q_{2y}^- = -\bar{u}_{2yy} - F_2(\bar{u}_1 - \bar{u}_2) + \beta_T = 0 \quad (3.11)$$

Here $\beta_T = \beta + \frac{f_0(\eta_b)_y}{H_2}$ is the effective topographic beta (Sinha and Richards, 1999; Thompson, 2010). Defining $C = (u_1 - u_2) + \frac{1}{F_2}u_{2yy}$, the instability condition becomes

$$C = \frac{1}{F_2}\beta_T \quad (3.12)$$

Figure 3.2a shows the maximum value of C obtained in our simulations for different shelf widths and wind forcings. The magnitude of C is dominated by the shear, which is maximum in the center of the jet. Since $\frac{1}{F_2}u_{2yy} < 0$ in the center of the jet, $\frac{1}{F_2}u_{2yy}$ has the effect of stabilizing the jet. The dashed line in Figure 3.2a shows the maximum value of $\frac{\beta_T}{F_2}$, which is given by $\max(\frac{1}{F_2}\beta_T) = \frac{1}{F_2}(\beta + |(\frac{f_0}{H_2}\frac{h_0}{2W})|)$. The absolute value signs are included to emphasize that the topography stabilizes the jet and has the same effect as increasing β .

Figure 3.2a shows that for $W < 25\text{km}$ the flow is always sub-critical ($C < \frac{1}{F_2}\beta_T$). For $25\text{km} < W < 100\text{km}$, the maximum values of C are close to criticality ($C \sim \frac{1}{F_2}\beta_T$). For $W > 100\text{km}$, we find that $C > \frac{1}{F_2}\beta_T$ and the flow is super-critical. In the critical regime, the maximum value of C is independent of the wind forcing.

Having identified these three regimes, a natural question is what sets the length

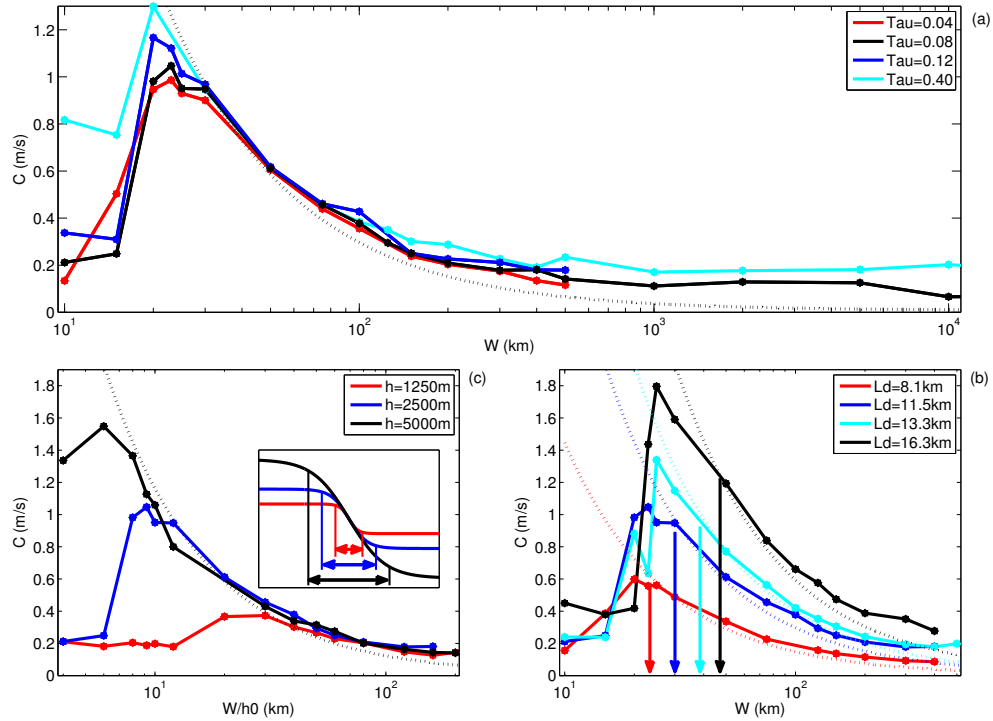


Figure 3.2: Panel (a) shows the maximum value of $C = (u_1 - u_2) + \frac{1}{F_2} u_{2yy}$ recorded in the domain during 200 year simulations for different shelf widths, W . The different colors indicate simulations using different wind speeds. Panel (b) shows the maximum value of C recorded during 200 year simulations for runs using scaled geometries. In these runs the width and height of the continental shelf was doubled (black) and halved (red). The x-axis in these plots is W/h_0 . The inset figure in panel (b) shows an example of the topography used in this experiment. The width of the shelf break is changed without changing the maximum shelf break slope. Experiments in panel (a) and (b) use deformation radius $L_d = 11.5\text{km}$. Panel (c) shows the maximum value of C for different values of W for runs using $\tau = 0.08 \frac{\text{N}}{\text{m}^2}$. Simulations were run with four different deformation radii: $L_d = 8.1\text{km}$, 11.5km , 13.3km and 16.3km , which are shown by the different color curves. The effective topographic beta, β_T , is shown by dashed lines in each panel and indicates the necessary condition for baroclinic instability.

scales which separate these three regions of parameter space? In the following we run some numerical experiments to answer this question. We then return to the question of how this jet behavior affects the cross shelf mixing.

3.3.2.1 From sub-critical to critical

As the shelf break width decreases below the eddy scale, $L_e \sim 4L_d$, we see a dramatic reduction in shear which builds up in the jet (Fig. 3.2a). This suggests that the boundary between the sub-critical and critical regions may be set by the eddy scale. Here we investigate.

Recall that changing the parameter W has the effect of altering both the slope and the width of the continental shelf break. We perform numerical experiments to decouple these two effects in order to determine what sets the upper bound of the sub-critical region. In the first set of experiments, the slope is held constant while the width of the shelf break is changed. The second set of experiments varies the deformation radius.

The first set of experiment is performed using a fixed radius of deformation, $L_D = 11.5\text{km}$, and fixed wind stress, $\tau_0 = 0.08 \frac{\text{N}}{\text{m}^2}$. The width and height of the shelf break are both doubled (and also halved), so that the average slope of the shelf break remains constant. An example of the shelf break topographies used in this experiment is shown in the inset panel in Fig 3.2b. The maximum value of C is plotted in Fig. 3.2b. The x-axis has been divided by h_0 , so that it varies like $\frac{1}{s}$, where s is the slope. The instability threshold, $\frac{1}{F_2} \beta_T$, is plotted using

a dashed line, and is the same for the three sets of simulations. The flow becomes sub-critical for different values of $\frac{W}{h_0}$ for simulations using different values of h_0 . In particular, the boundary between the sub-critical and critical regime occurs at $W \sim 25\text{km}$, for all three values of h_0 despite the fact that $W=25\text{km}$ corresponds to different shelf break slopes in each of the three simulations shown. We conclude that it is the actual width of the shelf break region which sets the upper bound of the sub-critical region, and not the slope of the shelf break.

In the second set of experiments, we vary the deformation radius. Figure 3.2c shows the maximum value of C recorded during 200 year simulations for various shelf break widths, W , and different deformation scales, L_d . The value of $\frac{1}{F_2} \beta_T$ is plotted using dashed lines for each of the deformations scales. In this figure we see that the upper bound of the sub-critical region increases with the deformation radius. For example, when $L_d = 16.3\text{km}$, the flow is sub-critical for $W < 50\text{km}$. When $L_d = 8.1\text{km}$, the flow is sub-critical for $W < 23\text{km}$. This result suggests that it is the eddy scale, $L_e \sim 4L_d$, which determines the border of the sub-critical and critical regions.

For simulations with shelf break regions smaller than the eddy scale, the flow is not influenced by the effect of the shelf break, and a jet does not form over the shelf break. This result suggests that large-scale ocean currents do not form jets over regions with large gradients in bottom topography if the gradients are only present over spacial scales smaller than the eddy scale.

3.3.2.2 Super-critical region

Further numerical experiments are performed to study the super-critical region. Results show that for sufficiently large values of W , the maximum amount of shear which builds up in the shelf break jet approaches a constant value, independent of W (Fig. 3.2a).

A set of simulations were performed using an unrealistically large wind forcing, $\tau_0 = 0.4$. The results show that the shear buildup in the super-critical region increases with wind forcing (Fig. 3.2a). This result agrees qualitatively with Johnson and Bryden (1999), who showed that in the super-critical regime, shear buildup increases with τ_0 . In the super-critical region, the shear buildup also increases with the deformation radius (not shown).

The boundary between the critical and super-critical regions depends on the slope of the bottom topography, rather than the actual width of the shelf (Fig. 3.2b). For simulations using $L_d = 11.5\text{km}$, the flow is super-critical for $W > 100\text{km}$, which corresponds to $\beta_T = 5.5 \times 10^{-10}\text{m}^{-1}\text{s}^{-1}$. Note that for $W = 3500\text{km}$, the effect of the bottom topography is equal to the effect of β .

The minimum value of W for which the flow is super critical, decreases with the deformation scale L_d (Fig. 3.2c). We also expect that the minimum value of W for which the flow is super critical should decrease with wind forcing. This can be partially seen in Fig. 3.2a, although this is not entirely clear.

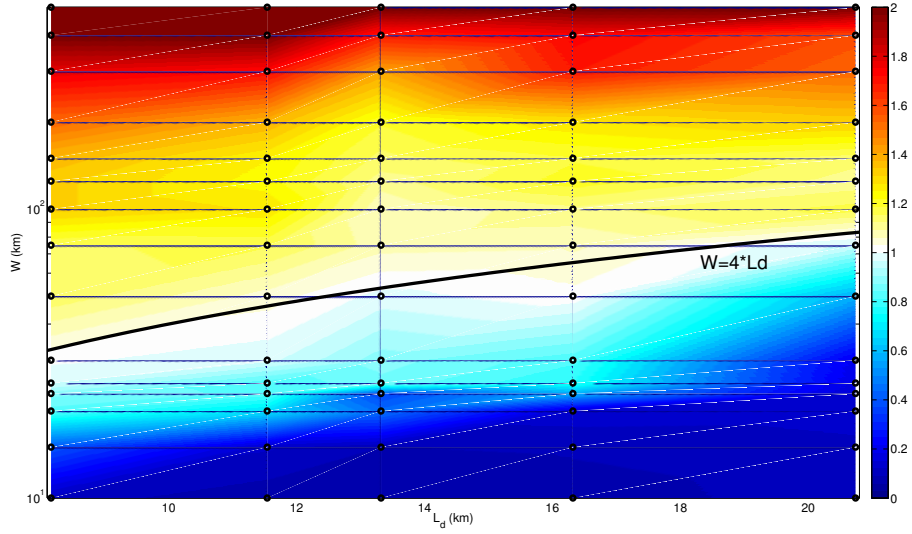


Figure 3.3: This figure shows the maximum value the criticality ratio $\frac{C}{\beta_T}$ recorded in the domain during 200 year simulations. The flow is at criticality when $\frac{C}{\beta_T} = 1$. The flow is sub-critical for $\frac{C}{\beta_T} < 1$ and super critical when $\frac{C}{\beta_T} > 1$. The criticality ratio is shown for simulations with different shelf widths and different deformation radii. The various simulations are indicated by circles. The line $W = 4L_d$ has been included for reference, and marks the width where the shelf is no longer wide enough to support a jet and the flow becomes sub-critical. For very large values of W , the flow becomes super-critical.

3.3.2.3 Summary of criticality results

Figure 3.3 shows the criticality ratio, $\frac{C}{\beta_T}$, for simulations using different shelf break widths and deformation scales. The criticality ratio gives a measure of how close to criticality the flow is during the largest instability events. The black dots in Fig. 3.3 indicate positions of each 200 year simulation. A black line is plotted showing the eddy scale $L_e = 4L_D$.

The sub-critical, critical and super-critical regimes can be clearly identified. For

shelf breaks much smaller than the eddy scale, the flow is sub-critical. Almost no shear builds up for $W \ll L_e$. At the eddy scale, the criticality ratio becomes close to one and the maximum shear buildup is strongly controlled by the slope of the bottom topography. For larger shelf widths the flow is super-critical. In this regime, the criticality ratio decreases proportionally to $\frac{1}{W}$. For a constant W , the criticality ratio is smaller for larger values of L_d . The transitions between sub-critical and critical, and critical and super-critical regimes occur for larger values of W when L_d is larger.

The results show that the evolution of the flow and shear buildup over the shelf is controlled by the parameter W . In the next section we consider how changes in the jet behavior affect the cross-shelf exchange.

3.3.3 Cross-Shelf Exchange

Figure 3.4a shows the Hovmöller diagram of the upper-layer zonally-averaged zonal velocity for the southern half of the domain for a simulation with $W=50\text{km}$ and $\tau_0 = 0.08 \frac{\text{N}}{\text{m}^2}$. A strong jet forms over the steepest part of the continental shelf break, centered at $y=300\text{km}$. This jet is destabilized and drifts northwards aperiodically. Fig. 3.4b shows the vertical shear in the zonal velocity over the continental shelf break. The shear increases steadily while the jet is stable. When the jet becomes unstable, the shear decreases sharply. The dashed line in Fig. 3.4b shows the minimum shear required for baroclinic instability as predicted by the Phillips model (Phillips, 1954; Pedlosky, 1979).

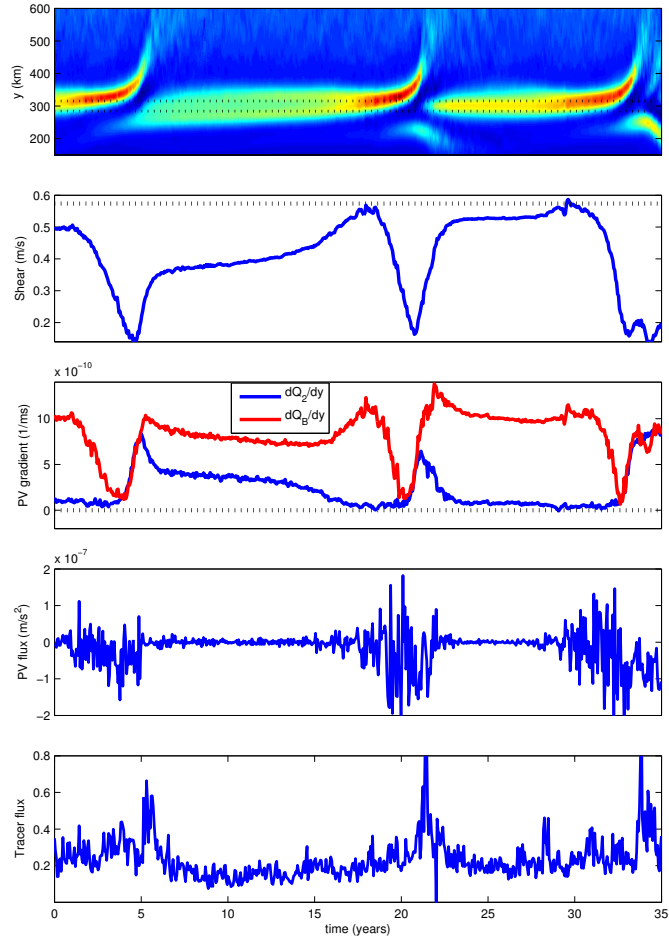


Figure 3.4: Panel (a) shows a Hovmöller diagram for the upper-layer zonally-averaged zonal velocity. A strong jet can be seen running along the shelf break. The jet becomes unstable intermittently. Panel (b) shows the time evolution of the vertical shear in the zonal velocity averaged over the shelf region. Panel (c) shows a time series of the lower-layer PV gradient and barotropic PV gradient averaged over the shelf region. Panel (d) shows the upper-layer meridional PV flux across over the shelf break region. The top four panels are averaged between $y=280\text{ km}$ and $y=320\text{ km}$ (marked by dotted lines on panel (a)). Panel (e) shows the upper-layer tracer flux across the latitude $y=600\text{ km}$. Strong mixing event can be seen by elevated tracer and PV fluxes. The timing of these mixing events coincides with the instabilities seen in panels (a) and (b). The figure shows long periods where the jet is stable and the shear builds up, followed by strong mixing events where the shear drops, and the jet drifts away from the shelf break.

Figure 3.4c shows a time series of the lower-layer PV gradient, $\frac{\partial q_2}{\partial y}$, and the barotropic PV gradient, $\frac{\partial q_B}{\partial y} = \frac{H_1 \frac{\partial q_1}{\partial y} + H_2 \frac{\partial q_2}{\partial y}}{H_1 + H_2}$, averaged over the shelf break region. During periods when the shear is building, the lower-layer PV gradient decreases. Once the lower-layer PV gradient reaches zero, the flow becomes unstable and the jet drifts away from the shelf break region. The barotropic PV gradient is greater than zero over the shelf break when the instability occurs. This suggests that the instability is baroclinic rather than barotropic. Barotropic instability can occur on the flanks of the jet where $U_{Byy} < 0$.

Two measures of the cross-shelf exchange are used to quantify the amount of mixing. Firstly, the mixing is quantified using the upper-layer meridional PV flux at $y=300\text{km}$. Since the PV is advected like a tracer, the amount of PV mixing gives us a convenient measure of the amount of mixing across the shelf break. The maximum magnitude of the meridional PV flux during an instability event can be used to quantify the size of that instability event. The meridional PV flux is not a perfect mixing metric as PV is not conserved in the domain. Secondly, we quantify the mixing using a passive tracer which advects with the flow (see Section 2c). The size of an instability event is quantified by the maximum meridional tracer flux at the latitude $y=600\text{km}$. Since both the PV and the tracer are not conserved in the domain, we do not expect exact agreement between the two methods of quantifying mixing.

Figure 3.4d shows a time series of the upper-layer meridional PV flux over the shelf break. Figure 3.4e shows the time series of the flux of tracer across the latitude $y=600\text{km}$. There is little mixing during periods where the jet is stable. The

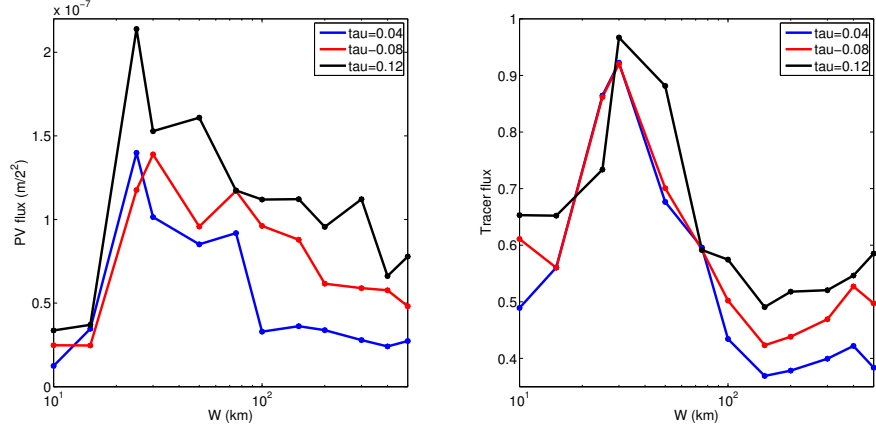


Figure 3.5: Left: the maximum upper-layer meridional flux of potential vorticity at $y=300\text{km}$ found during 200 year of simulations for different values of the shelf width parameter, W . Right: the maximum upper-layer tracer flux at latitude $y=600\text{km}$ found during 200 year simulations for different values of W . In both panels, the different colors indicate simulations using different wind speeds.

PV flux and tracer flux increase when the jet becomes unstable.

This connection between jet instability and mixing, together with the wide range of jet behavior seen in Fig. 3.1 suggests that there may be a relationship between the width of the shelf break region and the amount of cross-shelf exchange. Figure 3.5 shows the magnitude of the largest cross-shelf mixing events recorded during 200 year simulations, for various shelf break widths, W . The mixing quantified using the maximum PV fluxes and the maximum tracer fluxes are shown in Fig. 3.5a and Fig. 3.5b, respectively. Both methods show that mixing events are largest for shelf widths around $W=30\text{km}$, and decrease for larger values of W . The size of the mixing events increase with wind forcing, τ_0 . This is especially clear when $W > 100\text{km}$. For very narrow shelves, there is very little mixing.

Figure 3.5 suggests that the amount of mixing which occurs during instability events is proportional to the amount of shear in the jet (Fig. 3.2a). Greater shear buildup results in larger instability events, which cause greater amount of cross shelf mixing. In the next subsection, we argue that the jet drifting helps to create larger mixing events.

3.3.4 Connection between jet drifting and mixing

Pavan and Held (1996) showed that for a given value of β , the amount of mixing through the center of a baroclinically unstable jet increases with shear in the jet. Once the shear is large enough to cause baroclinic instability, the amount of mixing increases more rapidly for smaller values of β .

Over the continental shelf break, the large gradients in the bottom topography allow for a large buildup of shear in the jet. When the flow becomes unstable, the jets drift towards a region of lower background PV gradient. We hypothesize once a jet has drifted away from the steeper part of the shelf break, the PV gradient felt locally by the jet is reduced. Since the jet has a large shear and the local bottom slope is small, this can give rise to much enhanced mixing events.

In the critical regime, the steep bottom topography allows for the largest buildup of shear and results in the greatest amounts of cross-shelf mixing. This provides motivation to explore the dynamics of the critical regime more closely.

3.4 Intermittent critical regime

In this section, we focus on the dynamics of the intermittent critical regime. We saw in the previous section that this parameter regime displays a low frequency, intermittent jet variability, and that the size of cross-shelf mixing events are largest in this regime. We examine this regime by considering the dynamics of a simulation with $W=50\text{km}$ and $\tau_0 = 0.08$. We begin by looking at the steady state properties of the flow.

3.5 Intermittent critical regime

In this section, we focus on the dynamics of the intermittent critical regime. We saw in the previous section that this parameter regime displays a low frequency, intermittent jet variability, and that the size of cross-shelf mixing events are largest in this regime. We examine this regime by studying the dynamics of a simulation with $W=50\text{km}$ and $\tau_0 = 0.08 \frac{\text{N}}{\text{m}^2}$, which is an example of a simulation in this parameter regime. We begin by looking at the steady state properties of the flow.

3.5.1 Steady State Fields

Figure 3.6 shows time-averaged, zonally-averaged fields for a 200 year simulation (excluding spinup). A strong baroclinic jet can be seen over the shelf break (Fig. 3.6a). The jet appears over the region where the lower-layer background PV gradient, β_T , is maximal (Fig. 3.6b). The strong shear in the jet results in a large meridional PV gradient over the shelf break in the upper layer and a reduced meridional PV gradient in the lower layer (Fig. 3.6b). Interestingly, the large upper-layer PV gradient over the shelf break does not affect the time-averaged

upper-layer meridional PV flux (Fig. 3.6c). This is explained by looking at the steady state PV evolution equation. It can be shown that the evolution of the total PV on the continental shelf is given by

$$\frac{\partial}{\partial t} \iint_A q_1 dA = -\overline{v'_{g1} q'_1} - \frac{\tau^{(x)}}{\rho_1 H_1} \quad (3.13)$$

$$\frac{\partial}{\partial t} \iint_A q_2 dA = -\overline{v'_{g2} q'_2} + r\overline{u_2} \quad (3.14)$$

Here $\overline{(\)}$ is the zonal mean, and $()'$ signifies deviations from the zonal mean. The region A is defined as being all area south of a latitude y . The right hand side of the equation is evaluated on the northern boundary of the region A. We have neglected the viscous term, which does not contribute significantly to the time mean.

In steady state, the upper-layer meridional eddy PV flux is balanced by the wind forcing, $\langle -\overline{v'_{g1} q'_1} \rangle = \frac{\tau^{(x)}}{\rho_1 H_1}$, and is independent of the bottom topography (Fig. 3.6c). Here $\langle \rangle$ signifies the time mean. The lower-layer steady state balance (Fig. 3.6d) is between the drag and the lower-layer meridional eddy PV flux, $\langle -\overline{v'_{g2} q'_2} \rangle = \langle -r\overline{u_2} \rangle$. The reduced lower-layer velocity over the shelf break implies that the lower-layer time-mean meridional PV flux is lowered over the shelf break, indicating a lower-layer transport barrier.

The meridional eddy PV flux is made up of a Reynolds stress divergence term and a term due to interfacial stress or form drag.

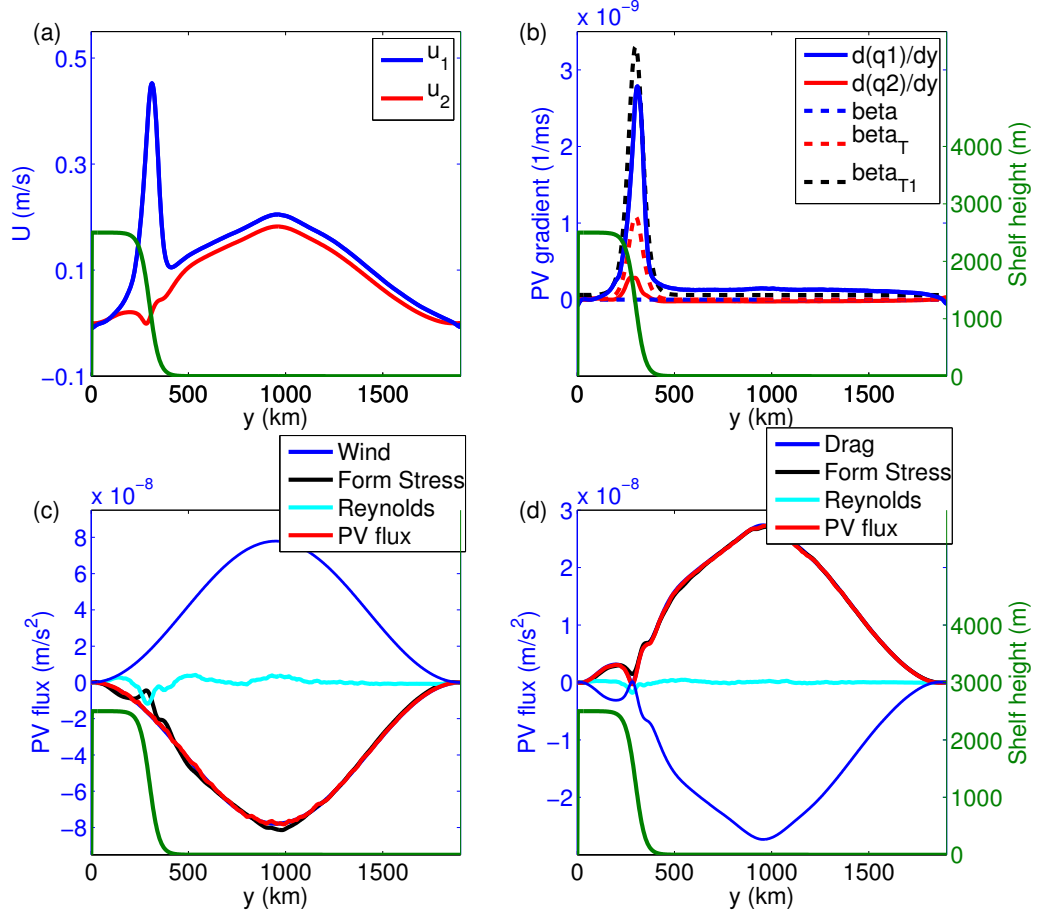


Figure 3.6: Panel (a) shows the time-averaged, zonally-averaged velocity in the upper and lower layers. Panel (b) shows the time-averaged zonally-averaged meridional PV gradient in the upper and lower layers. The dashed lines show upper-layer background PV gradient, β , and the lower-layer background PV gradient, β_T . The analytic estimate for the upper-layer mean PV gradient, β_{T1} , is also shown. In Panel (c), the red, black, cyan and blue curves show the upper-layer meridional PV flux, form stress, Reynolds stress divergence and the wind forcing, respectively. In Panel (d), the red, black, cyan and blue curves show the lower-layer meridional PV flux, form stress, Reynolds stress divergence and drag, respectively.

$$\overline{v'_{gi}q'_i} = \overline{v'_i\zeta'_{gi}} + F_i \overline{\psi'_{ix}\psi'_j} \quad (3.15)$$

The upper-layer Reynolds stress divergence over the shelf break region is negative (Fig. 3.6c), indicating a divergence of momentum fluxes out of the jet. This Reynolds stress divergence is balanced by an increased interfacial form stress in the upper layer. In the lower layer, the form stress dominates the PV flux, and the Reynolds stress divergence is much smaller.

However, these time-mean fields are somewhat misleading as they are dominated by the largely increased fluxes which occur during short periods when the jet is unstable. To get a more complete understanding of the dynamics, it is necessary to consider the time varying features of the flow. We begin by considering the spinup phase, which shows how the onset of instability helps to determine the steady state PV distribution and thus allows for a shelf break jet to form. We then consider the evolution of forces during an instability event, which give rise to the steady state fields shown in Fig. 3.6c and Fig. 3.6d.

3.5.2 Spinup

Figure 3.7a and Fig. 3.7b show the Hovmöller diagrams of upper-layer zonally-averaged zonal velocity and upper-layer zonally-averaged PV during the spinup phase, for a simulation using $\tau_0 = 0.08 \frac{N}{m^2}$ and $W=50\text{km}$.

During the spinup, no jet forms over the continental shelf break initially. After

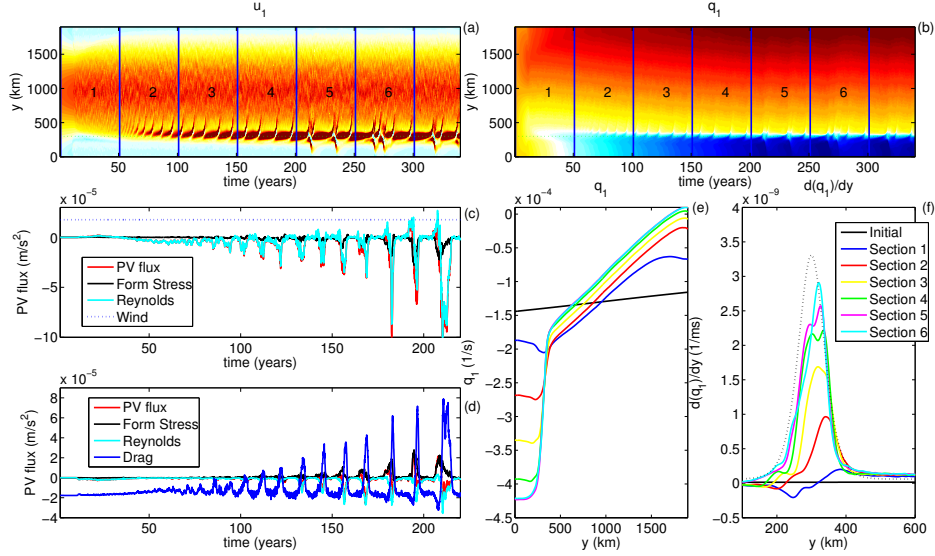


Figure 3.7: The spinup and jet formation process for $\tau = 0.08 \frac{N}{m^2}$, $W=50\text{km}$ is shown. Panel (a) shows the Hovmöller diagram of the upper-layer zonally-averaged zonal velocity. As the channel spins up, we see the formation of a zonal jet over the continental shelf break. Panel (b) shows a Hovmöller diagram of the upper-layer zonally-averaged PV field. As the flow spins up, negative PV is created on the shelf. Panel (c) and (d) show time series of the terms on right hand side of equations (3.13), (3.14), and (3.15). The terms are evaluated at $y=300\text{km}$. Panel (e) and (f) show the time-averaged upper-layer PV and upper-layer PV gradient during six different stages of the spin up process. The time averages are taken over the six time intervals shown on panel (a). The dashed line in panel (f) shows the upper-layer effective beta which is the hypothesized equilibrium for the upper-layer PV gradient.

60 years, a jet forms over the steepest part of the shelf break. This jet persists for a few years, and then becomes unstable. Figure 3.7c and Fig. 3.7d show time series of the terms on the right hand side of equations (3.13), (3.14), and (3.15) , evaluated at $y=300\text{km}$. While the jet is stable, the wind forcing is greater than the PV flux in the upper layer, resulting in the generation of negative PV on the continental shelf in upper layer. Similarly, the drag, $(-ru_2)$, is greater in magnitude than the lower-layer PV flux, which increases the PV on the shelf in the lower layer. When the jet becomes unstable, there is a strong PV flux associated with the jet instability. In the upper layer, the magnitude of the PV flux becomes larger than the wind forcing and the PV on the shelf increases. At equilibrium, instability events are sufficiently large that the time-mean upper-layer PV flux is equal to the wind forcing and the flow reaches a statistically steady state.

The observation that instability events limit the build up of negative PV on the shelf can be used to estimate how much PV is likely to accumulate on the shelf before a steady state is reached. In particular, we can get an estimate for the steady state upper-layer PV structure, by assuming that the flow is at its critical condition for baroclinic instability.

Combining equations (3.3) and (3.4), the upper-layer zonally-averaged PV can be written as

$$\overline{q_1} = \overline{\psi_{1yy}} - F_0 \overline{\psi_1} + \frac{H_2}{H_1} \overline{\psi_{2yy}} + (f_0 + \beta y) \left(\frac{H_1 + H_2}{H_1} \right) - \frac{H_2}{H_1} \overline{q_2} + \frac{f_0 \eta_b}{H_1} \quad (3.16)$$

Taking the y derivative, setting $\frac{\partial \bar{q}_2}{\partial y} = 0$, and neglecting the terms associated with the relative vorticity, we get

$$\frac{\overline{dq_1}}{dy} \sim \beta \left(\frac{H_1 + H_2}{H_1} \right) + \frac{f_0}{H_1} \frac{d\eta_b}{dy} = \beta_{T1} \quad (3.17)$$

This effective upper-layer topographic beta describes what the effect of the topography and β is on the upper-layer background PV gradient once the flow has reached a steady state.

Figure 3.7e and Fig. 3.7f show how the upper-layer PV and upper-layer PV gradient evolve during spinup. Initially, when the flow is at rest, the topography affects the lower-layer PV gradient, but does not contribute to the upper-layer PV. As the flow spins up, negative PV builds up on the continental shelf in the upper layer until the upper-layer PV gradient approaches β_{T1} (dashed line Fig. 3.7f). The steady state upper-layer PV gradient agrees well with the effective upper-layer topographic beta, β_{T1} (Fig. 3.6b).

In this critical regime, the steady state PV structure over the shelf is largely independent of wind forcing. This implies that it is the topography which ultimately sets the upper-layer PV structure. This in turn determines the strength of the shelf break jet and the size of the mixing events across the shelf break.

3.5.3 Evolution of forces during an instability event

In this section we examine the evolution of forces during a typical instability event. Figure 3.8a and Fig. 3.8b show Hovmöller diagrams of the upper layer and lower-layer zonally-averaged zonal velocity. The simulation is the same as that shown in Fig. 3.4. Snapshots of the zonally-averaged meridional eddy PV flux, Reynolds stress divergence, interfacial stress and wind/drag are shown in panels (U1) to (U3) for the upper layer, and (L1) to (L3) for the lower layer. The times of the 3 snapshots are indicated on Fig. 3.8a and Fig. 3.8b using dashed lines and numbers.

After an instability event, there is a long period where the jet is stable and there is little eddy activity (Fig. 3.8: (U1) and (L1))). During this period, the wind is stronger than the upper-layer meridional PV flux in the region over the shelf break. This results in a buildup of negative PV on the continental shelf in the upper layer (as we saw during spinup). In the lower layer, the magnitude of the drag over the shelf is larger than the eddy PV flux, and the PV on the shelf in the lower layer increases.

As the shelf break jet builds, the barotropic and baroclinic modes grow together. The barotropic mode of the jet causes an increased drag in the lower layer, which is balanced by a positive eddy PV flux in the lower layer (Fig. 3.8: (L2)). This lower-layer balance prevents the PV on the shelf in the lower layer from increasing. This allows the lower-layer PV gradient to remain positive, and keeps the jet stable. Since the lower-layer Reynolds stress divergence is small, the lower-layer eddy PV flux is dominated by the form stress. The equal and opposite form stress in the

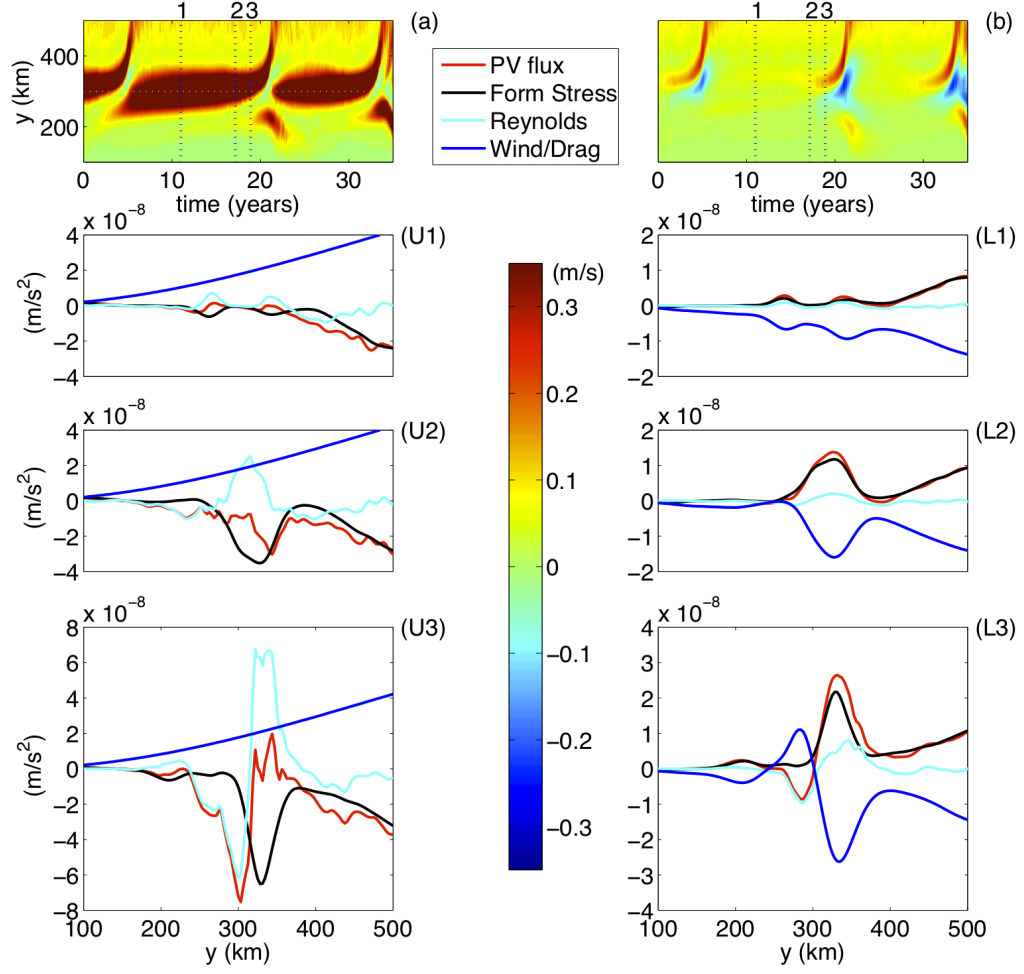


Figure 3.8: Panel (a) shows the Hovmöller diagram of the upper-layer zonally-averaged zonal velocity during a typical instability event. This simulation uses $\tau = 0.08 \frac{N}{m^2}$, $W=50\text{km}$. Snapshots of the upper-layer zonally-averaged eddy PV flux, Reynolds stress divergence, interfacial stress and wind, are shown in panels (U1), (U2) and (U3). The times of these four snapshots are shown by dotted lines in panel (a). Panels (b), (L1), (L2) and (L3) show the same fields as panels (a), (U1),(U2) and (U3), but for the lower layer.

upper layer is largely balanced by a positive Reynolds stress divergence (Fig. 3.8: (U2)). This results in convergence of eddy momentum into the jet in the upper layer, which strengthens the jet and increases the shear (Fig. 3.4b). The opposing effects of upper-layer Reynolds stress divergence and form stress, allow the upper-layer eddy PV flux to remain smaller than the wind forcing, so negative PV continues to build on the shelf, and the upper-layer PV gradient continues to build.

In panel (U2), we see regions of negative Reynolds stress divergence on the flanks of the jet. Momentum is fluxed from these regions into the jet center. Zhang et al (2011) argued that these regions of negative Reynolds stress divergence on the edges of the shelf break are essential to the jet formation through the following mechanism: Exchanges of water across the edge of the shelf break in the lower layer result in a decrease in PV flux in the lower layer over the edge of the shelf break region. This decreased lower-layer PV flux is largely caused by a decreased interfacial form stress. This results in an increased form stress in the upper layer over the edge of the shelf break region. Since the steady state upper-layer PV flux is equal to the wind forcing, an increased upper-layer form drag has to be compensated by a negative Reynolds stress divergence over the shelf break edges. The global constraint that the total Reynolds stress divergence must integrate to zero, means that there is a positive Reynolds stress divergence over the shelf break, which maintains and forces the jet. In our case, we see an asymmetry between the north and south flanks of the jet. This asymmetry determines which way the jet will drift.

At $t=19.5$ years, the jet begins to go unstable (Fig. 3.8: (U3) and (L3)). There

is a reversal of the flow direction in the lower layer on the southern flank of the jet. This is accompanied by a decrease in the Reynolds stress divergence on the southern flank of the jet in both layers. In the upper layer there is an increase in the Reynolds stress divergence in the center of the jet. This moves momentum from the southern flank of the jet into the jet center, which decelerates the southern flank of the jet, and accelerates and narrows the main jet. This results in the jet moving northwards.

The strong negative Reynolds stress divergence in the upper layer over the center of the shelf break region ($y=300\text{km}$) causes a strongly negative PV flux in the upper layer (Fig. 3.4c). The negative PV, which has built up on the shelf in the upper layer during the period of jet stability, is released back to the open ocean. In the lower layer, the large drag over the center of the shelf break causes negative PV to build on the continental shelf. This increases the lower-layer PV gradient and allows the flow to become stable again. The short burst of instability in (U3) and (L3) dominates the time-mean fields seen Fig. 3.6c and Fig. 3.6d.

3.6 Jet drifting

In the previous sections we saw that after the shelf break jet becomes unstable, it drifts northwards (Fig. 3.1). Jets are also seen to drift southwards sometimes, but are impeded by the southern boundary. The speed at which the jets drift northwards increases with increased wind forcing. This is especially apparent when comparing Fig. 3.1i and Fig. 3.1j. When the jet has moved away from the sloping

region, the bottom topography is no longer strong enough to maintain a jet and the jet disappears.

Meridional jet drifting is seen in the ocean, especially in the ACC, where jets are seen to drift and merge (Gille, 1994; Sokolov et al, 2007). A jet can be made to drift northwards when steered by bottom topography which is not zonally constant, and guides the jet along lines of constant PV (Boland et al, 2012). However, jets are also observed to drift and merge, while crossing lines of constant background PV (Thompson, 2010; Thompson and Richards, 2011). In this section, a series of numerical experiments were performed to study this jet drifting phenomenon.

3.6.1 Imposed shear simulations

To deconvolve the effects of wind forcing and bottom topography, experiments were run with the model forced using a constant imposed background shear U_s instead of using wind forcing (Pedlosky, 1979; Changheng et al, 2013). The results again showed jets drifting away from the center of the shelf break, but with the reduced drifting velocities. This suggests that wind curl contributes significantly to drift velocities. However, the presence of jet drifting without wind curl implies that there is another mechanism at work too.

As an example, we consider a simulation which uses $W=200\text{km}$ and an imposed background shear, $U_s = 0.2$. We set $\beta = 0$, and $y_0 = \frac{Ly}{2}$, so that the jet is in the center of the domain. Figure 3.9a shows lower-layer background PV gradient, β_T . The Hovmöller diagram of the upper-layer zonally-averaged zonal velocity is

shown in Fig. 3.9b.

Jets form in regions with high PV gradient and drift towards regions of lower background PV gradient (Fig. 3.9b). A white rectangle is drawn around one southward drifting jet. The black curve in Fig. 3.9c shows the time average velocity profile of this drifting jet. The blue and red curves show the time-averaged PV gradients in the upper and lower layers, respectively. The time average is taken over the period indicated by the white rectangle in Fig. 3.9b. The time average is taken following the jet, so that $y=0\text{km}$ is at the center of the jet. The upper-layer velocity is symmetric about the jet center. In contrast, the upper and lower-layer PV gradients have an asymmetry about the jet center. The asymmetry in the lower-layer PV gradient reflects the fact that the topography is steeper on the northern flank of the jet. This makes the jet more unstable on the southern flank. The upper-layer PV gradient is larger on the southern flank.

With these observations in hand, we hypothesize a possible mechanism which causes jet drifting: The curvature in the bottom topography allows the bottom slope on the one flank of the jet to be steeper than the bottom slope on the other flank of the jet. This results in the lower-layer PV gradient being asymmetric about the jet center (Fig. 3.9c). The jet is most baroclinically unstable on the flank where the lower-layer PV gradient is smallest. This results in largest mixing on the unstable flank of the jet.

Numerical experiments using barotropic models have shown that a barotropic jet can be created and maintained by “stirring” at the jet latitude in the presence of a background PV gradient (Dritschel and McIntyre, 2008; Vallis et al, 2004). The

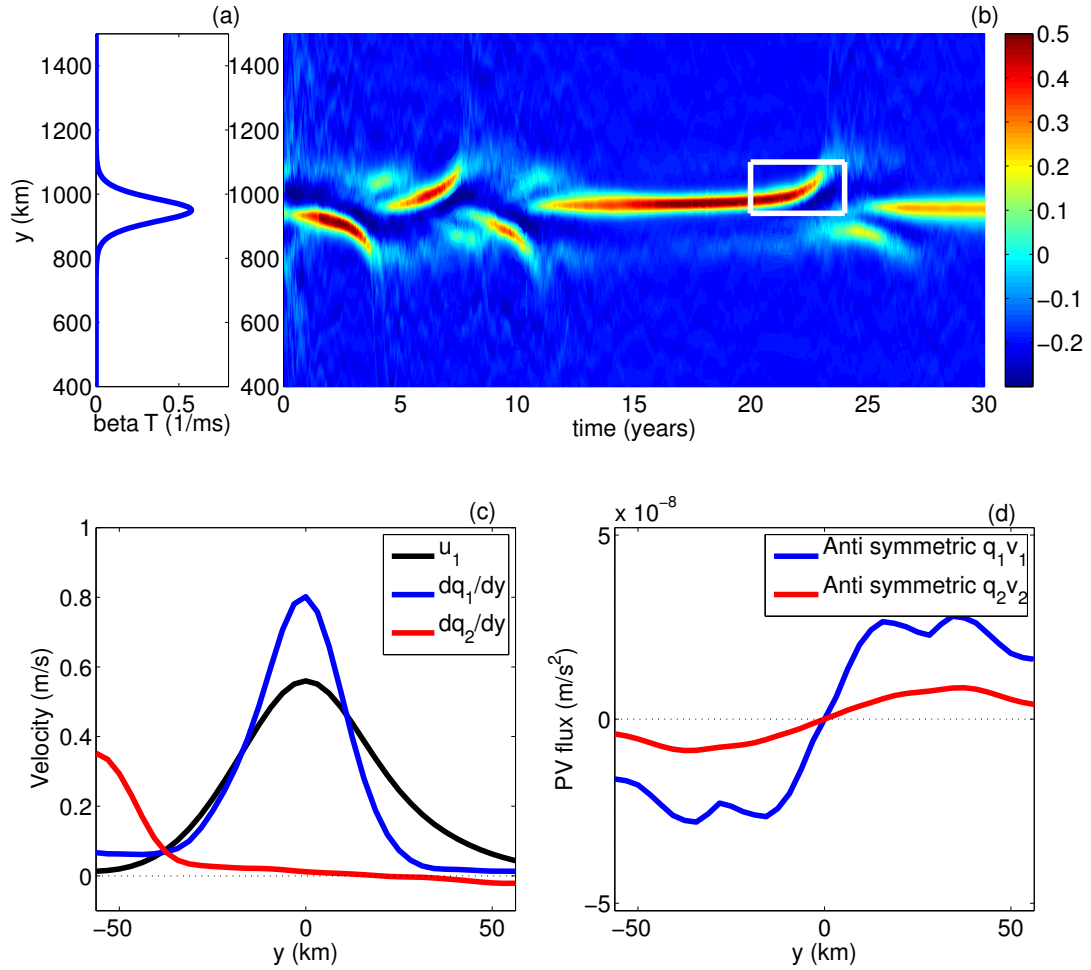


Figure 3.9: Panel (b) shows a Hovmöller diagram of the upper-layer zonally-averaged zonal velocity for a run with imposed shear, $U_s = 0.2$, $W=50\text{km}$. In this run the shelf has been moved to the center of the domain (ie: $y_0 = 950\text{km}$). The jets are able to drift in both directions from regions of strong background PV gradient to regions of weak background PV gradient. Panel (a) shows $\frac{\beta_T}{F_2}$ for this topography. Panel (c) shows the mean jet profile of the jet, which drifts through the white rectangle in panel (b). The time mean has been taken following the jet, so that the jet center is at $y=0\text{km}$. Panel (c) also shows the time-mean meridional PV gradient of the drifting jet in the upper and lower layers. The lower-layer PV gradient is asymmetric about the center of the drifting jet. Panel (d) shows the asymmetric part of the upper and lower-layer PV flux about the jet center. The positive meridional PV flux causes the jet to accelerate on the northern side of the jet, and makes the jet drift northwards.

“stirring”, which is a parametrization of the effect of baroclinic instability, creates Rossby waves which radiate away from the stirring latitude and cause momentum to be fluxed into the center of the jet. When the latitude of maximum stirring is not in the center of the jet, Rossby waves are generated preferentially from the flank of the jet where the jet is most unstable, which causes momentum flux into the unstable flank of the jet. This causes the peak of the jet to drift towards the unstable flank.

Figure 3.9d shows the asymmetric part of the upper and lower-layer meridional eddy PV flux

$$(\overline{q'_i v'_i})_{asym}(y) = \frac{\overline{q'_i v'_i}(y) - \overline{q'_i v'_i}(-y)}{2} \quad (3.18)$$

where $y=0\text{km}$, is the center of the jet. In Fig. 3.9d we see that there is more PV mixing on the northern flank of the jet. This is consistent with the jet drifting northwards.

The gradient in the background PV gradient is controlled by the parameter W . Figure 3.10 shows how the average jet drift velocity changes with the shelf break width, W . In these simulations, we use $y_0 = \frac{L_y}{2}$ (ie: the shelf is in the center of the domain). The drift velocity is measured at $y=1000\text{km}$ (50km north of the center of the domain). In this figure, we see that the drift velocity decays exponentially with W . It is also observed that the jets do not drift when a linear slope is used (not shown).

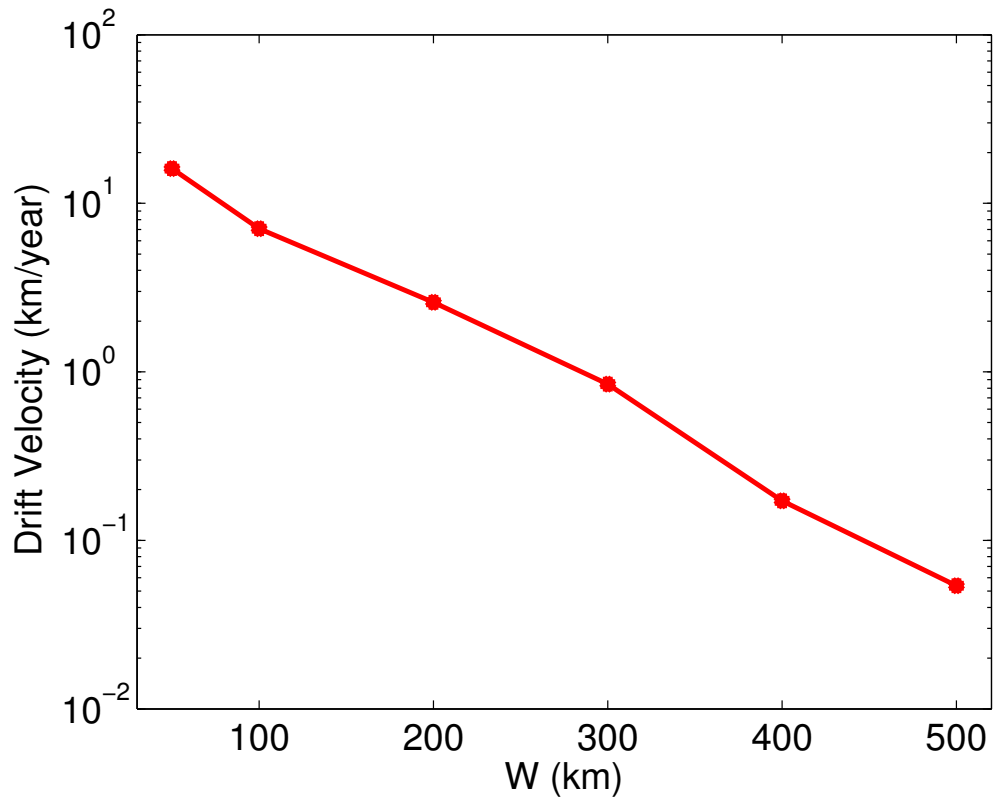


Figure 3.10: The meridional jet drift velocity is shown for different values of the parameter W . The drift velocities are measured at $y=1000\text{km}$ (50km north of the center of the domain). Simulations were forced using a background shear $U_s = 0.2\text{m/s}$. The simulations used a hyperbolic tangent shelf described by equation (3.8). The shelf was positioned in the center of the domain with $y_0 = \frac{L_y}{2}$. The drift velocity decay exponentially with W .

3.6.2 Simplest geometry for jet drifting

The simplest topography which has non-zero gradients in β_T is a parabolic bottom topography. Runs are performed using an imposed background shear, U_s , and a parabolic bottom topography described by

$$h_b(y) = ay^2 + by \quad (3.19)$$

where $a = \frac{Q}{2}$ and $b = (-\frac{QL_y}{2} - \frac{h_0}{2W})$. The parameter $Q = \frac{d^2h_b}{dy^2}$ controls the lower-layer background PV gradient (we set $\beta = 0$ for these experiments).

The topography is constructed such that $h_b(0) = 0$, $h_b(L_y) = -\frac{h_0}{2W}L_y$, and the $\frac{dh_b}{dy}\left(\frac{L_y}{2}\right) = -\frac{h_0}{2W}$. In this way, the average lower-layer meridional background PV gradient across the domain is equal to the PV gradient at $y = \frac{L_y}{2}$, and is independent of Q . This average PV gradient is chosen to be equal to the maximum lower-layer background PV gradient in the original set of experiments, so that we are in the same parameter regime. The range of Q used is limited in order to make sure that the slope is always negative (ie: $|Q| < \frac{h_0}{WL_y}$).

Figure 3.11a shows the jet drifting speed vs Q for runs using $U_s = 0.3$. The jet drift velocities were measured at $y = \frac{L_y}{2}$. The black curve in Fig. 3.11a shows results from simulations using $W=100\text{km}$. The results show that jets drift from regions of strong lower-layer background PV gradient to regions of weak lower-layer background PV gradient. The speed of the drifting jet varies linearly with the parameter $Q = \frac{d^2h_b}{dy^2}$, which controls the gradient of the lower-layer background PV gradient. The jets drift northwards for $Q > 0$, southwards for $Q < 0$, and did

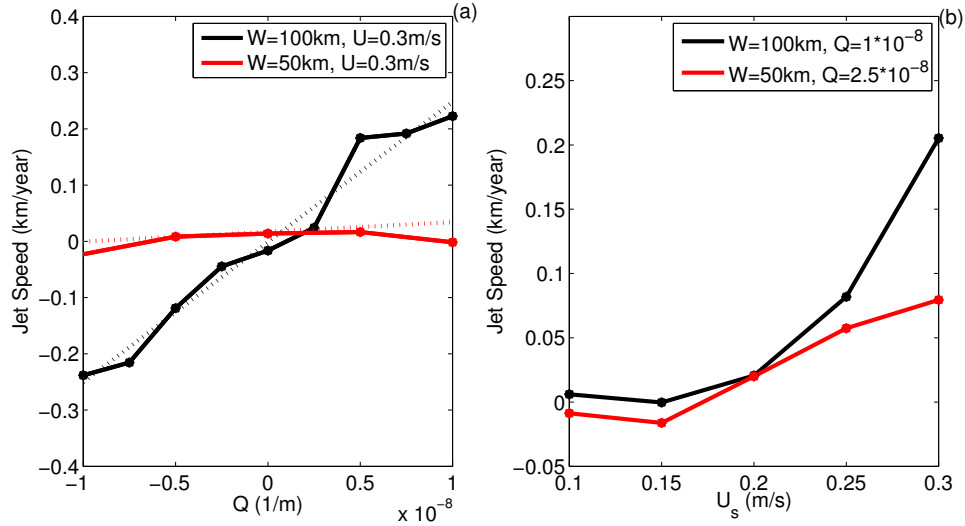


Figure 3.11: Panel (a) shows the meridional jet drifting velocity for different values of $Q = \frac{\partial^2 h_b}{\partial y^2}$. The black curve uses $W=100\text{km}$ and imposed shear, $U_s = 0.3$. The red curve uses $W=50\text{km}$ and $U_s = 0.3$. The jets drift northwards for positive Q and southward for negative Q . Panel (b) shows the jet drifting velocity for different values of imposed shear, U_s . The black curve uses $W=100\text{km}$ and $Q = 10 \times 10^{-9}$. The red curve uses $W=50\text{km}$ and $Q = 25 \times 10^{-9}$. Both sets of simulations used a parabolic bottom topography.

not drift for linear bottom topographies with $Q=0$.

When Q is held fixed, the jet drift velocity decreases with bottom slope (not shown). For sufficiently steep bottom topography (small W), the large slope stabilizes the flow and the jet does not drift at all. The red curve in Fig. 3.11a shows results for a set of simulations using $W=50\text{km}$, where the jet does not drift. For fixed values of W and Q , the jet drifting speed increases with imposed background shear U_s , although the relationship was not linear. Below a shear threshold, the jet does not drift. Once the shear is sufficiently high, the jet drifting speed increases sharply for increased shear (Fig. 3.11b).

The jet velocities observed in Fig. 3.11a and Fig.3.11b are much smaller than those seen in Fig. 3.1, which used a hyperbolic tangent topography. This is because (a) the gradients of the background PV gradients are much larger in the simulations which used the hyperbolic tangent bottom topography and (b) the curl of the wind forcing contributes significantly to the jet drifting.

In real world continental shelf breaks, the large gradients in bottom slope suggest that jet drifting away from the continental shelf breaks is likely to occur along many coastal margins. To our knowledge, this has not yet been observed.

3.7 Confirmation of drifting jets using primitive equation model

A series of numerical experiments were carried out using MITgcm (Marshal et al, 1997a,b). The aim of these experiments was to see if it was possible to reproduce jet drifting using a primitive equation model.

The model used a horizontal resolution of $\Delta x = 2.5\text{km}$. The model used 25 vertical levels with levels being closely spaced near the surface and further apart at depth. The K-Profile Parametrization (KPP) was used to account for vertical mixing (Large et al, 1994). The viscosity was tuned to give an eddying ACC. A linear bottom drag was used with a bottom drag coefficient, $r = 2 \times 10^{-4}$.

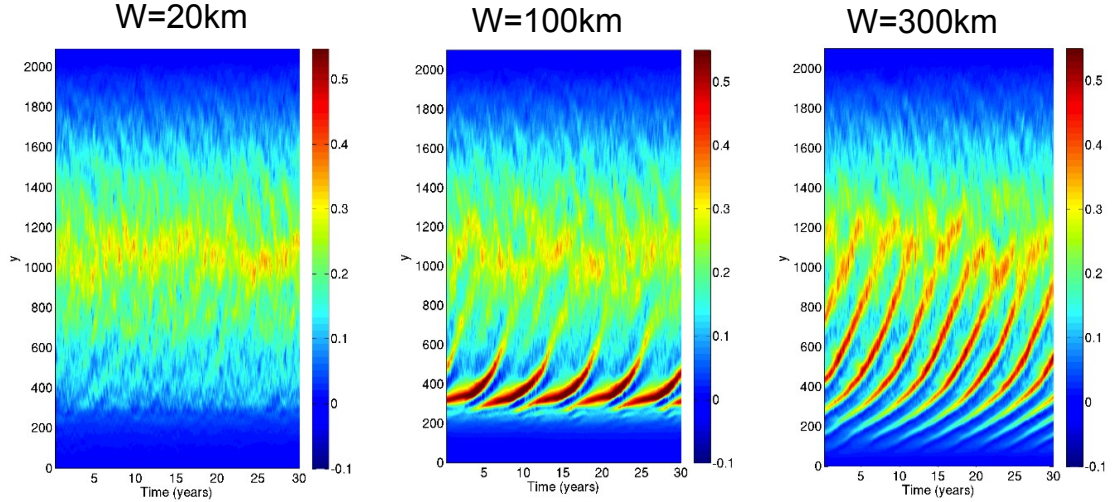


Figure 3.12: Simulations run using MITgcm primitive equation model. Figure shows the zonally-averaged zonal velocity on the surface for simulations using (a) $W=20\text{km}$, (b) $W=100\text{km}$, (c) $W=300\text{km}$. Jets which form over the continental shelf break region are seen to drift northwards.

A linear equation of state was used with salinity fixed, so that the temperature alone controlled the density of the water. It is unlikely that the non-linear nature of the equation of state of sea water has a major dynamical effect on the cross-shelf exchange problem.

The experimental setup was similar to the setup used in the QG experiments (described above). The domain was a channel with no-slip boundaries in the north and south, and periodic boundary conditions in the east and west. The domain

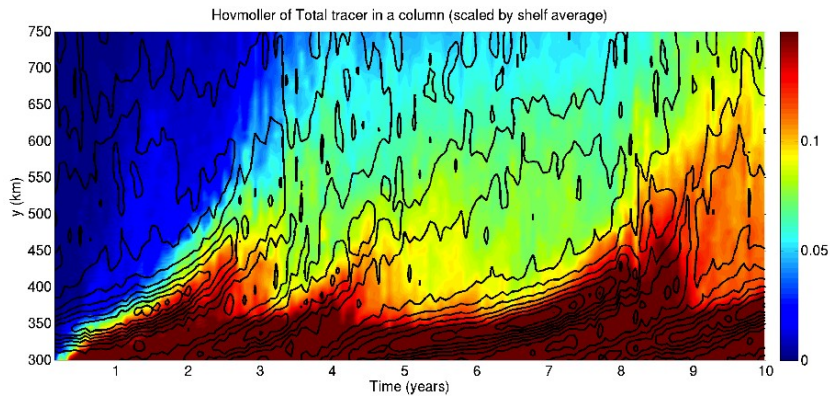


Figure 3.13: Hovmöller diagram of the zonally-averaged surface tracer concentration for a run using $\tau_0 = 0.1$ and $W=100\text{km}$. Black lines show the surface velocity contours of the jet. Cross shelf tracer fluxes coincide with the jet drifting northwards.

has dimensions $L_x = 1050\text{km}$ and $L_y = 2100\text{km}$. The model used a continental shelf topography in the south of the domain described by equation (3.8). The flow was forced by a wind stress, described by equation (3.9).

3.7.1 Drifting Jets

Figure 3.12 shows a hovmöller diagram of the zonally-averaged zonal surface velocity for runs with $\tau_0 = 0.1$. The simulations in panels (a), (b) and (c) used

$W=20\text{km}$, $W=100\text{km}$ and $W=300\text{km}$, respectively. The simulations results are qualitatively similar to those found using the QG model. For very narrow shelves, a jet does not form over the topography. For wider shelves, a jet forms over the shelf break region and drifts northwards. The period of jets drifting decreases with W . The strength of the jet increases with the slope of the bottom topography (provided the width of the shelf break is above a certain threshold value).

A numerical tracer was used to quantify mixing caused by the jet drifting. The tracer was initiated to be equal to one for $y < 100\text{km}$, and equal to zero for $y > 100\text{km}$, and then was allowed to freely evolve with the flow for 10 years. Figure 3.13 shows a hovmöller diagram of the zonally-averaged surface tracer concentration for a run using $\tau_0 = 0.1$ and $W=100\text{km}$. The black lines in Fig. 3.13 show the velocity contours of the zonally-averaged zonal surface velocity. Figure 3.13 shows that the transport of the tracer across the shelf break coincides with the jet drifting northwards.

These provisional primitive equation simulation give us further confidence that the jet drifting is a robust feature of ocean flows. A comparison between the QG and MITgcm simulations will be the topic of future work.

3.8 Conclusions

The exchange of water across a zonally constant continental shelf break adjacent to a turbulent current is explored using a 2-layer QG model. Model results

show the development of a strong zonal jet which runs along the continental shelf break. This shelf break jet is stabilized by the presence of large gradients in the bottom topography, and can remain stable for tens of years. While the jet is stable, shear builds up in the jet, which results in a steepening of isopycnals. Once this shear reaches a critical level, the flow becomes baroclinically unstable, the shear collapses and the jet drifts northwards. Passive tracers and PV fluxes are used to conclude that these baroclinic instability events coincide with enhanced mixing across the continental shelf break.

Analytic formulae and numerical experiments show that the time-averaged upper-layer cross-shelf exchange is independent of the zonally constant bottom topography. Our results suggest that the time variability of the cross-shelf exchange is controlled by the slope of the continental shelf break. The strength (and frequency) of mixing events is determined by the amount of shear that build up in the shelf break jet before it becomes unstable. The maximum shear which can buildup in the shelf break jet is set by the onset of baroclinic instability.

Three regimes are identified for the flow over the continental shelf break: sub-critical, critical and super-critical. For very narrow shelves, the shear over the shelf break is always smaller than the minimum shear required for baroclinic instability, and hence the flow is sub-critical. In this regime, the shelf break region is smaller than the typical eddy size, and a jet does not form over the continental shelf break. For shelves of intermediate width, one strong jets forms over the continental shelf break. The shear in the jet builds until the baroclinic instability condition is satisfied, after which the jet becomes unstable, drifts northwards. This

results in a large amount of mixing. Finally, for wide shelves, the flow is always super-critical. In this regime, the jet is constantly unstable and drifts northwards. For these wide shelves multiple jets exist over the shelf break simultaneously. The amount of shear build up in this regime is insensitive to the shelf break slope and instead depends on the wind stress and on the deformation scale, L_e .

For realistic shelf break slopes (critical regime), we observe that cross-shelf mixing occurs in discrete events which can be separated by up to 50 years. This intermittent low frequency variability is inherent to the QG dynamics of jets over steep topography. Long periods of jet stability are followed by short periods of enhanced mixing. This low-frequency intermittent oscillation controls the distribution of PV in the domain. During the quiescent periods, negative PV builds up on the continental shelf in the upper layer due to the presence of wind forcing. This increases the upper-layer PV gradient which allows further shear to build in the shelf break jet. During instability events, this negative PV is fluxed back into the open ocean. The inverse proportionality between the strength and frequency of instability events means that the time-averaged PV flux is independent of the shelf break topography.

The idealized simulation described above give us insight into the dynamics cross-shelf exchange mechanism. The results suggest that there could be low frequency variability in the cross-shelf exchange, which is intrinsic to the cross-shelf dynamics.

Chapter 4

Intrusion of warm surface water beneath the McMurdo Ice Shelf, Antarctica

4.1 Introduction

The melting of the floating ice shelves around Antarctica is an important factor in determining the Antarctic Ice Sheet mass balance. Recent observations have shown that accelerating ice shelf melt rates are closely linked with increased ice velocities of the grounded ice flowing into those ice shelves (Pritchard et al, 2012; Horgan et al, 2011). This results in an increase in the mass flux from the Antarctic continent into global oceans. However, due to the scarcity of data, the processes involved in ice shelf melting and the mechanisms delivering heat to the ice shelves, are still uncertain. This uncertainty significantly reduces our ability to project sea-level rise in the coming century.

Ice shelf melting processes and the intrusion of warm water beneath ice shelves can be described by three modes (Jacobs et al, 1992; Hattermann et al, 2012), as shown in the schematic in Fig. 4.1 (Craven, pers. comm., 2012). Mode 1 is the intrusion of High Salinity Shelf Water (HSSW) into the ice shelf cavities along the sea-floor bottom. HSSW is formed due to brine rejection from sea-ice formation. Since the HSSW is formed at the surface and the freezing point of salt water decreases with increased pressure, the HSSW is warmer than the freezing point at the grounding line and its intrusion causes melting at the grounding line (MacAyeal, 1984). Mode 1 circulation causes melting in the grounding line areas of the Ross, Filchner-Ronne and Amery Ice Shelves (Jacobs et al, 1992). Mode 2 is the intrusion of Circumpolar Deep Water (CDW) into the ice shelf cavity at intermediate depths. The CDW can be more than 4°C warmer than the in-situ freezing points and causes rapid melting. Mode 2 melting is largely responsible for the recent accelerated melt rates found on ice shelves by the Amundsen and Bellingshausen Seas (Jacobs et al, 2011). Lastly, a mode 3 intrusion is caused by warm surface waters that enter the ice shelf cavity near the surface, forced by tides and/or seasonal currents, causing melting near the ice front (Jacobs et al, 1992).

The three modes of circulation are not entirely distinct and can overlap and interact with one another. Interaction between the modes can be important for determining the heat and mass exchange beneath ice shelves (Hattermann et al, 2012). Nevertheless, the modes provide a good framework for understanding ice shelf melting processes. The seasonal dependence of the different intrusion modes has been observed with satellites (Horgan et al, 2011; Bindschadler et al, 2011),

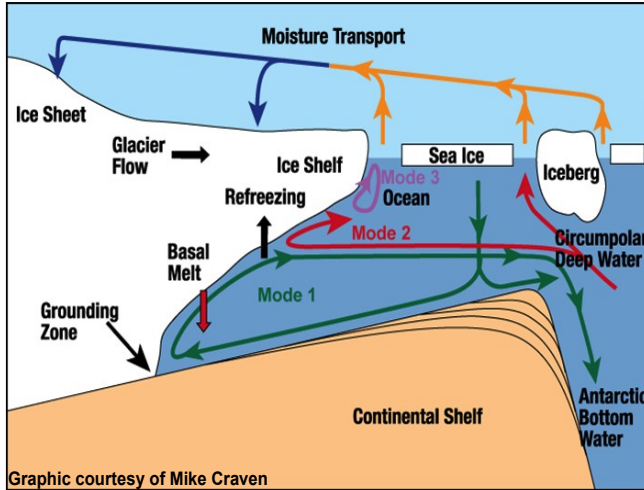


Figure 4.1: Schematic showing the three modes of warm water intrusion.

moorings (Nicholls, 1996; Makinson et al, 2006) and in models (Holland et al, 2003; Dinniman et al, 2007, 2012), but is still not well understood. Here we focus on mode 3 intrusions.

Mode 3 intrusions are likely to be present to some extent on all of the Antarctic ice shelves and are responsible for 173Gt per year of ice shelf melt, which is a significant fraction of the total annual ice shelf attrition (544Gt/yr) (Jacobs et al, 1992). The melting due to mode 3 currents occurs within 100km of the ice front,

and leads to exponential thinning of the ice shelf towards the ice front (Horgan et al, 2011).

As a step towards further understanding of mode 3 intrusions, results from measurements made beneath the McMurdo Ice Shelf at Windless Bight (WB) in 2011-2012 are presented. The McMurdo Ice Shelf was chosen for this study because the long history of measurements in McMurdo Sound means that we have a good understanding of the major current systems and oceanography in the region. Furthermore, recent measurements below the sea ice south of Ross Island (Hunt et al, 2003; Mahoney et al, 2011; Robinson and Williams, 2012) have shown that there is a warm water summer signal, which is a likely candidate for a regular mode 3 intrusion.

A Ross Sea regional model is run to simulate the summer intrusion of warm water in McMurdo Sound. Model simulations are compared with observations made near the ice front and under the ice shelf. The observational data and the model data are both used to estimate the temperature impact of this warm water intrusion. The model results are also used to determine the source and timing of the warm water intrusion.

4.2 Background oceanography

Oceanographical observations since the 1980's indicate that the dominant current system in McMurdo Sound is a clockwise circulation (Mitchell and Bye, 1985;

Lewis and Perkin, 1985; Robinson et al, 2010). Warmer waters enter McMurdo Sound in the north-east from the Ross Sea, and run along the eastern boundary of McMurdo Sound (see Fig. 4.2). Most of this water recirculates around the sound and leaves McMurdo Sound along the western boundary of the sound. Some of this water makes its way to the south-east, under the ice shelf. There is also a flow of water out from under the ice shelf in the west, that joins the main ocean current exiting McMurdo Sound along the western boundary of the sound. The circulation is summarized in Fig. 4.1a in Robinson et al (2010).

The water that moves under the ice shelf is directed by the bathymetry around Ross Island towards WB, following contours of constant ocean water column thickness (Hunt et al, 2003; Mahoney et al, 2011) (see Fig. 4.2d). Water is able to pass under the ice shelf since the McMurdo ice front is only about 20m thick. The ice thickness increases to 200m over a distance of about 10km (Kovacs et al, 1993). The bottom ocean currents in the strait south of Ross Island are fairly consistent all year round since they are strongly controlled by the bathymetry (MacAyeal, 1984; Robinson et al, 2010), while higher up in the water column the velocities show a seasonal variation (Mahoney et al, 2011). In summer, a current in the upper half of the water column wraps around Cape Armitage (CA, Fig. 4.2a) towards WB (Mahoney et al, 2011). This current is responsible for the mode 3 intrusion and subsequent enhanced melting that occurs in the summer months.

The two significant annual oceanographic signals that can be seen under the McMurdo Ice Shelf are the warm water summer signal, which enters through McMurdo Sound in December/January (Hunt et al, 2003; Mahoney et al, 2011; Robinson and

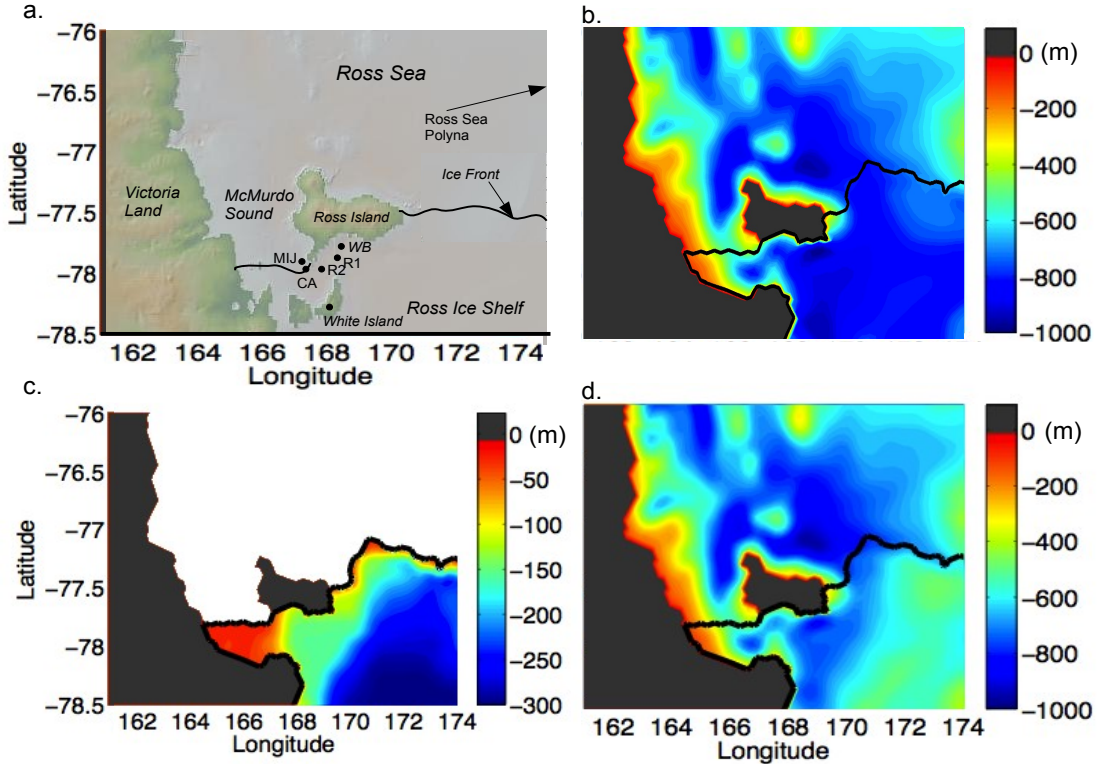


Figure 4.2: Panel (a) shows a map of the region around McMurdo Sound. The ocean south of the black line is underneath the ice shelf. WB shows the location of Windless Bight where the boreholes in this study were drilled. R1 and R2 are the two boreholes in Robinson et al (2010). CA shows where the Cape Armitage measurements (Mahoney et al, 2011) were made. MIJ is the McMurdo Inlet Jetty (Hunt et al, 2003). CA and MIJ are covered by multi-year sea ice near the ice front, while R1, R2 and WB are on the McMurdo Ice Shelf. Panel (b) shows the bathymetry around McMurdo Sound as used in the circulation model. Panel (c) shows the depth of the base of the ice shelf (below MSL). Panel (d) shows the thickness of the water column. The black line in panels b, c and d represents the location of the ice front in the model (Davey, 2004).

Williams, 2012), and the arrival of ice shelf water in winter from under the Ross Ice Shelf (Littlepage, 1965; Leonard et al, 2006; Mahoney et al, 2011; Robinson and Williams, 2012). This paper focuses on the summer warm water intrusion.

Year-long temperature moorings have been deployed underneath the sea ice at the McMurdo Inlet Jetty (MIJ) and at CA in 1999, 2000 (Hunt et al, 2003) and 2008 (Mahoney et al, 2011). Both Hunt et al (2003) and Mahoney et al (2011) observed increased temperatures in the upper levels of the ocean, arriving in December, peaking in January or February and then gradually decreasing in March and April. This warm water signal was also observed by moorings and CTD measurements made under the sea ice in summer in 2005, 2006 and 2009 (Robinson and Williams, 2012). Robinson et al (2010) made measurements through two boreholes in the McMurdo Ice Shelf in January 2003 (marked R1 and R2 on Fig. 4.2a). In their study, Robinson et al (2010) did not observe the warm waters seen by Hunt et al (2003) and Mahoney et al (2011), however, it was noted that this was an anomalously cold year with heavy sea-ice conditions in McMurdo Sound, a large iceberg B-15a disturbing regular circulation patterns, and a late opening of the RSP (Robinson et al, 2010; Robinson and Williams, 2012) . Robinson et al (2010) also observed barotropic diurnal tides with a maximum amplitude of $\sim 0.2\text{m/s}$ underneath the ice shelf.

4.3 Observations at Windless Bight

4.3.1 Deployment Details

In November 2011, two boreholes were completed through the McMurdo Ice Shelf at Windless Bight ($77^{\circ}46.550'\text{S}$, $167^{\circ}32.400'\text{E}$) and instrumented with Distributed Temperature Sensing (DTS) fiber optics, as well as traditional pressure and temperature transducers and platinum resistive thermometers. The DTS ca-

bles measured temperature in the ice shelf and ocean integrated over 1m intervals (Tyler et al, 2009). The DTS sensor had a temperature resolution of 0.03°C, and an accuracy of 0.05°C. DTS temperature measurements were made every eight times a day from November to March, and then four times a day during the winter in order to conserve electrical power. A summary of the deployment details is outlined in below. A more complete description of the deployment and calibration procedures can be found in Tyler et al (2013).

4.3.2 Drilling Details

Windless Bight is located 20 km east of McMurdo Station on the McMurdo Ice Shelf, a subsidiary of the larger Ross Ice Shelf. To the north and west of Windless Bight is Ross Island, which separates Windless Bight from McMurdo Sound (see Fig. 4.2). The Ross Ice Shelf lies to the east and south east of Windless Bight. The two boreholes drilled in this study were positioned at 77°46.550'S , 167°32.400'E.

Two boreholes were drilled, 40 meters apart. The depth of the ice in the boreholes was 193m. One fiber optic cable (Cable 1) was deployed into BH1. Cable 1 extended 223m vertically downwards, through the ice and 30 meters into the ocean. A pressure transducer is attached to the bottom of Cable 1. BH2 contained two different fiber optic cables. The shorter of the two (Cable 2) extended 203m vertically downwards through the ice and 10 meters into the ocean. The last cable (Cable 3) was deployed 792m vertically downwards, through the ice and into 599m of ocean. A second pressure transducer was attached to Cable 3. Due to depth limitations of the pressure transducer, it was suspended 150 meters above the end of the Cable 3.

To penetrate the 193 meter thick ice shelf, a combination of dry-hole electro-mechanical and hot point drills were used. Because the installation of fiber optic cable requires a slim (< 3cm diameter) hole accessible only during installation, it was not necessary to complete and maintain a large diameter open hole to the ocean. Bottom hole temperatures were measured periodically using either fiber optic sensing or traditional borehole logging to estimate the actual depth of the ice/water interface.

The boreholes each took approximately four days to drill and cable installation took less than one hour. After 5 hours, these cables were solidly frozen from 37m below surface (global sea level). Consequent installation of multiple cables/sensors was possible in BH2.

4.3.3 Instruments and Calibration

Four PT100 thermometers were placed in BH2 at depths of 2.5 meters, 22.5 meters, 32.5 meters and 37.5meters below the surface to help with the calibration of the Distributed Temperature Sensing. Three cables were deployed close together so that we could compare the performance of cables made by different manufactures (results to be published separately), and so that we could use the different data sets for calibration purposes. The borehole setups are summarized in Fig. 4.3.

The cables through the ice measure temperature using Distributed Temperature

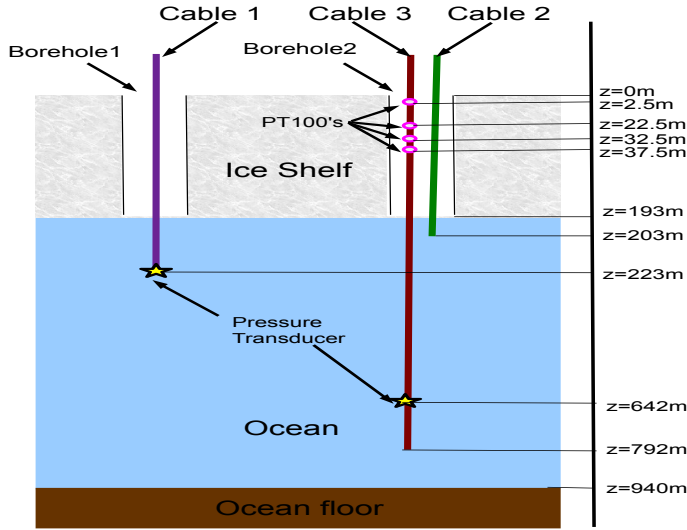


Figure 4.3: Two boreholes were drilled through the ice 20 meters apart. Three cables were deployed through the boreholes. Pressure transducers and PT100's are connected to the cables as shown above.

Sensing (DTS). DTS can be thought of as a Raman LIDAR within an optical fiber, and is now widely used in industry and environmental applications to provide high spatial ($< 1\text{m}$) and temporal (0.1 Hz) resolution of environmental temperatures along fibers (Sekler et al, 2006; Tyler et al, 2009). Distributed temperature sensing requires independent temperature measurement to improve accuracy. For this we used the pressure transducers and the PT100's described above (10mK resolution). A three point calibration procedure was used, following the calibration methods outlined in van de Giesen et al (2012). The redundant independent temperature measurements were used for validation and error estimation. Calibrated values result in an average root mean square error (RMSE) value of 0.03°C , indicating precision to that level.

Calculation for conservative temperature, used in Fig. 4.4a, are based on the Thermodynamic Equation Of Seawater - 2010 (TEOS-10). Absolute salinity was assumed to be 35g/kg. Note that the model uses potential temperature rather than conservative temperature.

Further details about the instrument deployment and the calibration methods can be found in Tyler et al (2013).

4.3.4 Ocean Temperature Measurements

The upper ice surface of the McMurdo Ice Shelf at WB is 37m above sea level. The ice shelf thickness is 193m, so that the ice shelf extends 156m below sea level. The depth of the ocean below the ice surface at WB was measured as 940 ± 60 m using seismic sensors (Anandakrishnan, pers. comm., 2011), meaning that the ocean water column thickness is 747 ± 60 m. (The model ocean thickness at WB is 697.82m and the model ice draft is 105m below sea level). The longest of the DTS cables deployed extended through the ice shelf and through 599m of ocean.

Figure 4.4a shows a detailed temporal evolution of the warm water intrusion at WB measured using the DTS system from November 2011 until June 2012. The warming of the upper water column begins in late December and continues through March. After March the temperatures start to decline to mean temperature at depth. The warmest layer (greater than -1.6°C) remains isolated to the upper ~ 50 m of the water column and warm water (greater than -1.8°C) extends as

deep as $\sim 200\text{m}$ below the base of the ice shelf. At depths greater than $\sim 300\text{m}$ below the base of the ice shelf, the ocean temperature remains constant $\sim -1.9^\circ\text{C}$, which represents local surface freezing point for typical salinities. This graph represents ~ 3 million individually recorded temperatures. The red curve in Fig. 4.5a shows the maximum temperature recorded at WB.

4.3.5 Estimates Ice Shelf Melting at Windless Bight Using Observed Data

In this section we use the DTS temperature measurements to estimate the melt rate at the base of the ice shelf at WB. Since only temperature data was collected, the calculation below presents the melt rate as a rescaling of the observed temperature, and represents our best guess of the melt rates given the lack of ancillary data.

The magnitude of the conductive heat flux from the ice base into the ice shelf is small compared to the turbulent heat flux from the ocean into the ice shelf base (McPhee, 2008). This implies that the melt rate of the base of the ice shelf is set by the heat flux from the ocean into the ice shelf base. Since the temperature of the ice shelf base is constrained to be equal to the in-situ freezing point, the heat fluxed into the ice shelf base will result in an equal latent heat flux (Holland and Jenkins, 1999). This interface heat balance is described by the simplified equation

$$\langle w'T' \rangle = w_0 Q_L \quad (4.1)$$

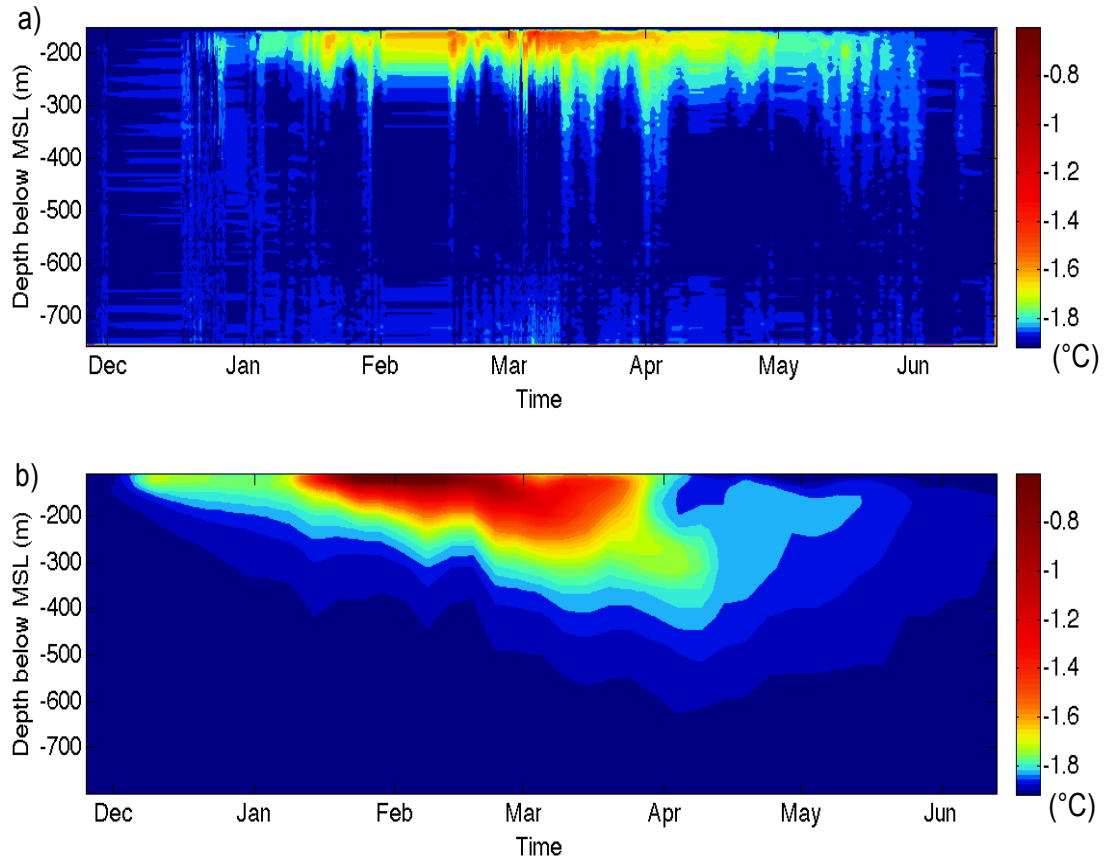


Figure 4.4: (a) Observations of the ocean temperature profile at Windless Bight from November 2011 to June 2012 made using a DTS fiber optic cable. Data gaps in this figure have been interpolated. (b) Model ocean temperature profile at Windless Bight from November 2010 to June 2011. The vertical axis is depth in meters below mean sea level (MSL) beginning at the base of the ice shelf. Note that the ice draft measure at Windless Bight onsite was 156m below sea level, while the model ice draft at Windless Bight is 105m. A significant warm water signal can be seen in the upper 200m of the water column.

Here $\langle w'T' \rangle$ is the turbulent heat flux from the ocean into the ice, w_0 is the vertical velocity of the ice base due to melting or freezing, and Q_L is the latent heat temperature parameter for ice (McPhee, 2008).

Observations below sea ice suggest that turbulent heat flux of the ocean can be

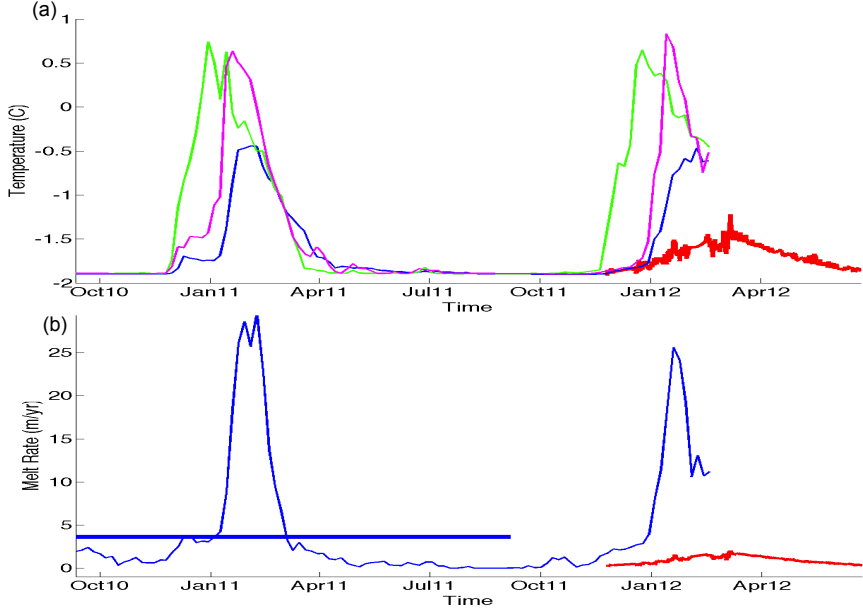


Figure 4.5: Panel (a) shows the time evolution maximum model temperature in the water column at the selected points to the north (green) and west (magenta) of Ross Island, and also at Windless Bight (blue) to the south of Ross Island. The positions of these points are indicated in Fig. 4.10 in the corresponding colors. The red curve in panel (a) shows the maximum temperature observed at WB using DTS. In Panel (b), the blue curve shows the time evolution of the model melt rate found at the grid point closest to Windless Bight. The annual mean from Sept 15, 2010 to Sept 14, 2011 is shown with a blue horizontal line. The red curve shows the melt rate estimated using observed ocean temperatures at WB.

approximated by the formulae

$$\langle w' T' \rangle = St_* u_{*0} (T_w - T_f(S_w)) \quad (4.2)$$

Here St_* is the bulk Stanton number , u_{*0} is the frictional velocity, T_w is the ocean temperature from 5 to 10m below the ice-ocean interface, and $T_f(S_w)$ is the freezing point that the sea water at the ocean-ice interface would have if it were at the salinity of water 5 to 10m below the ice-ocean interface (McPhee, 1992, 2008). The

Stanton number, formally defined by equation (2), is an empirical parameter that governs the turbulent exchange of heat though a fluid, and has been found to be approximately constant in the parameter regime considered here (McPhee, 1992).

This bulk formulae is useful in that it allows us to estimate the turbulent heat flux into the ice shelf base using only the far-field conditions. This allows us to parametrize the competing effects of turbulent mixing, which brings heat to the ice-ocean interface, and stratification near the ice-ocean interface, which suppresses heat exchange, in terms of more easily measurable variables, and allows us to estimate melt rates. This approach is widely used in numerical models where the complex small-scale behavior cannot be resolved. The use of this bulk formulae has been well tested below sea ice (McPhee, 1992), and has been partially verified for use under ice shelves (Jenkins et al, 2010). Walker et al (2013) showed that this approximation is reasonable provided the ice shelf base is not too steep and ocean temperatures are sufficiently close to freezing. In our case, the ice shelf base has a slope of ~ 0.01 (Kovacs et al, 1993) and the temperatures observed are less than one degree above freezing, so the errors introduced by this bulk formula are likely to be small.

Following McPhee (2008), we assume that $w_0 = \frac{\rho_{ice}}{\rho_w} \dot{m}$. This implies

$$\frac{\rho_{ice}}{\rho_w} \dot{m} Q_L = St_* u_{*0} (T_w - T_f(S_w)) \quad (4.3)$$

Solving for the melt rate gives

$$\dot{m} = St_* u_{*0} (T_w - T_f(S_w)) \frac{\rho_w}{\rho_{ice}} (Q_L)^{-1} \quad (4.4)$$

At WB the pressure at the base of the ice shelf is ~ 156 db. Robinson et al (2010) measured the salinity below the McMurdo ice shelf to be between 34.35 to 34.72psu. This implies an in-situ sea-water freezing point of $T_f(S_w) \sim -1.99^\circ\text{C}$ (using salinity 34.5psu). The latent heat temperature parameter is given by $Q_L = \frac{L}{c_p}$ (McPhee, 2008). Here c_p is the specific heat capacity of the ice at constant pressure, and L is the specific latent heat of melting. We use $c_p = 2093 \frac{J}{kgK}$ (Hooke, 2005). Since the ice at the shelf glacier base is fresh, we use $L = 333.5 \times 10^3 \frac{J}{kg}$. This gives $Q_L = \frac{L}{c_p} = \frac{333.5 \times 10^3 J kg^{-1}}{2093 J kg^{-1} K^{-1}} = 159.3 \text{K}$.

The frictional velocity, u_{*0} is given by $u_{*0} = \sqrt{c_d} U_m$, where c_d is the dimensionless drag coefficient, and U_m is the mixed layer velocity (Holland and Jenkins, 1999; McPhee, 2008). We use $c_d = 1.5 \times 10^{-3}$ (Holland and Jenkins, 1999). This number is subject to uncertainty since it depends on the surface roughness at the ice-ocean interface at WB, which is not known.

Robinson et al (2010) observed that ocean velocities beneath the ice shelf are dominated by diurnal tides. At site R2 (see Fig. 4.2a), Robinson et al (2010) observed an average velocity of 0.05m/s to the north east, and a maximum speed of > 0.15 m/s at high tide. We can get a rough estimate of the average speed under the ice shelf by adding a component due to mean currents and a component due to tides. The simplest periodic velocity function that has a mean equal to

0.05m/s and a maximum equal to 0.15m/s is given by $u(\theta) = 0.05 + 0.1\sin(2\pi\theta)$. To get the average speed, we integrate the absolute value of this velocity over one period.

$$U_m = \int_0^1 |(0.05 + 0.1\sin(2\pi\theta))| d\theta = 0.072 \text{m/s} \quad (4.5)$$

This gives a frictional velocity $u_{*0} = 0.0028 \text{ms}^{-1}$. We use $\rho_{ice} = 920 \text{kgm}^{-3}$ and $\rho_w = 1028.4 \text{kgm}^{-3}$. Finally, we use a bulk Stanton Number $St_* = 0.0057$ (McPhee, 2008). We let T_w be the ocean temperature 10m below the ice ocean interface that we observe using DTS.

Equation (4) allows us to estimate the melt rate at the base of the ice shelf at WB. This melt rate is plotted by the red curve in Fig. 4.5b. The peak melt rate is 2.0m/yr, and occurs on March 7th 2012. If we assume that the melt rate from the end of June to the middle of November is constant and equal to the average melt rate in June, we get an average annual melt rate is 0.71m/yr.

In the derivation above, the melt rate depends on the mixed layer velocity and salinity, which were not measured at WB, but rather taken from Robinson et al (2010). Changing the mixed layer velocity by 0.01ms^{-1} changes the estimated annual melt rate by 0.1m/yr. Changing the mixed layer salinity by 0.1psu, changes the estimated annual melt rate by 0.02m/yr. The melt rate sensitivities to other parameters are shown in Table 1. The dominant error in the above calculation comes from our lack of knowledge of the upper layer velocities.

Upper layer velocities are subject to seasonal fluctuations and change with the

tides. Mahoney et al (2011) presented velocity data measured below the sea ice at CA. These data showed seasonal changes in the upper layer ocean velocities, which caused water to flow eastward entering the ice shelf cavity during summer and to flow northwards exiting the cavity during winter. It is unclear how far under the ice shelf this current penetrates during the summer and what the current speed is by the time it reaches WB. A stronger summer current would result in an increase in the heat brought into the ice shelf cavity, and would increase the frictional velocity below the ice shelf resulting in an increased melt rate caused by the intrusion. The strong tidal velocities observed under the ice shelf by Robinson et al (2010) indicate that although the accelerated summer melt rates are caused by the intrusion of warm water, the melt rate impact of this warm water intrusion is significantly affected by the strength of the tidal signal.

While the errors in the above estimate are large, they do give us an idea of the order of magnitude of the melt rates at WB. Comparing the red curves in Fig. 4.5a and 4.5b, we see that the summer intrusion of warm water beneath the ice shelf results in seasonally accelerated summer melt rates.

The uncertainties in the melt rate calculation highlight the need for ocean temperature, salinity and velocity profiles to be collected with independent melt rate measurements, in order to confirm the use of bulk formulae beneath ice shelves. It is especially important since these bulk formulae are commonly used to find melt rates in numerical models (Holland and Jenkins, 1999). In principle, a melt rate estimate could also be derived from the ice temperature profile using inverse methods, which would provide an independent melt rate estimate.

Table 4.1: Melt rate sensitivities are shown for six different parameters. The first column shows the parameters used in the melt rate calculation. The second column shows the value of the parameters used. The third column shows the amount that the parameter is changed by in the sensitivity study. The fourth column shows the change in the annual mean melt rate as a result of changing the parameter.

Parameter	Param Value	Δ Param Value	Δ Melt
Salinity	34.5psu	0.1psu	0.02m/yr
Mixed Layer Velocity (U_M)	0.072ms^{-1}	0.01ms^{-1}	0.1m/yr
Drag Coefficient (c_d)	1.5×10^{-3}	0.1×10^{-3}	0.02m/yr
Pressure (p)	156db	10db	0.03m/yr
Stanton Number (St_*)	0.0057	0.001	0.12m/yr
Depth below ice shelf base	10m	5m	0.05m/yr

4.4 Modeling of ocean circulation and temperatures

4.4.1 Model Setup

A Ross Sea model was used to simulate the ocean dynamics in and around McMurdo Sound. The aim of the simulation was to determine the source, timing and duration of the summer warm water signal discussed above, and to determine melt rate impact of this mode 3 intrusion.

The Ross Sea circulation model used is the Rutgers/UCLA Regional Ocean Modeling System (ROMS), which is a primitive equation finite difference model with a terrain following vertical coordinate system (Haidvogel et al, 2008; Shchepetkin and McWilliams, 2009). Details of the model setup can be found in Dinniman

et al (2007) and Dinniman et al (2011), except that the dynamic sea-ice model (Budgell, 2005) that was only turned on for the Bellingshausen model in Dinniman et al (2011) is now active in the Ross Sea model. The dynamic sea-ice model (Budgell, 2005) has been added to ROMS based on ice thermodynamics described by Mellor and Kantha (1989) and Hakkinnen and Mellor (1992). The model calculates the sea-ice concentration prognostically using a two layer sea-ice representation, a snow layer and a molecular sub-layer beneath the sea ice. Further details of the sea-ice model can be found in Dinniman et al (2011). Open ocean momentum, heat and fresh water (imposed as a salt flux) fluxes for the model are calculated based on the COARE 3.0 bulk flux algorithm (Fairall et al, 2003) and there is no relaxation of surface temperature or salinity. The model also simulates the mechanical and thermodynamic interactions between the floating Ross Ice Shelf and the water cavity underneath (Holland and Jenkins, 1999; Dinniman et al, 2011).

The model domain, shown in Dinniman et al (2011) Fig. 4.1, includes most of the Ross Ice Shelf and Ross Sea, and extends north to 67.5°S. The horizontal grid spacing was 5 km and there were 24 vertical layers. The model topography is a combination of BEDMAP and a digitized version of an updated Ross Sea bathymetry from Davey (2004) (see Fig. 4.2). For this study, a model run has been completed covering the time period 9/15/2010 to 2/29/2012. This run was forced with six hourly, 0.75 degree horizontal resolution, ECMWF-Interim winds and atmospheric temperatures. The rest of the model atmospheric forcing fields (air pressure, humidity and clouds) are the same as in Dinniman et al (2007). There are no ocean tides in this model.

4.4.2 Model Results

Figure 4.6a shows the 2011 annual mean velocity field around Ross Island at 25m below the ocean surface (open ocean or below ice shelf base). In this figure, we see water entering McMurdo Sound on the east and flowing along the western coast of Ross Island. Some of the water moves under the ice shelf, while the rest recirculates and exits McMurdo Sound along the west of the sound. The velocity field is consistent with the ocean circulation in McMurdo Sound discussed in Section 2.

Figure 4.7 shows the temperature on the level 20 model surface from December 2010 to March 2011. Since the modeling surfaces are terrain following, they have different depths at different points in the domain, depending on the bottom topography and ice shelf thickness. The level 20 surface has a depth of \sim 52m below sea level in the open ocean around McMurdo Sound, and is \sim 47m below the ice shelf base close to Ross Island, and \sim 38m below the ice shelf base in the south-east Fig. 4.7. The surface does not vary by more than 20m below the ice shelf in the domain shown in Fig. 4.7.

In Fig. 4.7 we see the warm water signal entering McMurdo Sound as summer arrives and disappearing as summer comes to an end. The summer signal originates to the west of the RSP in late December. CTD profiles collected in the Ross Sea confirm that water temperatures in and to the west of the RSP can be in excess of 0.5°C in the summer months (Jacobs and Comiso, 1989; Saggiomo et

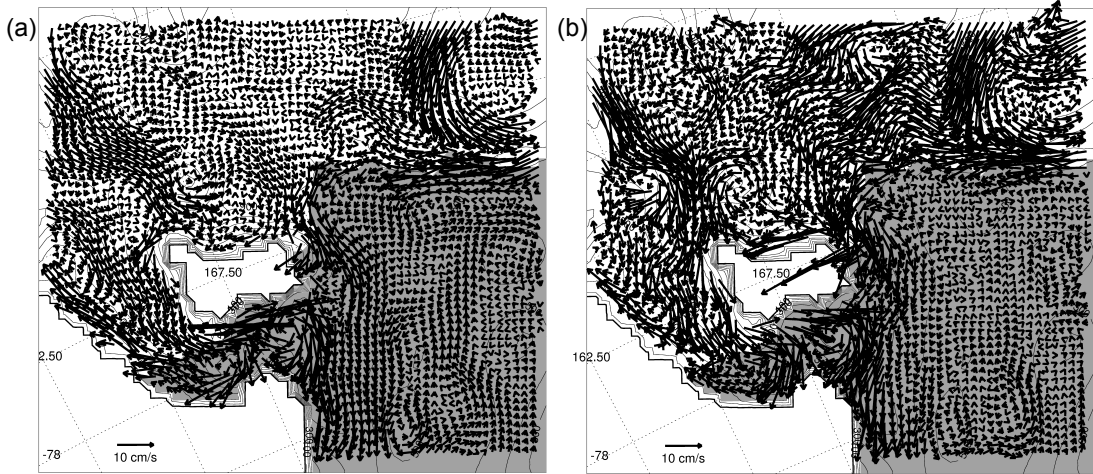


Figure 4.6: Mean model velocities around Ross Island. Panel (a) shows the annual mean velocity at 25m below the ocean surface (open ocean or below the ice shelf base). Panel (b) shows the mean surface velocity for January 2011. The summer warm current can be seen running westward along the of Ross Island in the January profile. Shaded areas represent the location of ice shelves in the model. The thick black line near the bottom of panel (a) indicates the position of the cross section shown in Fig. 4.11

al, 2002). The warm water is advected to the south-west into McMurdo Sound. It then wraps around Ross Island and moves under the McMurdo Ice Shelf towards WB. Similar summer warm water signals can be seen in all of the years simulated by the model. One other example (2003-2004 simulation) is shown in Fig. 4.8 in the supplementary material.

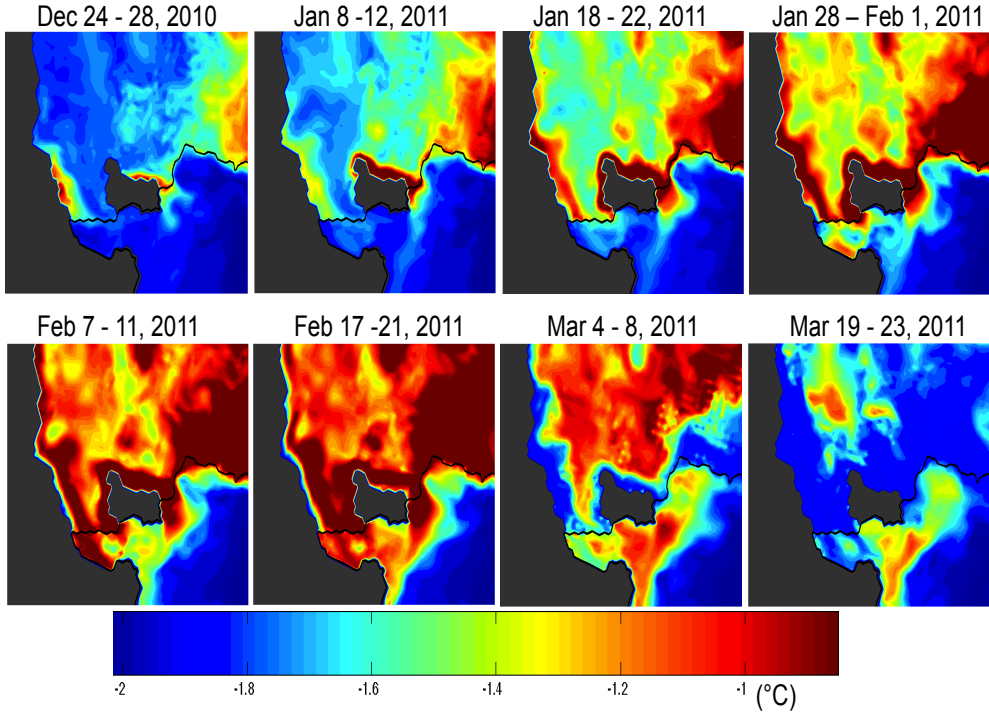


Figure 4.7: Ocean temperatures on the level 20 terrain following model surface from December 2010 to March 2011. The level 20 surface has a depth of around 52m in the open ocean, and is 48m below the ice shelf base at the grid point closest to Windless Bight. Each frame is a 5 day time average. The sequence shows the warm water signal originating to the west of the Ross Sea Polynya, being advected into McMurdo Sound and wrapping around Ross Island under the McMurdo Ice Shelf towards Windless Bight.

Figure 4.6b show the mean surface velocity field for January 2012. In Fig. 4.6b, one can see a strong surface current running westward from the west of the RSP, along the north of Ross Island and wrapping around Ross Island towards WB. This summer-time current is strongest on the surface, and decreases in strength further down in the water column. The current is not present during the winter and is less visible in the annual mean velocity field (Fig. 4.6a). Figure 4.6a also shows that there is a year round current coming from the direction of the Terra Nova Bay polynya and into McMurdo Sound. This pathway may be involved in

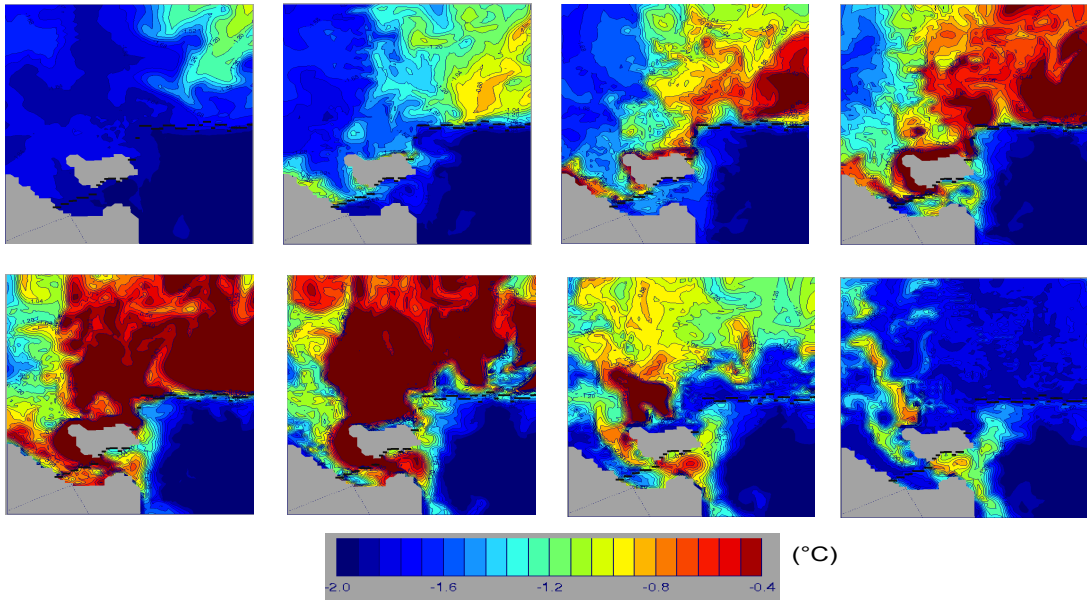


Figure 4.8: Ocean temperatures on the level 20 surface from December 2003 to March 2004. The level 20 surface has a depth of around 25m in the open ocean, and is 137m below the sea level at the grid point closest to Windless Bight. Each frame is a 5 day time average. The sequence shows the warm water signal originating to the west of the Ross Sea Polynya, being advected into McMurdo Sound and wrapping around Ross Island under the McMurdo Ice Shelf towards Windless Bight.

transporting heat into McMurdo Sound later in the summer. However, Fig. 4.7 suggests that the main source of heat at the is from the the west of the RSP.

Figure 4.5a shows the temporal evolution of the maximum temperature in the water column for three selected points: north of Ross Island (NR), west of Ross Island (WR) and WB. The position of these points are shown in Fig. 4.9. In Fig. 4.5a we again see that the warm water signal arrives first in the north in early December and makes its way around Ross Island, reaching WR next, and finally arriving to WB. Similarly, the temperature peak also occurs first at NR (0.74°C),

then at WR (0.64°C) and finally at WB (-0.44°C).

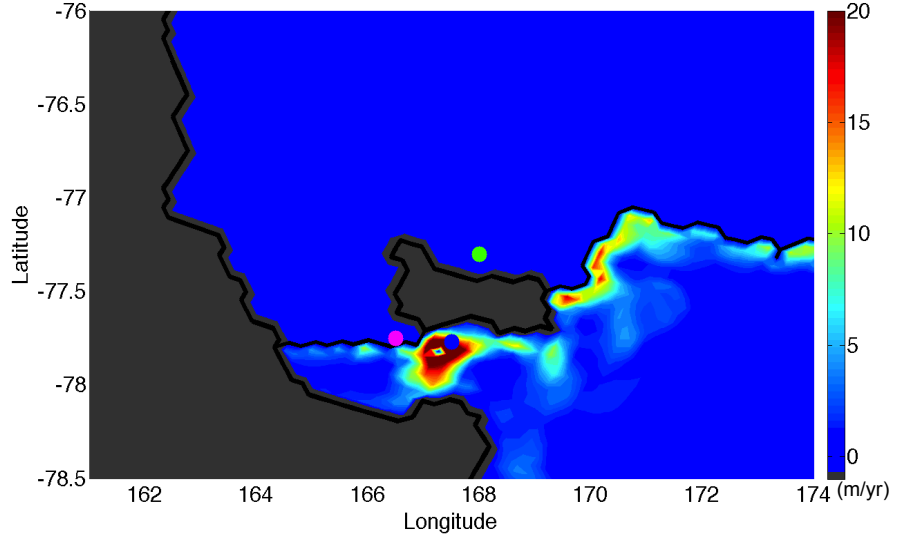


Figure 4.9: Melt rates at the base of the ice shelf in mid-February, at the peak of melting. The position of Windless Bight is shown with a blue dot. Selected points to the north (green) and west (magenta) of Ross Island are discussed in the text and in Fig. 4.5.

The temporal evolution of the model melt rate at WB is shown in Fig. 4.5b. The modeled melt rate at WB peaks on 15 February 2011. Figure 4.9 shows the melt rates under the McMurdo (and part of the Ross) Ice Shelf for mid February 2011. In these two plots we see that the summer warm water intrusion results in a large seasonal elevation in melt rates close to the ice front on the McMurdo Ice Shelf. The annual melt rate (09/15/2010 - 09/15/2011) at WB predicted by the model is 3.6m/yr, but is strongly dominated by a short but strong summer melting period. Comparing Fig. 4.9 with Fig. 4.2c, we notice that the increased melt rates are

confined to a region where the ice draft is small. Since the water intruding under the ice shelf is warm and fresh, the relatively low density of the intruding water prohibits it from penetrating deep under the ice shelf. Furthermore, as the intruding waters travel deeper under the ice shelf, the density is decreased by interaction with melt water from the base of the ice shelf. The large ice shelf draft essentially creates a shadow zone where the intruding surface waters can not penetrate.

Figure 4.10 shows the trajectory of four sets of 3D model Lagrangian floats released to the north east of Ross Island, in the location of the RSP. Each group of floats consists of ten floats that were allowed to drift for 120 days. Figures 8a, 8b and 8c show floats that were released on the level 20 model surface on 1 December 2011, 16 December 2011 and 31 December 2011, respectively. Figure 4.10d shows the trajectory of floats released at the surface on 16 December 2011.

The floats released on 1 December 2011 (Fig. 4.10a) do not appear to have a preferred drift direction. A few of the floats drift towards Ross Island making their way beneath the ice shelf to the east of Ross Island. One of the floats moves westward and makes its way into McMurdo Sound. Once this float is in McMurdo Sound, it wraps around the west of Ross Island and moves in the direction of WB. The floats released on December 16th (Fig. 4.10b) appear to move in a more organized way. All of the floats either move to the north east, or else move south west towards Ross Island. Some of these floats wrap around the east and west of Ross Island and move under the ice shelf. The floats released on 31 December 2011 move in a similar fashion except that a greater number of floats move westward along the north of Ross Island, wrap around the west of Ross Island, and move

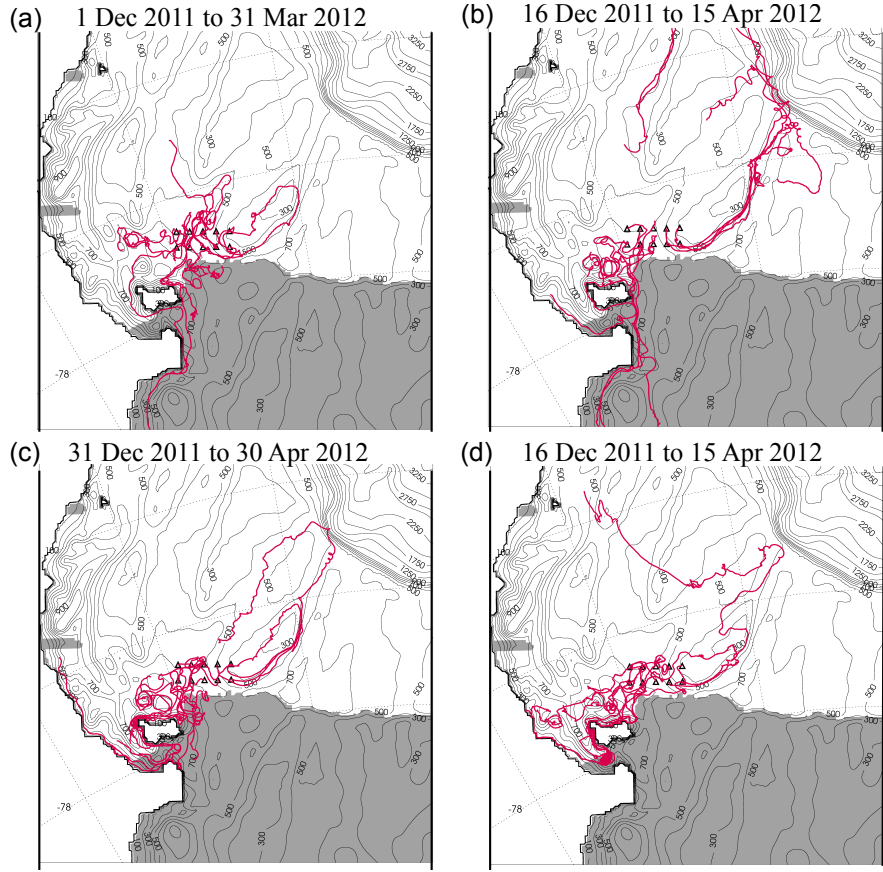


Figure 4.10: The trajectories of four groups of 3D Lagrangian model floats is shown. Each group of floats consists of ten floats which were allowed to drift for 120 days . The initial position of the floats is indicated by the black triangles. Panels (a), (b) and (c) show floats released at model level 20 on 1 Dec 2011, 16 Dec 2011 and 31 Dec 2011, respectively. Panel (d) shows floats released at the surface on 16 Dec 2011.

under the ice shelf towards WB. Figure 4.10d shows that for floats released at the surface on December 16th, an even greater number of floats follow the pathway from the RSP, around Ross Island, and under the ice shelf towards WB. Some of the floats exit the ice shelf cavity on the west of McMurdo Sound and follow the western coastline out of McMurdo Sound. A few of the deeper floats move past WB and move deeper under the ice shelf.

The float trajectories indicate that there is a summer current that moves water from the west of the RSP around the north of Ross Island and into McMurdo Sound. This current appears to be surface intensified and results in water closer to the surface being more strongly steered along this pathway. The current appears to strengthen as summer advances. This summer current is also seen in model summer mean surface velocity fields (not shown). These model results suggests that the summer warm water signal observed at WB, or at least part of it, is likely to have originated to the west of the RSP, and have followed the same path as the drifters towards WB.

The onset of the westward current leading from the RSP to McMurdo Sound is most likely caused by the melting of the sea ice in the west of the RSP. As the sea ice melts, the surface water closer to the coast becomes warmer, fresher and less dense than the water beneath the sea ice further to the north. This density difference drives a westward current, which moves water from the RSP to McMurdo Sound. The fresh surface water is decoupled from the bathymetry below, and this allows a surface intensified current to form. This generation mechanism is consistent with the model data. This mechanism is analogous to the mechanism driving a seasonal coastal current along the Antarctic Peninsula that was found by Moffat et al (2008).

Cross-sections of the salinity, potential temperature and potential density across the ice front for late January 2011 are shown in Fig. 4.11a, 4.11b and 4.11c respectively. A cross section of the potential temperature across the ice front for

late February is shown in Fig. 4.11d. Winter salinity and potential temperature sections from late September are shown in Fig. 4.11e and 4.11f. All sections in Fig. 4.11 are 5 day averages beginning on the dates indicated.

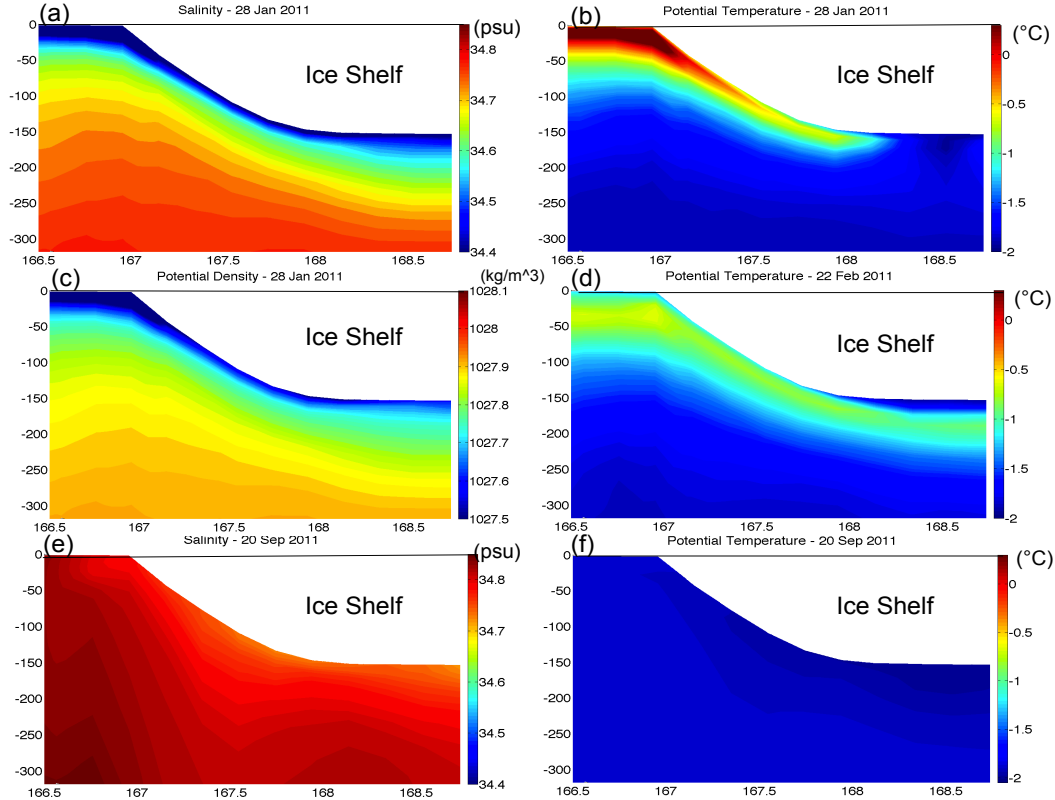


Figure 4.11: Cross sections of model results running across the ice shelf front in the south of McMurdo Sound in 2011. The position of these cross sections is shown in Fig. 4.6a. Panel (a) shows the salinity in late January 2011. Panel (b) shows the potential temperature in late January 2011. Panel (c) shows the potential density in late January 2011. Panel (d) shows the potential temperature in late February 2011. Panel (e) shows the salinity in late September 2011. Panel (f) shows the potential temperature in late September 2011. The warm near surface water at the ice front subducts under the ice shelf. The water then cools as it moves along the ice shelf base. In winter, the water column becomes homogenous. The McMurdo ice front is 20m high, which is why it appears to be so smooth (Kovacs et al, 1993; Robinson et al, 2010)

Figure 4.11 shows that the warm water moving toward WB subducts as it moves under the shelf, rather than entering the ice shelf cavity through horizontal advection (which would produce horizontal temperature contours). This implies that the intrusion is a mode 3 rather than a mode 2 intrusion. Further east on the Ross Ice Shelf, Modified Circumpolar Deep Water (MCDW) is able to move under the ice shelf at a depth of 200-400m (Dinniman et al, 2011; Orsi and Wiederwohl, 2009). This appears not to happen in McMurdo Sound. Figure 4.11 also shows that as the water subducts under the ice shelf, it cools as it travels along the ice shelf base. The heat is transmitted into the ice shelf causing melting. By late February the water at the ice shelf base is cooler than the water directly below it (Fig. 4.11d). In winter, the warm water signal disappears entirely and the water column becomes almost homogenous (Fig. 4.11e and 4.11f).

The structure of the surface intensified warm water signal indicates that a large portion of the heat entering McMurdo Sound must come from solar insolation. This result is consistent with Robinson and Williams (2012) who used CTD and mooring data to show that the warm water entering McMurdo Sound in summer was Antarctic Surface Water. Figure 4.10 shows that the intruding warm waters originate in the south west of the RSP. Observations of ocean temperature profiles in the region in the south west of the RSP show that once the sea ice has cleared, the sun is able to heat the top of the water column, creating a temperature maximum at the top of the water column (Jacobs and Comiso, 1989; Reddy et al, 2010). The warming of the surface waters in the south west of the RSP could not have occurred without the region becoming ice free because this would require another source of heat. While some heat contribution might come from MCDW (Jacobs

and Comiso, 1989; Reddy et al, 2010), most of the MCDW heat is lost when it mixes to the surface during the fall/winter. The temperature maximum at the surface could not have been created by upwelling of MCDW alone since this would create a temperature maximum lower down in the water column.

Since the source of the heat for the warm water intrusion is through solar insulation in the south west of the RSP, the arrival of the warm water intrusion can not occur until the RSP becomes ice free. The time of this arrival varies slightly from year to year because of inter-annual variability in the sea-ice conditions (Martin et al, 2007; Robinson and Williams, 2012). One example of this was in 2003, when the presence of large icebergs resulted in a late opening of the RSP, which had a significant effect on the temperatures measured in McMurdo Sound (Robinson and Williams, 2012).

Figure 4.4b shows how the ocean profile at WB in the model varies with time. In this figure we see the annual arrival of warm water and the vertical structure of this warm water signal.

4.4.3 Model Sea-Ice Conditions

The above results imply that the timing of the warm water intrusion depends on the timing of the opening of the RSP. It is therefore important that our model should be able to correctly simulate the sea-ice conditions over the Ross Sea if we hope for the timing of the model intrusion to match the observed intrusion. Recall that our model includes a dynamic sea-ice model (Budgell, 2005).

The model sea-ice results compare well to sea-ice satellite observations. The integrated sea-ice area over the entire domain and over the continental shelf are used to quantify the comparison between the model results and the Special Sensor Microwave Imager/Sounder (SSMIS) sea-ice satellite observations (Maslanik and Stroeve, 1999). The model output and satellite observations have a correlation of $r = 0.956$ over the entire model domain and $r = 0.946$ over the continental shelf. This high correlation indicates that the model does a good job of representing the timing of seasonal changes in the ice concentration and the opening of the RSP.

Figure 4.12 shows how the integrated sea-ice area over the entire domain and over the continental shelf vary with time. The model is slow to first open up the polynya compared with SSMIS, and has a consistent lag during the period when the sea-ice area is decreasing. The model does a good job simulating the timing and area of the summer time sea-ice minimum across the entire domain and on the continental shelf. The timing of the ice coming back in the fall is also well reproduced. The model has too much sea ice at the time of maximum sea-ice extent. The spatial structure of the RSP (not shown) also compares well with observations.

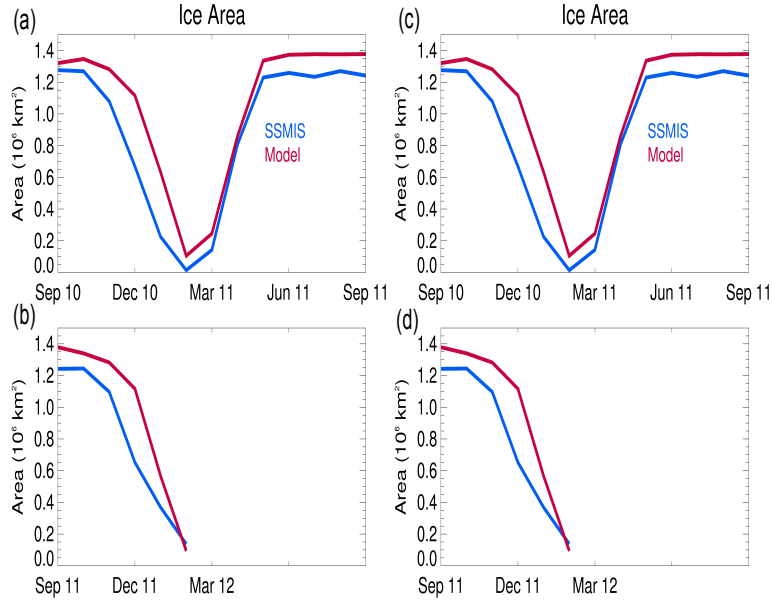


Figure 4.12: Integrated sea-ice cover over the Ross Sea (panels (a) and (b)) and over the Ross Sea continental shelf (panels (c) and (d)). Model results are shown in red and SSMIS satellite observations are shown in blue.

4.5 Discussion

4.5.1 Comparing Observations with Model Results

The maximum ocean temperature recorded at WB occurred on March 7, 2012 and was -1.19°C . This is considerably cooler than the temperature maximum observed in previous campaigns by moorings under the sea ice (-0.08°C at CA in late January 2008 (Mahoney et al, 2011); -0.43°C in mid January 2000 and -0.65°C in early February 2001 at MIJ (Hunt et al, 2003)). This is consistent with the model results that showed subduction and cooling of the warm water as it moved under the ice shelf (Fig. 4.5). The temperature maximum also arrives substantially later at WB than it had under the sea ice in any of measurements from previous years. The maximum modeled ocean temperature recorded at WB in 2011 occurred on

February 25th, 2011.

The modeling results and the newly acquired observations provide further evidence that the warm water summer signal seen below the sea ice by Mahoney et al (2011) and Hunt et al (2003) at CA is a regular annual signal, and that it is advected from north east of Ross Island into McMurdo Sound. Furthermore, the results confirm that the warm water signal does manage to propagate below the McMurdo Ice Shelf and eventually arrives at WB, where it causes elevated melt rates during the summer.

Comparing the modeled temperature profile at WB (Fig. 4.4b) to the observed temperature profile at WB (Fig. 4.4a), we see that the model captures many of the features seen in the observational data. Both the model and observations at WB show the arrival of the summer warm water signal in January. The initial warm water signal occurs in the upper portion of the water column close to the base of the ice shelf. During February the intrusion becomes stronger and extends deeper in the water column. The highest temperatures are found at the top of the water column, close to the base of the ice shelf. The summer signal peaks at the end of summer, with maximum temperatures occurring in late February (model) and early March (observations). In the fall, the temperatures decrease and by June, the water column is almost isothermal. During the fall there is a temperature inversion in the water column in both the model and observations. The ocean temperatures just below the ice shelf cool fastest, which results in the water column having cooler water temperatures at the top of the water column and warmer temperatures just below. The lower portion of the water column is

largely unaffected by the warm water intrusion, and remains at $\sim -1.9^{\circ}\text{C}$ throughout the observed period. The warm water signal observed at WB is cooler than the signal predicted by the model. The observed signal persists longer than the modeled warm water signal and is confined more tightly to the upper layer. The model warm water signal from 2011 arrives two weeks earlier than the signal in the observations from 2012.

The model predicted an annual average melt rate of 3.6m/yr at WB, which was higher than the annual average melt rate estimated from the observed ocean temperatures (0.71m/yr). One reason for this was that the modeled temperature of the warm water intrusion at WB was up to $\sim 1^{\circ}\text{C}$ warmer than the observed temperatures. Examining the modeled melt rate data more carefully (Fig. 4.10), we notice that WB is in a region that has a steep gradient in the melt rates since it is right on the edge of a high melting zone. The three model points immediately to the east of WB have annual melt rates of 2.9, 1.5 and 0.6 m/yr. These large spatial gradients in the melt rate are a result of similar large spatial gradients in the bathymetry data around WB (since the warmest water is steered by the bathymetry). The resolution and accuracy of the bathymetry data used in the model is another likely source of error in determining the ultimate melt rates.

The fact that the model is able to reproduce the summer water intrusion under McMurdo ice shelf without including the complex topography around Ross Island and without including tides, indicates that the local oceanography under the McMurdo Ice Shelf is strongly controlled by the larger circulation in the Ross Sea. The calculation for the melt rate estimate shown in Section 3.3 indicates that

tidal currents may be significant for determining the basal melting caused by this intrusion.

The annual melt rate is heavily dominated by a short period of extreme melting. This implies that attempting to predict this melt rate using a model will be sensitive to the strength and duration of the warming period. Since these both depend on sea-ice conditions further north, it is likely to be a difficult problem, and a source of inaccuracy for coupled models that do not use prescribed sea-ice concentrations. This difficulty is likely to be common to most mode 3 warm water intrusions.

The modeling results shown above indicate that the RSP is the source of the warm water signal observed beneath the McMurdo ice shelf. This result suggests that mode three intrusions may be associated with the opening of the polynyas in other regions in Antarctica. Hattermann et al (2012) observed a mode 3 intrusion of warm water near the ice front beneath the Fimbul Ice Shelf. This intrusion occurred in late summer and was associated with the ocean near the ice front becoming ice free (Hattermann et al, 2012). Further observations and modeling efforts are needed to determine whether there are further examples of this phenomenon.

4.6 Conclusion

High resolution, semi-annual ocean temperature profiles measured at WB on the McMurdo Ice Shelf from November 2011 to June 2012 reveal a warm water

summer signal that penetrates under the McMurdo Ice Shelf and results in increased melting. A regional Ross Sea ocean model is used to simulate the mode 3 summer intrusion. Model results are compared with observations of temperatures below the sea-ice and ice shelf south of Ross Island. The results presented above shed light on the source, timing and melt rate impact of the warm water intrusion.

The model shows that the warm water signal seen at WB originates in the region to the north-east of Ross island, west of the Ross Sea Polynya. Once the sea ice in this region has cleared, the Sun heats the ocean surface, which causes warming in the upper part of the ocean. The warm water is transported into McMurdo Sound by ocean currents, where some of the water subducts under the ice shelf and is able to wrap around Ross Island towards Windless Bight. As the intruding water moves along the ice shelf base, it is cooled due to glacier ice melting, eventually resulting in a temperature inversion. The warm water under the ice shelf results in seasonally accelerated melt rates. The extent of the melt rate impact is strongly controlled by bathymetry.

The model was able to simulate the structure of the temporal evolution of the ocean temperature profile at Windless Bight. The maximum model temperatures achieved were $\sim 1^{\circ}\text{C}$ higher than those observed, resulting in a melt rate that was higher than the melt rate inferred from ocean temperature observations. This highlights the sensitivity of the melt rates caused by mode 3 intrusions to the strength and duration of the intrusion and also to the accuracy of bathymetry data used. The elevated melt rates occurring for short periods of time, implies that predicting the total contribution of mode 3 intrusions on the melt rates of

Antarctic ice shelves is likely to present a challenge to numerical models.

This study presents one of the first successful incorporations of high spatial and temporal resolution data from fiber optic sensing in an ice shelf, which could be an exciting new measurement technique for polar regions. The above findings provide motivation for the establishment of a wide network of ice shelf monitoring stations which can be used to constrain and validate numerical models on a larger scale.

Chapter 5

Conclusion

5.1 Summary

The work above describes three mechanisms which are responsible for transporting heat beneath the Antarctic ice shelves. The thesis uses the framework of the three modes of warm water intrusion outlined in Jacobs et al (1992). In the chapters above, we describe the three modes and discuss how each of these three modes is responsible for transporting heat towards the Antarctic ice shelves. Understanding the dynamics which control the warm water intrusions beneath the Antarctic ice shelves is critical to projecting the melt rates beneath the Antarctic ice shelves, and hence to projecting future sea level.

Chapter 2 describes the Mode 1 warm water intrusion. In Chapter 2, we use a laboratory experiment to explore the density driven circulation beneath the large Antarctic ice shelves. The study focusses on how changes in the ice shelf geometry can affect the circulation inside the ice shelf cavity, and the strength of the

dynamical barrier caused by the presence of the ice shelf.

Chapter 3 focusses on Mode 2 warm water intrusions. In the Amundsen and Bellingshausen Seas, Circumpolar Deep Water crosses the continental shelf break and causes accelerated melting beneath the adjacent ice shelves. Chapter 3 discusses the dynamics which control this cross shelf exchange. In particular, we describe how instabilities of ocean jets which form over the continental shelf break can lead to enhanced cross shelf mixing.

Lastly, Chapter 4 looks an example of a seasonal Mode 3 warm water intrusion. In this chapter we describe how warm surface water subducts beneath the McMurdo Ice Shelf during the summer. We consider the timing, pathway and melt rate impact of this warm water intrusion. Model results are compared to observations made beneath the McMurdo Ice Shelf collected using a Distributed Temperature Sensing fiber optic thermistor.

5.2 Future work:

The work above makes some progress in understanding the dynamics of the water beneath and around the Antarctic ice shelves. However there is still much more work to be done. In this section we briefly discuss some of the immediate questions which need to be addressed.

In this thesis, the three modes of melting are discussed separately. However, it

is expected that the three modes should interact with one another. The question of how these three modes interact with one another is likely to be an important question in the coming years.

A related question is how these three modes are affected by atmospheric forcing. It is important for us to understand the response of polar oceans to changing atmospheric forcings since this will help us to understand how melt rates are likely to be affected by changing climates? Another important question is how well are these three modes of warm water intrusions represented in global climate models. Can these modes be accurately simulated when the grid scale of the climate models is large, or do these heat transfer mechanisms need to be parasitized in some way?

The results in Chapter 3 suggest that there might be a shelf break jet which forms over the continental shelf break in the Bellingshausen Sea, and that this jet drifts away from the shelf break aperiodically. Since the drifting jets and low frequency variability are seen in both in the quasi geostrophic simulations and in primitive equation simulations, it is likely that these features can be observed in the real ocean. The next step which needs to be taken is to see if these jets can be seen in real-world observations and complex climate models. A starting point for this is to see if the shelf break jet can be detected using satellite observations of sea surface height.

Lastly, there are many observational challenges which need to be overcome if we hope to get a more complete understanding of processes beneath the Antarctic ice shelves. One goal in the coming years will be to establish a permanent net-

work of ocean temperature and salinity sensors to make measurements below the ice shelves. This will help us to monitor trends in the melt rates beneath the Antarctic ice shelves.

Bibliography

- ADRIAN R. J. (2005) Twenty years of particle image velocimetry. *Experiments in Fluids.*, **39(2)**, 159-169.
- M. rthun, Nicholls, K.W and Boehme, L. (2013): Wintertime Water Mass Modification near an Antarctic Ice Front. *J. Phys. Oceanogr.*, 43, 359365. doi: <http://dx.doi.org/10.1175/JPO-D-12-0186.1>
- Assmann, K. , Hellmer, H. and Beckmann, A. (2003): Seasonal variation in circulation and water mass distribution on the Ross Sea continental shelf, *Antarctic Science*, **15 (1)**, pp. 3-11, doi: 10.1017/S0954102003001007
- Beardsley, R.C., and C.N. Flagg. 1976, The water structure, mean currents, and shelf-water/slope-water front on the New England continental shelf. *Mem. Soc. Roy. Sci.*, Liege 6, 209-225.
- Benilov, E. S., 2001: Baroclinic Instability of Two-Layer Flows over One-Dimensional Bottom Topography. *J. Phys. Oceanogr.*, 31, 20192025.
- Boland, Emma J. D., Andrew F. Thompson, Emily Shuckburgh, Peter H. Haynes, 2012: The Formation of Nonzonal Jets over Sloped Topography. *J. Phys. Oceanogr.*, 42, 16351651.

- Bindschadler, R., D.G. Vaughan, P. Vornberger (2011), Variability of basal melt beneath the Pine Island Glacier ice shelf, West Antarctica. *J. of Glaciol.*, 57 (204), 581-595.
- Budgell, W. P. (2005), Numerical simulation of ice-ocean variability in the Barents Sea region: Towards dynamical downscaling, *Ocean Dynamics*, 55, 3-4, 370-387.
- CENEDESE C., WHITEHEAD J. A., ASCARELLI T. A, OHIWA M. (2004) A dense current flowing down a sloping bottom in a rotating fluid. *J. Phys. Oceanogr.*, **34**, 188-203.
- Changheng Chen, Igor Kamenkovich. (2013) Effects of Topography on Baroclinic Instability. *Journal of Physical Oceanography* 43:4, 790-804
- CONWAY, H., B. L. HALL, G. H. DENTON, A. M. GADES, AND E. D. WADDINGTON. (1999), Past and future grounding-line retreat of the West Antarctic ice sheet. *Science* 286, no. 5438 (1999): 280-283.
- COSSU R., M. G. WELLS WHLIN A. K. (2004) Influence of the Coriolis force on the velocity structure of gravity currents in straight submarine channel systems. *J. Geophys. Res.*, **115**, C11016, doi:10.1029/2010JC006208..
- Davey, F.J. (2004), Ross Sea Bathymetry, 1:2,000,000, Version 1.0, Institute of Geological & Nuclear Sciences Geophysical Map 16. Institute of Geological & Nuclear Sciences Limited, Lower Hutt, New Zealand.
- DETERMAN J., GERDES R. (1994) MELTING AND FREEZING BENEATH ICE SHELVES: IMPLICATIONS FROM A THREE-DIMENSIONAL OCEAN-CIRCULATION MODEL. *Ann. Glaciol.*, **20**, 413-419.

DINNIMAN, M. S., J. M. KLINCK, AND W. O. SMITH JR., 2003: CROSS-SHELF EXCHANGE IN A MODEL OF THE ROSS SEA CIRCULATION AND BIOGEOCHEMISTRY. *Deep-Sea Res.*, 50, 31033120, doi:10.1016/J.DSR2.2003.07.011.

DINNIMAN, M. S. AND J. M. KLINCK, 2004: A MODEL STUDY OF CIRCULATION AND CROSS-SHELF EXCHANGE ON THE WEST ANTARCTIC PENINSULA CONTINENTAL SHELF. *Deep-Sea Res.*, 51, 20032022, doi:10.1016/J.DSR2.2004.07.030.

DINNIMAN, M.S., KLINCK, J.M., SMITH JR., W.O. (2007), THE INFLUENCE OF SEA ICE COVER AND ICEBERGS ON CIRCULATION AND WATER MASS FORMATION IN A NUMERICAL CIRCULATION MODEL OF THE ROSS SEA, ANTARCTICA. *Journal of Geophysical Research*, 112, C11013. doi:10.1029/2006JC004036

DINNIMAN, M.S., J.M. KLINCK AND W.O. SMITH, JR. (2011), A MODEL STUDY OF CIRCUMPOLAR DEEP WATER ON THE WEST ANTARCTIC PENINSULA AND ROSS SEA CONTINENTAL SHELVES. *Deep-Sea Research II*, 58, 1508-1523, doi:10.1016/J.DSR2.2010.11.013.

DINNIMAN, M.S., J.M. KLINCK AND E.E. HOFMANN (2012), SENSITIVITY OF CIRCUMPOLAR DEEP WATER TRANSPORT AND ICE SHELF BASAL MELT ALONG THE WEST ANTARCTIC PENINSULA TO CHANGES IN THE WINDS *J. of Clim.*, 58, 4799-4816, DOI: 10.1175/JCLI-D-11-00307.1

DRITSCHEL, D. G., M. E. MCINTYRE, 2008: MULTIPLE JETS AS PV STAIRCASES: THE PHILLIPS EFFECT AND THE RESILIENCE OF EDDY-TRANSPORT BARRIERS. *J. Atmos. Sci.*, 65, 855874.

- ETLING D., GELHARDT F., SCHRADER U., BRENNCKE F., KUHN G., CHABERT DHIERES G., DIDELLE H. (2000) EXPERIMENTS WITH DENSITY CURRENTS ON A SLOPING BOTTOM IN A ROTATING FLUID. *Dynamics of Atmospheres and Oceans*, **31**, 139-164.
- FAIRALL, C. W., E. F. BRADLEY, J. E. HARE, A. A. GRACHEV, AND J. B. EDSON (2003), BULK PARAMETERIZATION OF AIRSEA FLUXES: UPDATES AND VERIFICATION FOR THE COARE ALGORITHM. *J. Climate*, **16**, 571-591.
- FARRELL, B. F. AND P. J. IOANNOU, 2003: STRUCTURAL STABILITY OF TURBULENT JETS. *J. Atmos. Sci.*, **50**, 21012118.
- FOLDVIK A., GAMMELSRØD T., NYGAARD E., OSTERHUS, S. (1983) CURRENT MEASUREMENTS NEAR RONNE ICE SHELF: IMPLICATIONS FOR CIRCULATION AND MELTING. *J. Geophys. Res.* **106**, 4463-4477..
- GILLE, S. T. (1994), MEAN SEA SURFACE HEIGHT OF THE ANTARCTIC CIRUMPOLAR CURRENT FROM GEOSAT DATA: METHOD AND APPLICATION, *J. Geophys. Res.*, **99**(C9), 1825518273, doi:10.1029/94JC01172
- GORDON, A. L., ORSI, A. H., MUENCH, R., HUBER, B. A., ZAMBIANCHI, E., AND VISBECK, M., (2009), WESTERN ROSS SEA CONTINENTAL SLOPE GRAVITY CURRENTS, *Deep-Sea Res. Pt. II*, **56**, 796817, 20 doi:10.1016/j.dsr2.2008.10.037.
- GREENSPAN H.P., HOWARD L.N. (1963) ON A TIME-DEPENDENT MOTION OF A ROTATING FLUID . *J. Fluid Mech.* **17**, 385.
- GRIFFITHS, R.W. (1986) GRAVITY CURRENTS IN ROTATING SYSTEMS. *Ann. Rev. Fluid Mech.*, **18**, 59-89.

GRIFFITHS, R. W., HOPFINGER E. J. (1983) GRAVITY CURRENTS MOVING ALONG A LATERAL BOUNDARY IN A ROTATING FRAME. *J. Fluid Mech.* **134**, 357-399..

GROSFELD K., GERDES R., DETERMAN J. (1997) THERMOHALINE CIRCULATION AND INTERACTION BETWEEN ICE SHELF CAVITIES AND THE ADJACENT OPEN OCEAN. *J. Phys. Oceanogr.*, **102**, C7, 15959-15610.

HAIDVOGEL, D.B., H. ARANGO, W.P. BUDGELL, B.D. CORNUELLE, E. CURCHITSER, E. DI LORENZO, K. FENNEL, W.R. GEYER, A.M. HERMANN, L. LANEROLLE, J. LEVIN, J.C. MCWILLIAMS, A.J. MILLER, A.M. MOORE, T.M. POWELL, A.F. SCHEPETKIN, C.R. SHERWOOD, R.P. SIGNELL, J.C. WARNER, AND J. WILKIN (2008), OCEAN FORECASTING IN TERRAIN FOLLOWING COORDINATES: FORMULATION AND SKILL ASSESSMENT OF THE REGIONAL OCEAN MODELING SYSTEM, *J. Comput. Phys.*, 227, 3595-3624, doi:10.1016/j.jcp.2007.06.016.

HAKKINEN, S., G.L. MELLOR (1992), MODELING THE SEASONAL VARIABILITY OF A COUPLED ARCTIC ICE-OCEAN SYSTEM, *J. Geophys. Res.*, 97, 20285-20304.

HATTERMANN, T., O. A. NOST, J. M. LILLY, AND L. H. SMEDSRUD (2012), TWO YEARS OF OCEANIC OBSERVATIONS BELOW THE FIMBUL ICE SHELF, ANTARCTICA. *Geophysical Research Letters*, 39, L12605: 16, doi:10.1029/2012GL051012.

HELLMER H.H., OLBERS D. J. (1989) A TWO-DIMENSIONAL MODEL FOR THE

THERMOHALINE CIRCULATION UNDER AN ICE SHELF. *Antarctic Science*, **1**, 325- 336.

HOLLAND, D.M., AND A. JENKINS (1999), MODELING THERMODYNAMIC ICE-OCEAN INTERACTIONS AT THE BASE OF AN ICE SHELF. *J. Phys. Oceanogr.*, **29**, 1787-1800.

HOLLAND D. M., JENKINS A. (2001) ADAPTATION OF AN ISOPYCNIC CO-ORDINATE OCEAN MODEL FOR THE STUDY OF CIRCULATION BENEATH ICE SHELVES. *Mon. Wea. Rev.*, **129**, 1905-1927.

HOLLAND, D.M., S.S. JACOBS, AND A. JENKINS (2003), MODELING ROSS SEA ICE SHELF - OCEAN INTERACTION, *Antarctic Sci.*, **15**, 13-23.

HOLLAND P. R., FELTHAM D. L. (2006) THE EFFECTS OF ROTATION AND ICE SHELF TOPOGRAPHY ON FRAZIL-LADEN ICE SHELF WATER PLUMES. *J. Phys. Oceanogr.*, **36**, 2312-2327.

HOLLAND P. R., JENKINS A., HOLLAND D. M (2008) THE RESPONSE OF ICE SHELF BASAL MELTING TO VARIATIONS IN OCEAN TEMPERATURE. *J. Climate*, **15**, 2558-2572.

HOLMAN, J. P. (2002). HEAT TRANSFER. McGRAW-HILL. p. 207.

HOUCINE I., VIVIER J. M., PLASARI J. M., VILLERMAUX J. M. (1996) PLANAR LASER INDUCED FLUORESCENCE TECHNIQUE FOR MEASUREMENTS OF CONCENTRATION FIELDS IN CONTINUOUS STIRRED TANK REACTORS. *Exp. Fluids*, **22**, 95-10.

HOOKE, R. L. (2005), PRINCIPLES OF GLACIER MECHANICS, SECOND EDITION, XIV PP, CAMBRIDGE UNIVERSITY PRESS, UK

HORGAN, H. J., R. T. WALKER, S. ANANDAKRISHNAN, AND R. B. ALLEY (2011), SURFACE ELEVATION CHANGES AT THE FRONT OF THE ROSS ICE SHELF: IMPLICATIONS FOR BASAL MELTING, *J. Geophys. Res.*, 116, C02005, doi:10.1029/2010JC006192.

HUNT, B.M., K. HOEFLING AND C. C. CHENG (2003), ANNUAL WARMING EPISODES IN SEAWATER TEMPERATURES IN McMURDO SOUND IN RELATIONSHIP TO ENDOGENOUS ICE IN NOTOTHENIOID FISH, *Antarctic Science*, 15 , PP 333-338 doi:10.1017/S0954102003001342.

HUTHNANCE, J. 1995: CIRCULATION, EXCHANGE AND WATER MASSES AT THE OCEAN MARGIN: THE ROLE OF PHYSICAL PROCESSES AT THE SHELF EDGE. *Prog. Oceanogr.*, VOL. 35. PP. 353-431

JACOBS, S. S. AND J. C. COMISO (1989) SEA ICE AND OCEANIC PROCESSES ON THE ROSS SEA CONTINENTAL-SHELF. *J. of Geophys. Research-Oceans*, 94(C12): 18195-18211.

JACOBS, S.S. 1991: ON THE NATURE AND SIGNIFICANCE OF THE ANTARCTIC SLOPE FRONT. *Marine Chemistry*., VOL.35, PP.924.

JACOBS S.S., H.H. HELMER, C.S.M. DOAKE, A. JENKINS AND R.M. FROLICH (1992), MELTING OF ICE SHELVES AND THE MASS BALANCE OF ANTARCTICA. *J. of Glaciol.*, 38 (130): 375-387.

JACOBS, S.S., A. JENKINS, C.F. GIULIVI AND P. DUTRIEUX (2011), STRONGER OCEAN CIRCULATION AND INCREASED MELTING UNDER

PINE ISLAND GLACIER ICE SHELF. *Nature Geoscience*, 4, 519-523,
doi:10.1038/NGEO1188.

JENKINS, A. (1991) A ONE-DIMENSIONAL MODEL OF ICE SHELF-OCEAN INTERACTION. *J. Geophys. Res. -Oceans*, 96, C11, 20671-20677.

JENKINS, A., VAUGHAN, D. G., JACOBS, S. S., HELLMER, H. H. AND KEYS, J. R., 1997: GLACIOLOGICAL AND OCEANOGRAPHIC EVIDENCE OF HIGH MELT RATES BENEATH PINE ISLAND GLACIER, WEST ANTARCTICA. *J. Glaciol.*, 43, 114121

JENKINS, A., K. W. NICHOLLS, AND H. F. CORR (2010), OBSERVATION AND PARAMETERIZATION OF ABLATION AT THE BASE OF RONNE ICE SHELF, ANTARCTICA. *J. Phys. Oceanogr*, 40(10), 2298-2312.

JOHNSON, G. C., AND H. L. BRYDEN, 1989: ON THE SIZE OF THE ANTARCTIC CIRCUMPOLAR CURRENT. *Deep-Sea Res.*, 36, 3953.

JOUGHIN, I. AND R. ALLEY (2011), STABILITY OF THE WEST ANTARCTIC ICE SHEET IN A WARMING WORLD, *Nature Geoscience*, 4, 506513, doi:10.1038/NGEO1194

JENKINS A., DUTRIEUX P., JACOBS S., MCPHAIL S., PERRETT J., WEBB A., WHITE D. (2012) AUTONOMOUS UNDERWATER VEHICLE EXPLORATION OF THE OCEAN CAVITY BENEATH AN ANTARCTIC ICE SHELF. *Oceanography* 25(3):202203, [HTTP://DX.DOI.ORG/10.5670/OCEANOOG.2012.95](http://dx.doi.org/10.5670/oceanog.2012.95).

KILLWORTH O.D., PALDOR N., STERN M.E. (1984) WAVE PROPAGATION AND GROWTH ON A SURFACE FRONT IN A TWO-LAYER GEOSTROPHIC CURRENT. *J. Marine Res.*, 42, 761-785.

KOMAR, P. D. (1969) THE CHANNELIZED FLOW OF TURBIDITY CURRENTS WITH APPLICATION TO MONTEREY DEEP?SEA FAN CHANNEL. *J. Geophys. Res.*, **74**, 45444558, doi:10.1029/JC074i018p04544.

KOVACS, A., A.J. GOW AND R.M. MOREY (1993), A REASSESSMENT OF THE IN-SITU DIELECTRIC CONSTANT OF POLAR FIRN. *Cold Regions Research & Engineering Laboratory Report*, 93-26.

G. LANE-SERFF, BAINES, P. (1998) EDDY FORMATION BY DENSE FLOWS ON SLOPES IN A ROTATING FLUID. *J. Fluid Mech.*, **363**, pp. 229252.

LARGE, W. G., J. C. MCWILLIAMS, AND S. C. DONEY, 1994: OCEANIC VERTICAL MIXING: A REVIEW AND A MODEL WITH A NONLOCAL BOUNDARY LAYER PARAMETERIZATION. *Rev. Geophys.*, **32**, 363-403.

LEONARD, G. H., C. R. PURDIE, P. J. LANGHORNE, T. G. HASKELL, M. J. M. WILLIAMS, AND R. D. FREW (2006), OBSERVATIONS OF PLATELET ICE GROWTH AND OCEANOGRAPHIC CONDITIONS DURING THE WINTER OF 2003 IN McMURDO SOUND, ANTARCTICA, *J. Geophys. Res.*, **111**, C04012, doi:10.1029/2005JC002952.

LEWIS, E.L. AND R.G. PERKIN (1985), THE WINTER OCEANOGRAPHY OF McMURDO SOUND, ANTARCTICA. *Antarctic Research Series*, **43**, 145-166.

LINDER, C. A., AND G. GAWARKIEWICZ, 1998 , A CLIMATOLOGY OF THE SHELFBREAK FRONT IN THE MIDDLE ATLANTIC BIGHT, *J. Geophys. Res.*, **103(C9)**, 1840518423, doi:10.1029/98JC01438.

LITTLEPAGE, J.L. (1965), OCEANOGRAPHIC INVESTIGATIONS IN McMURDO SOUND, ANTARCTICA. *Antarctic Research Series*, **5**, 1-37.

LOZIER, M. SUSAN, MARK S. C. REED, GLEN G. GAWARKIEWICZ,
2002: INSTABILITY OF A SHELFBREAK FRONT. *J. Phys.*
OCEANOGR., 32, 924944. DOI: [HTTP://DX.DOI.ORG/10.1175/1520-0485\(2002\)032<0924:IOASF>2.0.CO;2](http://dx.doi.org/10.1175/1520-0485(2002)032<0924:IOASF>2.0.CO;2)

MACAYEAL, D. R. (1984), THERMOHALINE CIRCULATION BELOW THE ROSS ICE SHELF: A CONSEQUENCE OF TIDALLY INDUCED VERTICAL MIXING AND BASAL MELTING, *J. Geophys. Res.*, 89(C1), 597-606, DOI:10.1029/JC089iC01p00597.

MACAYEAL D.R. (1985) EVOLUTION OF TIDALLY TRIGGERED MELTWATER PLUMES BELOW ICE SHELVES, IN OCEANOLOGY OF THE ANTARCTIC CONTINENTAL SHELF (ED S. S. JACOBS). *American Geophysical Union*, WASHINGTON, D. C.. DOI: 10.1029/AR043P0133.

MAKINSON K., SCHRÖDER M., ØSTERHUS S. (2005) SEASONAL STRATIFICATION AND TIDAL CURRENT PROFILES ALONG RONNE ICE FRONT. *Frisp Report*, 16.

MAKINSON, K., M. SCHRDER, AND S. STERHUS (2006), EFFECT OF CRITICAL LATITUDE AND SEASONAL STRATIFICATION ON TIDAL CURRENT PROFILES ALONG RONNE ICE FRONT, ANTARCTICA, *J. Geophys. Res.*, 111, C03022, DOI:10.1029/2005JC003062.

MAKINSON K., HOLLAND P.R., JENKINS A., NICHOLLS K.W., HOLLAND D.M. (2011) INFLUENCE OF TIDES ON MELTING AND FREEZING BENEATH FILCHNER-RONNE ICE SHELF, ANTARCTICA. *Geophys. Res. Letters*, 113, C08043.

MAHONEY, A. R., A. J. GOUGH, P. J. LANGHORNE, N. J. ROBINSON, C. L. STEVENS, M. M. J. WILLIAMS, AND T. G. HASKELL (2011), THE SEASONAL APPEARANCE OF ICE SHELF WATER IN COASTAL ANTARCTICA AND ITS EFFECT ON SEA ICE GROWTH, *J. Geophys. Res.*, 116, C11032, doi:10.1029/2011JC007060.

MARSHALL, J., ADCROFT, A., HILL, C., PERELMAN, L., HEISEY, C., 1997A. A NITE-VOLUME, INCOMPRESSIBLE NAVIER STOKES MODEL FOR STUDIES OF THE OCEAN ON PARALLEL COMPUTERS. *J. Geophys. Res.*, 102 (C3), 57535766.

MARSHALL, J., HILL, C., PERELMAN, L., ADCROFT, A., 1997B. HYDROSTATIC, QUASI-HYDROSTATIC, AND NONHYDROSTATIC OCEAN MODELING. *J. Geophys. Res.*, 102 (C3), 57335752

MARSHALL, J., AND T. RADKO, 2003: RESIDUAL-MEAN SOLUTIONS FOR THE ANTARCTIC CIRCUMPOLAR CURRENT AND ITS ASSOCIATED OVERTURNING CIRCULATION. *J. Phys. Oceanogr.*, 33, 23412354.

MARSHALL J., PLUMB R.A. (2008) ATMOSPHERE, OCEAN AND CLIMATE DYNAMICS. page 123 -128.

MARTIN, S., R. DRUCKER, AND R. KWOK (2007), THE AREAS AND ICE PRODUCTION OF THE WESTERN AND CENTRAL ROSS SEA POLYNYAS, 19912002, AND THEIR RELATION TO THE B-15 AND C-19 ICEBERG EVENTS OF 2000 AND 2002. *J. of Maine Systems.*, 68, 201-214, <HTTP://DX.DOI.ORG/10.1016/J.JMARSYS.2006.11.008>

MASLANKI, J., AND J. STROEVE (1999), NEAR-REAL-TIME DMSP SSM/I-SSMIS DAILY POLAR GRIDDED SEA ICE CONCENTRATIONS, 15 SEPT. 2010 TO 29 FEB. 2012. BOULDER, COLORADO USA: NATIONAL SNOW AND ICE DATA CENTER. DIGITAL MEDIA.

MATHIOT P., JOURDAIN N.C., BARNIER B., GALLE B., MOLINES J.M., LE SOMMER J., PENDUFF T. (2012) SENSITIVITY OF COASTAL POLYNYAS AND HIGH-SALINITY SHELF WATER PRODUCTION IN THE ROSS SEA, ANTARCTICA, TO THE ATMOSPHERIC FORCING. *Ocean Dynamics* 62:701723 DOI 10.1007/s10236-012-0531-y

McPHEE, M. G. (1992), TURBULENT HEAT FLUX IN THE UPPER OCEAN UNDER SEA ICE. *J. Geophys. Res.*, 97, 5365-5379.

McPHEE, M. (2008), AIR-ICE-OCEAN INTERACTIONS: TURBULENT OCEAN BOUNDARY LAYER EXCHANGE PROCESSES, CHAPTER 6, PUBLISHED BY SPRINGER.

MCWILLIAMS, J.C., 1977: A NOTE ON A CONSISTENT QUASIGEOSTROPHIC MODEL IN A MULTIPLY CONNECTED DOMAIN. *Dyn. Atmos. Oceans* 1, 427-441.

MEIJERS, A.J.S., KLOCKER, A., BINDOFF, N.L., WILLIAMS, G.D., MARS-LAND, S.J., 2010. THE CIRCULATION AND WATER MASSES OF THE ANTARCTIC SHELF AND CONTINENTAL SLOPE BETWEEN 30 AND 80 E. *Deep-Sea Res. II Top. Stud. Oceanogr.* 57 (910), 723-737

MILLERO F. J. (1978) FREEZING POINT OF SEA WATER: EIGHTH REPORT OF

THE JOINT PANEL OF OCEANOGRAPHIC TABLES AND STANDARDS. *Appendix 6, UNESCO Tech. Pap. Mar. Sci.*, **28**, 2931.

MELLOR, G.L., L. KANTHA(1989), AN ICE-OCEAN COUPLED MODEL, *J. Geophys. Res.*, **94**, 10937-10954.

MITCHELL, W. M., AND J. A. T. BYE (1985), OBSERVATIONS IN THE BOUNDARY LAYER UNDER THE SEA ICE IN McMURDO SOUND, IN OCEANOLGY OF THE ANTARCTIC CONTINENTAL SHELF, *Antarct. Res. Ser.*, VOL. 43, EDITED BY S. JACOBS, PP. 167-176, AGU, WASHINGTON, D. C., doi:10.1029/AR043P0167.

MOFFAT, C., R.C. BEARDSLEY, B. OWENS, AND N. VAN LIPZIG (2008), A FIRST DESCRIPTION OF THE ANTARCTIC PENINSULA COASTAL CURRENT., *Deep Sea Research Part II, Topical Studies in Oceanography* **55**, 3-4, 277-293.

NADEAU, L.P. AND D.N. STRAUB 2011 INFLUENCE OF WIND STRESS, WIND STRESS CURL, AND BOTTOM FRICTION ON THE TRANSPORT OF A MODEL ANTARCTIC CIRCUMPOLAR CURRENT. *J. Phys. Oceanogr.*, **42**, 207222.

NICHOLLS, K.W. (1996), TEMPERATURE VARIABILITY BENEATH RONNE ICE SHELF, ANTARCTICA, FROM THERMISTOR CABLES., *J. Phys. Oceanogr.*, **11**, 1199-1210.

NICHOLLS K. W., PADMAN L., SCHRÖDER M., WOODGATE R. A., JENKINS A., ØSTERHUS S. (2003) WATER MASS MODIFICATION OVER THE CONTINENTAL SHELF NORTH OF RONNE ICE SHELF, ANTARCTICA, *J. Geophys. Res.*, **108(C8)**, 3260, doi:10.1029/2002JC001713.

NICHOLLS K.W., ÖSTERHUS S., MAKINSON K., GAMMELSRØD T., FAHRBACH E. (2009) ICE-OCEAN PROCESSES OVER THE CONTINENTAL SHELF OF THE SOUTHERN WEDDELL SEA, ANTARCTICA: A REVIEW. *Rev. Geophys.*, **47**, RG3003, doi:10.1029/2007RG000250.

NUNEZ-RIBONI I., FAHRBACH E. (2010) AN OBSERVATION OF THE BANDED STRUCTURE OF THE ANTARCTIC COASTAL CURRENT AT THE PRIME MERIDIAN. *Polar Res.* **29**, 322-329.

ORSI, A. H., T. WHITWORTH, AND W. D. NOWLIN, 1995, ON THE MERIDIONAL EXTENT AND FRONTS OF THE ANTARCTIC CIRCUMPOLAR CURRENT. *Deep-Sea Res.*, **42**, 641673.

ORSI, A. H., W. M. SMETHIE JR., AND J. L. BULLISTER, (2002) ON THE TOTAL INPUT OF ANTARCTIC WATERS TO THE DEEP OCEAN: A PRELIMINARY ESTIMATE FROM CHLOROFUOROCARBON MEASUREMENTS, *J. Geophys. Res.*, **107(C8)**, doi:10.1029/2001JC000976.

ORSI, A.H., WIEDERWOHL, C.L. (2009), A RECOUNT OF ROSS SEA WATER, *Deep-Sea Research II*, **56**, 778-795.

PHILLIPS, N. A., 1954, ENERGY TRANSFORMATIONS AND MERIDIONAL CIRCULATIONS. *Tellus*, **6**, PP. 273-286.

PAVAN, V., AND I. M. HELD, 1996: THE DIFFUSIVE APPROXIMATION FOREDDY UXES IN BAROCLINICALLY UNSTABLE JETS. *I.J. ATMOS. SCI.*, **53**, 12621272.

PEDLOSKY, J. "GEOPHYSICAL FLUID DYNAMICS. 1979."

- POULIN, F. J., AND G. R. FLIERL. 2005: THE INFLUENCE OF TOPOGRAPHY ON THE STABILITY OF JETS. *J. Phys. Oceanogr.*, 35.5, 811-825.
- PRITCHARD, H. D. , S. R. M. LIGTENBERG, H. A. FRICKER, D. G. VAUGHAN, M. R. VAN DEN BROEKE AND L. PADMAN (2012), ANTARCTIC ICE-SHEET LOSS DRIVEN BY BASAL MELTING OF ICE SHELVES, *Nature*, 484, 502505 (26 APRIL 2012) doi:10.1038/NATURE10968
- REDDY, T., D.M. HOLLAND, K. ARRIGO (2010), ROSS ICE SHELF CAVITY CIRCULATION, RESIDENCE TIME, AND MELTING: RESULTS FROM A MODEL OF OCEANIC CHLOROFLUOROCARBONS, *Continental Shelf Res.*, 30.7 (2010): 733-742.
- RHINES, P. B., 1975: WAVES AND TURBULENCE ON A BETA-PLANE. *J. Fluid Mech.*, 69, 417443
- RIGNOT E., JACOBS S. (2002) RAPID BOTTOM MELTING WIDESPREAD NEAR ANTARCTIC ICE SHEET GROUNDING LINES. *Science*, 296, 2020-2023.
- RIGNOT, ERIC; VAUGHAN, DAVID G.; SCHMELTZ, MAJORIE; DUPONT, TODD; MACAYEAL, DOUGLAS. 2002 ACCELERATION OF PINE ISLAND AND THWAITES GLACIERS, WEST ANTARCTICA. *Annals of Glaciology*, 34. 189-194. 1
- ROBINSON, N. J., M. J. M. WILLIAMS, P. J. BARRETT, AND A. R. PYNE (2010), OBSERVATIONS OF FLOW AND ICE-OCEAN INTERACTION BENEATH THE McMURDO ICE SHELF, ANTARCTICA, *J. Geophys. Res.*, 115, C03025, doi:10.1029/2008JC005255.

ROBINSON, N. J., & M. J. M. WILLIAMS (2012), ICEBERG-INDUCED CHANGES TO POLYNYA OPERATION AND REGIONAL OCEANOGRAPHY IN THE SOUTHERN ROSS SEA, ANTARCTICA, FROM IN SITU OBSERVATIONS, *Antarctic Science*, 514-526.

SAGGIOMO, V., G. CATALANO, O. MANGONI, G. BUDILLON, G.C. CARRADA (2002), PRIMARY PRODUCTION PROCESSES IN ICE-FREE WATERS OF THE ROSS SEA (ANTARCTICA) DURING THE AUSTRAL SUMMER 1996, *Deep Sea Research II*, 49, 1787-1801

SAMELSON, R. M. (1992) FLUID EXCHANGE ACROSS A MEANDERING JET. *J. of Phys. Oceanogr.* 22.4, 431-444.

SCAMBOS, TED A., J. A. BOHLANDER, C. A. SHUMAN, AND P. SKVARCA. (2004), GLACIER ACCELERATION AND THINNING AFTER ICE SHELF COLLAPSE IN THE LARSEN B EMBAYMENT, ANTARCTICA. *Geophys. Res. Lett.* **31**, NO. 18

SELKER, J., N. VAN DE GIESEN, M. WESTHOFF, W. LUXEMBURG, AND M. B. PARLANGE (2006), FIBER OPTICS OPENS WINDOW ON STREAM DYNAMICS, *Geophys. Res. Lett.*, 33, L24401, doi:10.1029/2006GL027979.

SHCHEPETKIN, A. F., AND J. C. MCWILLIAMS, 2009: CORRECTION AND COMMENTARY FOR OCEAN FORECASTING IN TERRAIN-FOLLOWING COORDINATE: FORMULATION AND SKILL ASSESSMENT OF THE REGIONAL OCEAN MODELING SYSTEM BY HAIDVOGEL ET AL., *J. Comp. Phys.* 227, PP. 3595-3634. *J. Comput. Phys.*, 228, 8985-9000, doi:10.1016/j.jcp.2009.09.002.

SINHA, B., AND K. J. RICHARDS, 1999: JET STRUCTURE AND SCALING IN SOUTHERN OCEAN MODELS. *J. Phys. Oceanogr.*, 29, 11431155.

- SOKOLOV, SERGUEI, STEPHEN R. RINTOUL, 2007: MULTIPLE JETS OF THE ANTARCTIC CIRCUMPOLAR CURRENT SOUTH OF AUSTRALIA. *J. Phys. Oceanogr.*, 37, 13941412. DOI: [HTTP://DX.DOI.ORG/10.1175/JPO3111.1](http://dx.doi.org/10.1175/JPO3111.1)
- SRINIVASAN, KAUSHIK, W. R. YOUNG, 2012: ZONOSTROPHIC INSTABILITY. *J. Atmos. Sci.*, 69, 16331656., DOI: [HTTP://DX.DOI.ORG/10.1175/JAS-D-11-0200.1](http://dx.doi.org/10.1175/JAS-D-11-0200.1)
- ST-LAURENT, P., J. M. KLINCK, AND M. S. DINNIMAN (2013), ON THE ROLE OF COASTAL TROUGHS IN THE CIRCULATION OF WARM CIRCUMPOLAR DEEP WATER ON ANTARCTIC SHELVES, *J. Phys. Ocean.* 43, DOI: 10.1175/JPO-D-0237.1.
- STERN M.E., WHITEHEAD J.A, HUA, B.L. (1982) THE INTRUSION OF A DENSITY CURRENT ALONG THE COAST OF A ROTATING FLUID. *J. Fluid Mech.* **123**, 237-266.
- A.A. STERN, M.S. DINNIMAN, V. ZAGORODNOV, S.W. TYLER, AND D.M. HOLLAND1, INTRUSION OF WARM SURFACE WATER BENEATH THE McMURDO ICE SHELF, ANTARCTICA (2013), INTRUSION OF WARM SURFACE WATER BENEATH THE McMURDO ICE SHELF, ANTARCTICA, *J. of Geophys. Res.*
- STERN, A. A., HOLLAND, D. M., HOLLAND, P. R., JENKINS, A., AND SOMERIA, J. (2014). THE EFFECT OF GEOMETRY ON ICE SHELF OCEAN CAVITY VENTILATION: A LABORATORY EXPERIMENT. *EXPERIMENTS IN FLUIDS*, 55(5), 1-19.
- STEWART, A.L. & A.F. THOMPSON, 2013. CONNECTING ANTARCTIC CROSS-

SLOPE EXCHANGE WITH SOUTHERN OCEAN OVERTURNING. *J. of Phys. Oceanogr.*, 43, 1453-1471

THOMPSON, A.F. (2010) JET FORMATION AND EVOLUTION IN BAROCLINIC TURBULENCE WITH SIMPLE TOPOGRAPHY BY AN OPEN-OCEAN CURRENT *J. of Phys. Oceanogr.*, 40, 257-278, DOI: 10.1175/2009JPO4218.1

THOMPSON, A. F., AND K. J. RICHARDS (2011), LOW FREQUENCY VARIABILITY OF SOUTHERN OCEAN JETS, *J. Geophys. Res.*, 116, C09022, doi:10.1029/2010JC006749.

THOMA, M., A. JENKINS, D. HOLLAND, AND S. JACOBS, 2008: MODELLING CIRCUMPOLAR DEEP WATER INTRUSIONS ON THE AMUNDSEN SEA CONTINENTAL SHELF, ANTARCTICA. *Geophys. Res. Lett.*, 35, L18602, doi:10.1029/2008GL034939.

TYLER, S. W., J. S. SELKER, M. B. HAUSNER, C. E. HATCH, T. TORGERSEN, C. E. THODAL, AND S. G. SCHLADOW (2009), ENVIRONMENTAL TEMPERATURE SENSING USING RAMAN SPECTRA DTS FIBER-OPTIC METHODS, *Water Resour. Res.*, 45, W00D23, doi:10.1029/2008WR007052, [PRINTED 46(4), 2010].

TYLER, S. W., D.M. HOLLAND, V. ZAGORODNOV, A.A. STERN, C. SLADEK, S. KOBS, S. WHITE, F. SUAREZ, J. BRYENTON (2013), INSTRUMENTS AND METHODS USING DISTRIBUTED TEMPERATURE SENSORS TO MONITOR AN ANTARCTIC ICE SHELF AND SUB-ICE-SHELF CAVITY, *J. of Glaciology.*, VOL. 59, No. 215, 2013 doi:10.3189/2013JoG12J207.

VAN DE GIESEN, N.; S.C STEELE-DUNNE J. JANSEN, O. HOES, M.B HAUSNER, S. TYLER AND J. SELKER (2012), DOUBLE-ENDED CALIBRATION OF FIBER-OPTIC RAMAN SPECTRA DISTRIBUTED TEMPERATURE SENSING DATA, *Sensors* 12, NO. 5: 5471-5485.

VALLIS, GEOFFREY K., EDWIN P. GERBER, PAUL J. KUSHNER, BENJAMIN A. CASH, 2004: A MECHANISM AND SIMPLE DYNAMICAL MODEL OF THE NORTH ATLANTIC OSCILLATION AND ANNULAR MODES. *J. ATMOS. SCI.*, 61, 264280.

WAHLIN A.K., DARELIUS E., CENEDESE C., LANE-SERFF G.F. (2008). LABORATORY OBSERVATIONS OF ENHANCED ENTRAINMENT IN DENSE OVERFLOWS IN THE PRESENCE OF SUBMARINE CANYONS AND RIDGES. *Deep-sea Research 1, 55*, 737-750. DOI: 10.1016/J.DSR.2008.02.007.

WALKER, D. P., M. A. BRANDON, A. JENKINS, J. T. ALLEN, J. A. DOWDESWELL, AND J. EVANS (2007), OCEANIC HEAT TRANSPORT ONTO THE AMUNDSEN SEA SHELF THROUGH A SUBMARINE GLACIAL TROUGH, *Geophys. Res. Lett.*, 34, L02602, doi:10.1029/2006GL028154.

WALKER, R.T., D.M. HOLLAND, B.R. PARIZEK, R.B. ALLEY, S.M.J. NOWICKI, A. JENKINS (2013), EFFICIENT FLOWLINE SIMULATIONS OF ICE-SHELF/OCEAN INTERACTIONS: SENSITIVITY STUDIES WITH A FULLY COUPLED MODEL, *J. Phys Oceanography*. (INPRESS).

WAHLIN, A. K., X. YUAN, G. BJORK, AND C. NOHR, 2010: INFLOW OF WARM CIRCUMPOLAR DEEP WATER IN THE CENTRAL AMUNDSEN SHELF. *J. Phys. Oceanogr.*, 40, 14271434, doi:10.1175/2010JPO4431.1.

WELLS M.G., WETTLAUFER J. S. (2008). THE CIRCULATION IN LAKE VOSTOK: A LABORATORY ANALOGUE STUDY. GEOPHYSICAL RESEARCH LETTERS. 35, L0350, doi:10.1029

V. ZAGORODNOV, S. TYLER, D. HOLLAND, A. STERN, L.G. THOMPSON, C. SLADEK, S. KOBS, J. NICOLS, (2014) ASSESSMENT OF ACCESS BOREHOLE DRILLING TECHNIQUE IN SHELF GLACIERS. (SUBMITTED TO ANNALS OF GLACIOLOGY)

ZATSEPIN A.G., DIDKOVSKI V.L., SEMENOV A.V. (1996) A SELF-OSCILLATORY MECHANISM OF INDUCING A VORTEX SLOPING BOTTOM IN A ROTATING FLUID. *Oceanology* 38, 4350.

ZHANG, YU, JOSEPH PEDLOSKY, GLENN R. FLIERL, 2011: CROSS-SHELF AND OUT-OF-BAY TRANSPORT DRIVEN BY AN OPEN-OCEAN CURRENT. *J. Phys. Oceanogr.*, 41, 21682186.